arXiv:1705.08629v1 [physics.ins-det] 24 May 2017

Technical Design Report (TDR): Searching for a Sterile Neutrino at J-PARC MLF (E56, JSNS^2)

S. Ajimura[1], M. K. Cheoun[2], J. H. Choi[3], H. Furuta[4], M. Harada[5], S. Hasegawa[5], Y. Hino[4], T. Hiraiwa[1], E. Iwai[6], S. Iwata[7], J. S. Jang[8], H. I. Jang[9], K. K. Joo[10], J. Jordan[6], S. K. Kang[11], T. Kawasaki[7], Y. Kasugai[5], E. J. Kim[12], J. Y. Kim[10], S. B. Kim[13], W. Kim[14], K. Kuwata[4], E. Kwon[13], I. T. Lim[10], T. Maruyama*[15], T. Matsubara[4], S. Meigo[5], S. Monjushiro[15], D. H. Moon[10], T. Nakano[1], M. Niiyama[16], K. Nishikawa[15], M. Nomachi[1], M. Y. Pac[3], J. S. Park[15], H. Ray[17], C. Rott[18], K. Sakai[5], S. Sakamoto[5], H. Seo[13], S. H. Seo[13], A. Shibata[7], T. Shima[1], J. Spitz[6], I. Stancu[19], F. Suekane[4], Y. Sugaya[1], K. Suzuya[5], M. Taira[15], W. Toki[20], T. Torizawa[7], M. Yeh[21], and I. Yu[18]

[1] *Research Center for Nuclear Physics, Osaka University, Osaka, JAPAN*
[2] *Department of Physics, Soongsil University, Seoul 06978, KOREA*
[3] *Department of Radiology, Dongshin University, Chonnam 58245, KOREA*
[4] *Research Center for Neutrino Science, Tohoku University, Sendai, Miyagi, JAPAN*
[5] *J-PARC Center, JAEA, Tokai, Ibaraki JAPAN*
[6] *University of Michigan, Ann Arbor, MI, 48109, USA*
[7] *Department of Physics, Kitasato University, Sagamihara 252-0373, Kanagawa, JAPAN*
[8] *Gwangju Institute of Science and Technology, Gwangju, 61005, KOREA*
[9] *Department of Fire Safety, Seoyeong University, Gwangju 61268, KOREA*
[10] *Department of Physics, Chonnam National University, Gwangju, 61186, KOREA*
[11] *School of Liberal Arts, Seoul National University of Science and Technology, Seoul, 139-743, KOREA*
[12] *Division of Science Education, Physics major, Chonbuk National University, Jeonju, 54896, KOREA*
[13] *Department of Physics and Astronomy, Seoul National University, Seoul 08826, KOREA*
[14] *Department of Physics, Kyungpook National University, Daegu 41566, KOREA*
[15] *High Energy Accelerator Research Organization (KEK), Tsukuba, Ibaraki, JAPAN*
[16] *Department of Physics, Kyoto University, Kyoto, JAPAN*
[17] *University of Florida, Gainesville, FL, 32611, USA*
[18] *Department of Physics, Sungkyunkwan University, Gyeong Gi-do, KOREA*
[19] *University of Alabama, Tuscaloosa, AL, 35487, USA*
[20] *Colorado State University, Tuscaloosa, AL, 35487, USA*
[21] *Brookhaven National Laboratory, Upton, NY, 11973-5000, USA*

March 12, 2022

*Spokesperson:(takasumi.maruyama@kek.jp)

Contents

1 Introduction **4**

2 Physics of the JSNS^2 experiment **4**
2.1 Search for $\bar{\nu_\mu} \to \bar{\nu_e}$ oscillation as a direct and an ultimate test for LSND . 4
2.1.1 Experimental status 4
2.1.2 The JSNS^2 Experiment 7
2.1.3 Experiment Strategy 12
2.2 Measurement of Neutrino-Induced Nuclear Reaction Cross Sections . . . 12
2.2.1 Physics Motivations 12
2.2.2 Measurement Plan for the ^{12}C(ν_e,e$^-$)^{12}N Cross Section in JSNS^2 . 13
2.3 Physics with neutrinos from charged kaon decay-at-rest 14

3 Experimental Components **17**
3.1 The J-PARC MLF as a DAR Neutrino Source 17
3.1.1 The RCS beam and the target 17
3.1.2 Neutrino Beam 19
3.1.3 Estimated Neutrino Flux 20
3.2 Detector Location and Constraints 20
3.2.1 Withstand Weight Load 22
3.3 Tanks 24
3.3.1 General structure 24
3.3.2 Stainless Steel Tank and Anti Oil-Leak Tank 25
3.3.3 Acrylic Vessel 25
3.3.4 Liquid level stabilizing mechanism 27
3.3.5 Emergency overflow pipes 29
3.4 Safety Protection System 29
3.4.1 Second Anti Oil-Leak Tank 30
3.4.2 Sealing the Space between Hatches and Concrete 30
3.4.3 The Third Anti Oil-Leak Wall 31
3.4.4 Slow Monitors 32
3.5 PhotoMultiplier Tube and its system 33
3.5.1 Overview of the PMT system 33
3.5.2 PMT 33
3.5.3 Test, Delivery 34
3.5.4 Noise test at MLF 3rd Floor 41
3.5.5 Magnetic Shield 42
3.5.6 Magnetic Field Measurement on the 3rd Floor of the MLF 42
3.6 Veto system 42
3.7 High Voltage System 46
3.8 Liquid Scintillator 46
3.8.1 Recipe of LS 48
3.8.2 Purification of LS 48
3.8.3 Mass Production of LS 49
3.8.4 Gadolinium-loaded LS 49
3.8.5 Synthesis of Gd-LAB 50

3.8.6 Mass production of Gd-loaded LS . . . 50
3.9 Electronics, DAQ . . . 51
3.10 Calibration System . . . 52
3.10.1 LED System . . . 53
3.10.2 Laser System . . . 56
3.11 Installation works inside Tank . . . 57
3.12 Expected Experimental Operation . . . 60
3.12.1 Normal Operation . . . 60
3.12.2 Operation in the Emergency . . . 64
3.13 Offline Software . . . 65
3.13.1 Event Reconstruction and Particle Identification . . . 65

4 Understandings of the Background and Expected Detector Performance 66
4.1 Expected Detector Performance . . . 66
4.1.1 Energy Resolution . . . 66
4.1.2 Pulse Shape Discrimination (PSD) capability . . . 67
4.1.3 Selection criteria and the signal efficiency . . . 69
4.2 Summary of 2014 Measurement . . . 70
4.2.1 Revised Numbers from the Reference . . . 72
4.3 Summary of Backgrounds . . . 75

5 Sensitivity for the Sterile Neutrino Search 75
5.1 Fit method . . . 75
5.2 Systematic uncertainties . . . 77
5.3 Sensitivity for $\bar{\nu_\mu} \to \bar{\nu_e}$ oscillation . . . 78

6 Summary 78

7 Requests to J-PARC PAC 79

8 Acknowledgements 79

A Strength Calculation around the Stainless Tank 80
A.1 Thickness of the Stainless Tank for the Static Operation . . . 80
A.1.1 Wall . . . 80
A.1.2 Top . . . 80
A.2 Strength of Stainless Tank during the Earthquake . . . 81
A.2.1 Wall Part . . . 81
A.2.2 Welding Condition to Prohibit Sliding of the Detector . . . 81
A.3 FEM calculation . . . 82
A.3.1 Static Operation . . . 82
A.3.2 Earthquake case . . . 85
A.3.3 How to fix the Detector to the Floor . . . 87

1 Introduction

In this document, the technical details of the JSNS^2 (J-PARC Sterile Neutrino Search at J-PARC Spallation Neutron Source) experiment are described.

The search for sterile neutrinos is currently one of the hottest topics in neutrino physics. The JSNS^2 experiment aims to search for the existence of neutrino oscillations with Δm^2 near 1 eV^2 at the J-PARC Materials and Life Science Experimental Facility (MLF). A 1 MW beam of 3 GeV protons incident on a spallation neutron target produces an intense neutrino beam from muon decay at rest. Neutrinos come predominantly from μ^+ decay: $\mu^+ \to e^+ + \bar{\nu}_\mu + \nu_e$. The experiment will search for $\bar{\nu}_\mu$ to $\bar{\nu}_e$ oscillations which are detected by the inverse beta decay interaction $\bar{\nu}_e + p \to e^+ + n$, followed by gammas from neutron capture on Gd. The detector has a fiducial volume of 17 tons and is located 24 meters away from the mercury target. JSNS^2 offers the ultimate direct test of the LSND anomaly.

In addition to the sterile neutrino search, the physics program includes cross section measurements with neutrinos with a few 10's of MeV from muon decay at rest and with monochromatic 236 MeV neutrinos from kaon decay at rest. These cross sections are relevant for our understanding of supernova explosions and nuclear physics.

2 Physics of the JSNS^2 experiment

2.1 Search for $\bar{\nu_\mu} \to \bar{\nu_e}$ oscillation as a direct and an ultimate test for LSND

2.1.1 Experimental status

Experimental evidence for sterile neutrinos would come from disappearance or appearance of active flavors with a new Δm^2 inconsistent with Δm^2_{12} or Δm^2_{23}. Table 1 gives a summary of observed experimental anomalies and their significance.

Experiment	neutrino source	Signal	σ
LSND	π decay at rest	$\bar{\nu}_\mu \to \bar{\nu}_e$	3.8σ
MiniBooNE	π decay in flight	$\nu_\mu \to \nu_e$	3.4σ
MiniBooNE	π decay in flight	$\bar{\nu}_\mu \to \bar{\nu}_e$	2.8σ
Gallium/SAGE	e capture	$\nu_e \to \nu_x$	2.7σ
Reactor	β decay	$\bar{\nu}_e \to \bar{\nu}_x$	3.0σ

Table 1: Possible large Δm^2 anomalies

The first indication of a possible sterile neutrino was reported by the LSND experiment. LSND reported an excess of $87.9 \pm 22.4 \pm 6.0$ $\bar{\nu}_e$ events (3.8σ) in 1998 [1]. The MiniBooNE experiment recently reported observed excesses of $\nu_e, \bar{\nu}_e$ candidates in the 200-1250 MeV energy range in neutrino mode (3.4σ) and in anti-neutrino mode (2.8σ) respectively. The combined excess is $240.3 \pm 34.5 \pm 52.6$ events, which corresponds to

3.8σ [2]. It is not clear whether the excesses are due to oscillations, but if they are, both LSND and MiniBooNE indicate a flavor conversion of $\bar{\nu}_\mu$ to $\bar{\nu}_e$ at a probability of about 0.003 with a Δm^2 of ~ 1 eV^2.

The second indicatation is a deficit observed in the calibration of low energy radiochemical solar neutrino experiments. The results indicate a deficiency in neutrino event rates. Monoenergetic neutrino sources (^{51}Cr and ^{37}Ar) were used in these experiments. Their results were presented in terms of the ratio of the observed and predicted rates. The predictions are based on theoretical calculations of neutrino cross sections by Bahcall and by Haxton. The quoted numbers are $R_{obs}/R_{pred} = 0.86 \pm 0.05(\sigma_{Bahcall}), 0.76 \pm 0.085(\sigma_{Haxton})$ [3].

The final anomaly is the so-called reactor anomaly, a 6% deficit of detected $\bar{\nu}_e$ from nuclear reactors at baselines less than 100 m. The ratio of the observed and expected rates is 0.927 ± 0.023, and is based entirely on the re-analysis of existing data. The deficit is caused by three independent effects which all tend to increase the expected neutrino event rate. There have been two re-evaluations of reactor anti-neutrino fluxes and both indicate an increase of flux by about 3%. The neutron lifetime decreased from 887-899s to 885.7s and thus the inverse β-decay cross section increased by a corresponding amount. The contribution from long-lived isotopes to the neutrino spectrum was previously neglected and enhances the neutrino flux at low energies [4].

All these hints have a statistical significance around $3 - 3.8\sigma$ and may be caused by one or more sterile neutrinos with a mass of roughly 1 eV. If they are due to neutrino oscillation with new mass state $m_4(\sim\text{eV})$, the disappearance and the appearance of active neutrinos are related by ($m_4 \gg m_{1,2,3}$ and $U_{s4} \sim 1 \gg U_{e\mu\tau,4}$.)

$$
\begin{aligned}
P(\nu_e, \nu_\mu \to \nu_s) &= -4 \sum_{i>j} Re(U_{si} U^*_{\mu,ei} U^*_{sj} U_{\mu,ej}) \sin^2 \Delta_{ij} \\
&- 2 \sum_{i>j} Im(U_{si} U^*_{\mu,ei} U^*_{sj} U_{\mu,ej}) \sin 2\Delta_{ij} \\
P(\nu_\mu \to \nu_e) &= -4 \sum_{i>j} Re(U_{ei} U^*_{\mu i} U^*_{ej} U_{\mu j}) \sin^2 \Delta_{ij} \\
&- 2 \sum_{i>j} Im(U_{ei} U^*_{\mu i} U^*_{ej} U_{\mu j}) \sin 2\Delta_{ij} \\
\Delta_{ij} &= (m_j^2 - m_i^2) L/4E_\nu
\end{aligned}
$$

For a short baseline experiments ($L(m)/E(MeV) \sim 1$) and if only one sterile neutrino involved in mixing,

$$
\begin{aligned}
P(\nu_{e,\mu} \to \nu_s) &\sim -4 \sum_j Re(U_{s4} U^*_{\mu,e4} U^*_{sj} U_{\mu,ej}) \sin^2(m^2_4 L/4E_\nu) \\
&- 2 \sum_j Im(U_{s4} U^*_{\mu,e4} U^*_{sj} U_{\mu,ej}) \sin 2(m^2_4 L/4E_\nu) \\
&= 4 \mid U_{s4} \mid^2 \mid U_{\mu,e4} \mid^2 \sin^2(m^2_4 L/4E_\nu) \\
P(\nu_\mu \to \nu_e) &\sim -4 \sum_i Re(U_{e4} U^*_{\mu 4} U^*_{ei} U_{\mu i}) \sin^2(m^2_4 L/4E_\nu) \\
&- 2 \sum_j Im(U_{e4} U^*_{\mu 4} U^*_{ej} U_{\mu j}) \sin 2(m^2_4 L/4E_\nu) \\
&= 4 \mid U_{e4} \mid^2 \mid U_{\mu 4} \mid^2 \sin^2(m^2_4 L/4E_\nu)
\end{aligned}
\tag{1}
$$

Thus $P(\nu_\mu \to \nu_s) \cdot P(\nu_e \to \nu_s) \sim P(\nu_\mu \to \nu_e)$.

In order for the LSND and MiniBooNE data to be consistent with the sterile neutrino hypothesis, ν_μ disappearance at $\Delta m^2 \sim \mathrm{eV}^2$ should exist in addition to the observed ν_e deficiencies. So far only several % level upper limits exist for ν_μ disappearance and thus some tensions exist [5].

The allowed regions are shown in Fig. 1 for the appearance channel (left figure) ($\bar{\nu}_\mu \to \bar{\nu}_e$) and for the disappearance channel (right figure) ($\nu_e \to \nu_s$).

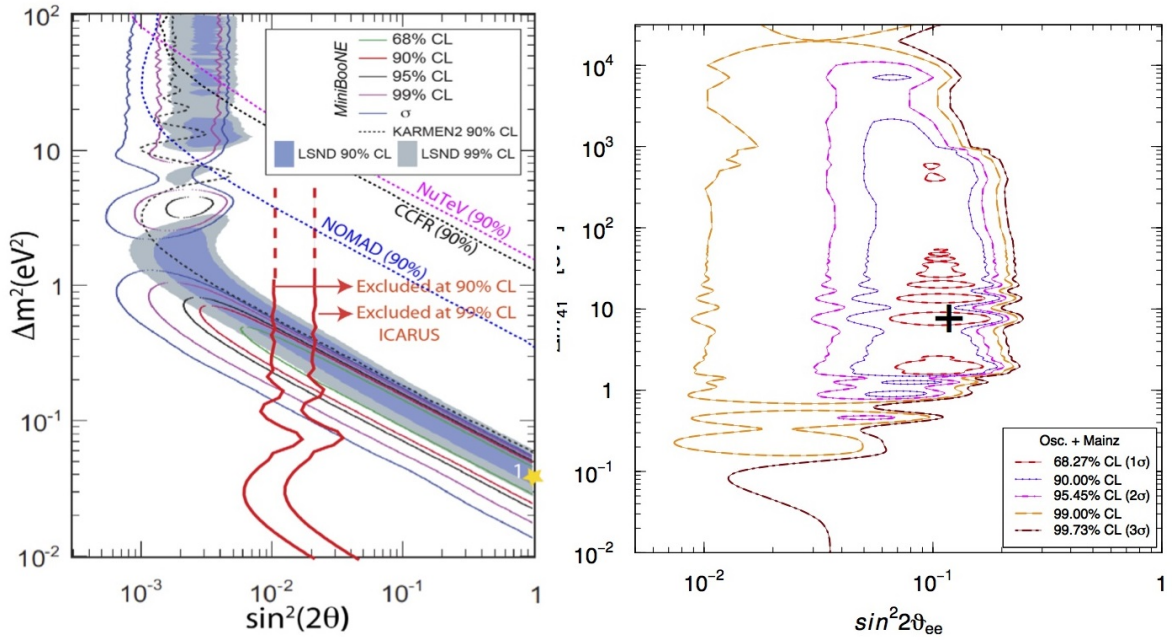


Figure 1: Left figure : Allowed region for $\bar{\nu}_\mu \to \bar{\nu}_e$ appearance channel as a result of combining LSND, MiniBooNE and ICARUS [6]. Right figure : Allowed region for disappearance channel with Reactor and β source anomalies, taken into account the KATRIN and neutrino-less double β decay limits [7].

Recently, several results on the sterile neutrino search have been updated [8, 9, 10, 11,

12] for ν_μ and ν_e disappearance modes. In short, the Daya Bay and NEOS experiments have excluded the region $\Delta m^2 \leq 1$ eV^2 of the Fig. 1, and the MINOS, Super-Kamiokande, and IceCube experiments have crucial null results for the ν_μ disappearance at $\Delta m^2 \sim$ eV^2.

These results prefer higher Δm^2 in the global fit [13] and motivate the JSNS^2 experiment which is sensitive in the higher Δm^2 region favored by the fits.

2.1.2 The JSNS^2 Experiment

In the context of these global results, we proposed a search for the existence of neutrino oscillations with Δm^2 near 1 eV^2 at the J-PARC MLF: JSNS^2 (J-PARC Sterile Neutrino Search at J-PARC Spallation Neutron Source) experiment in 2013 [14]. With the 3 GeV proton beam from the Rapid Cycling Synchrotron (RCS), and a spallation neutron target, an intense neutrino beam from muon decay at rest (μDAR) is available. Neutrinos come predominantly from μ^+ decay: $\mu^+ \rightarrow e^+ + \bar{\nu}_\mu + \nu_e$. We will search for $\bar{\nu}_\mu \rightarrow \bar{\nu}_e$ oscillations which are detected via the inverse β decay (IBD) interaction $\bar{\nu}_e + p \rightarrow e^+ + n$ followed by gammas from neutron capture inside the liquid scintillator. Figure 2 shows the overall setup of the JSNS^2 experiment. The detector will be placed at a baseline of 24 meters and will contain 17 tons of gadolinium (Gd) loaded liquid scintillator (LS) inside an inner acrylic vessel, and ~30 tons unloaded LS in the space between the acrylic vessel and an outer stainless steel tank. 193 8-inch PMTs between the acrylic vessel and stainless tank will view the sensitive inner volume and 48 5-inch PMTs will be placed in the outer veto region.

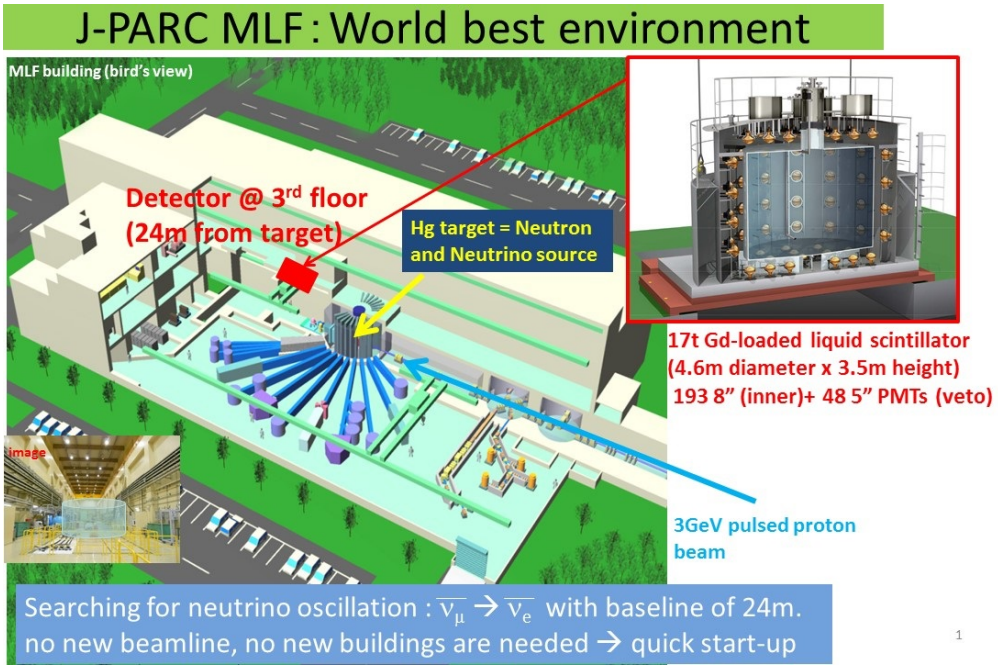


Figure 2: The MLF building and the overview of the JSNS^2 experimental setup.

This experiment is the ultimate direct test of the LSND experiment because it uses

the same neutrino source (μDAR), and the same neutrino target and interaction (IBD) as LSND, but with several imrpovements. The signal-to-noise ratio is much better due to the lower duty factor of the proton beam (0.7 μs beam pulse / 40000 μs pulse separation) with repetition at 25 Hz. The use of Gd-loaded liquid scintillator in the target volume also lowers the neutron capture time which lowers accidental backgrounds and improves the signal-to-noise ratio.

Figure 3 shows the merit of using the short pulse, low duty factor beam. The black

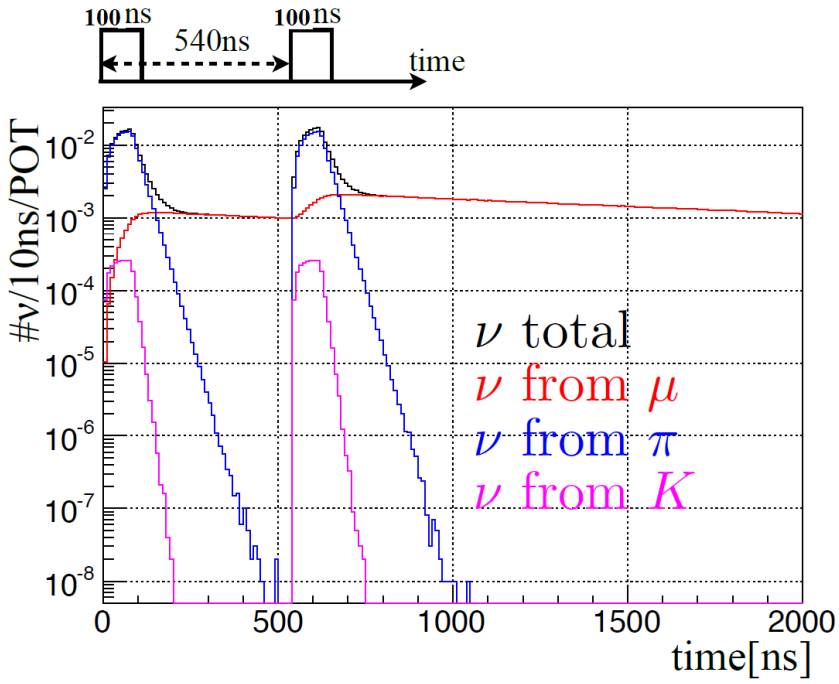


Figure 3: Time distribution of neutrinos from pion, muon and kaon decays is shown. Only neutrinos from muon decay at rest survive after 1 μs from the start of proton beam.

square pulse corresponds to the proton beam bunch timing, and the time distribution of neutrinos from pion, muon and kaon decays is shown. Only neutrinos from muon decay at rest survive after 1 μs from the start of proton beam. Thus, neutrinos from pion and kaon decays as well as the beam fast neutrons are eliminated with the 1 μs timing gate. In addition to the on-bunch timing cuts, a timing gate from 1 to 10 μs from the beam starting time is applied for event selection because the next beam bunch comes after 40 ms (25 Hz). This reduces the cosmic ray induced background by factor of 9/40000. Note that the LSND had 600 μs beam bunches with 120 Hz operation from the LINAC beam, and therefore the on-bunch neutrinos and neutrons could not be removed. Also the beam duty factor was 600 μs $\times$ 120 Hz = 7.2%, which is higher than that of the MLF by factor of $\sim$14400.

The Gd-loaded LS is also quite a strong tool for eliminating the accidental background. The IBD delayed signal from neutron capture gammas in Gd-doped liquid scintillator gives a shorter coincidence gate (about 30 μs) due to higher capture cross section and higher gamma energy (8 MeV) than capture on hydrogen ($\sim$ 200 μs and 2.2 MeV). The coincidence gate timing reduces the background by a factor 6-7 and the higher energy of the capture gammas reduces the background by factor of more than 100 due to the

presence of environmental gammas up to 2.6 MeV.

Compared to experiments using the horn-focused beams (e.g. the SBN experiments [15]), JSNS^2 has a few advantages. First, using neutrinos from the spallation neutron source reduces the intrinsic background from $\bar{\nu}_e$ by a factor of $\sim$10. Second, the energy reconstruction for neutrinos from μDAR is simple which allows for a precise determination of the energy of candidate oscillation events.

The spallation neutron source is the mercury target, which is a high-Z material, surrounded by thick iron and concrete in the target enclosure as shown in Fig. 9. Due to strong nuclear absorption of π^- and μ^- in the mercury target, neutrinos from μ^- decay are strongly suppressed to about the 10^{-3} level. The resulting neutrino beam is predominantly ν_e and $\bar{\nu}_\mu$ from μ^+ with contamination from other neutrino species at the level of 10^{-3}. For horn-focused neutrino beams, however, it is well-known that the ν_μ beam from pions contains ν_e background at the 1% level from muon contamination.

The energy of neutrinos from μDAR is quite well known: it is the Michel spectrum. The energy reconstruction of IBD is also very easy: $E_\nu \sim E_{visible} + 0.8$ MeV where $E_{visible}$ is the visible energy of positron. These two features make the energy information available for the final analysis which is important because the neutrino oscillation is a function of the neutrino energy. On the other hand, a horn-focused beam has large uncertainty on the neutrino energy spectrum because the parent pion production at the target is not well understood and it propagates to uncertainty in the energy spectrum. In addition, the reconstruction of neutrino interactions in the sub-GeV and multi-GeV neutrino energy regions suffers from uncertainty in nuclear effects, which again gives large uncertainty in the neutrino energy spectrum.

The μ DAR component of the neutrino flux can be selected by gating out the first 1 μs from the start of the proton beam. The resulting neutrino fluxes for each type of neutrino species are shown in Fig. 4. Note that the resulting $\bar{\nu}_\mu$ and ν_e fluxes have different spectra with endpoint energy of 52.8 MeV. A possible survived μ^- decay will be at the level of 10^{-3} and produce ν_μ and $\bar{\nu_e}$ with same spectrum as those of $\bar{\nu}_\mu$ and ν_e, respectively.

Signatures of the oscillation

A sensitive search for $\bar{\nu}_e$ appearance ($\bar{\nu}_\mu \to \bar{\nu}_e$ from $\mu^+ DAR$) can be performed by searching for the two-fold signature of $\bar{\nu}_e + p \to e^+ + n$ which produces a prompt positron signal with an endpoint of 52.8 MeV followed by gammas due to neutron capture on Gd.

The main background coming from μ^- decays (as shown in Fig. 4) is highly suppressed by π^- and μ^- capture in heavy metals like Hg. However, μ^- which stop in a light metal such as Be, usually decay before absorption. This background can be estimated from the E_ν reconstructed distribution, which is well defined and distinct from oscillated events.

Since the oscillation probability is given by

$$P = \sin^2 2\theta \sin^2\left(\frac{1.27\Delta m^2(eV^2)L(m)}{E_\nu(MeV)}\right),$$

there are two distinct signatures of oscillation signal. One is the energy spectrum of the

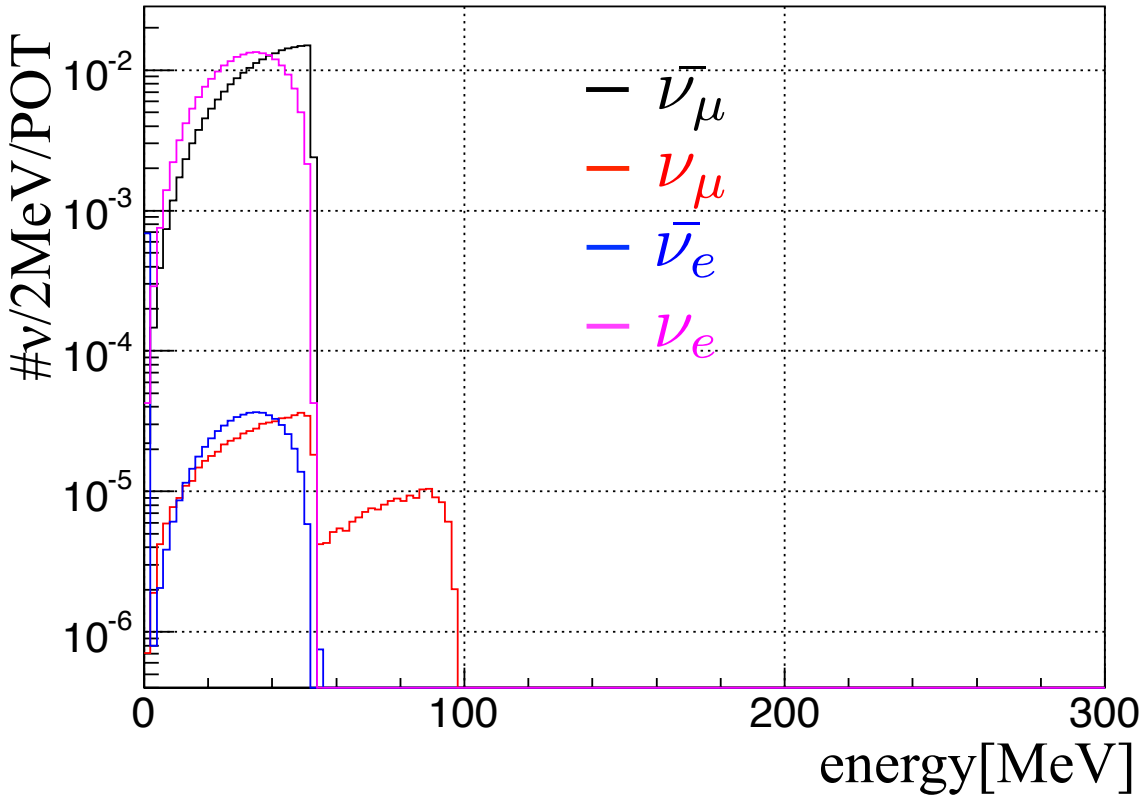


Figure 4: Estimated neutrino flux after 1 μs from the start of proton beam. The $\mu^+ DAR$ components are selected and main background come from μ^- decays.

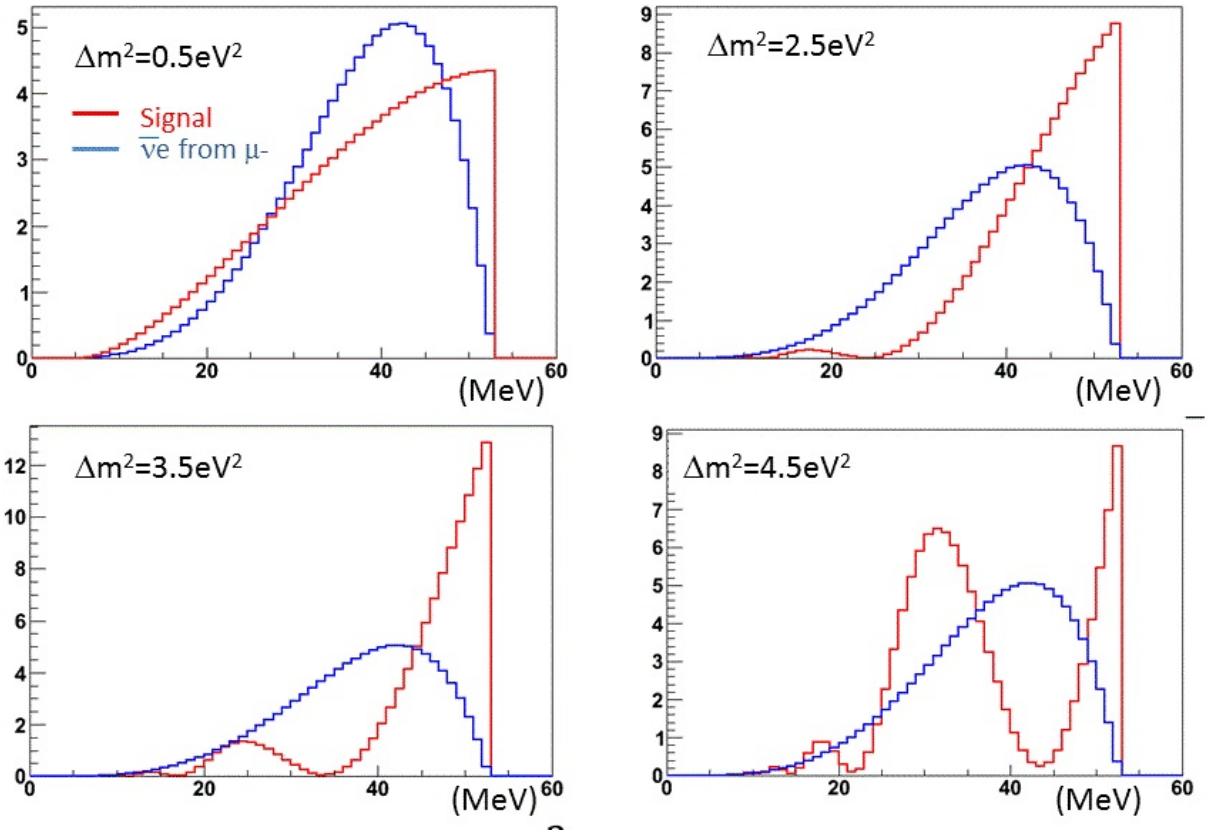


Figure 5: Examples of oscillation signals at typical Δm^2 for a baseline of 24 m. The red graphs are shapes of $\bar{\nu}_e$ appearance signal and the blue graphs are shapes of signal from μ^- decays. All plots are normalized by area.

oscillated signal, which is a convolution of the energy spectrum of the original neutrino (in this case, $\bar{\nu}_\mu$) and the oscillation probability. The other signature is the distribution of events as a function of distance from the source. The background $\bar{\nu}_e$ from μ^- decay has a different spectrum from that of $\bar{\nu}_\mu$ oscillations which can be used to distinguish background from signal. Figure 5 shows $E_{\bar{\nu}}$ distributions of oscillation signals at some typical Δm^2 values for a baseline of 24 m.

Signal identification

The signal for $\bar{\nu_e}$ appearance from $\bar{\nu}_\mu \rightarrow \bar{\nu}_e$ is a primary positron signal followed by delayed signal from neutron capture. The primary signal is $\bar{\nu_e} + p \rightarrow e^+ + n$ (IBD) and the delayed signal consists of gammas from neutron capture on Gd. For the normalization of μ^+ decay, $\nu_e + C \rightarrow e + N_{gs}$ events will be measured. The primary signal is an electron and the delayed signal is a positron from N_{gs} β decay.

The time gate for the primary signal should be from 1 μs to 10 μs, corresponding to several muon lifetimes and avoiding pion decay from both decay at rest and decay in flight. Table 2 is a summary of the primary and delayed signals.

	primary timing	primary energy	delayed timing	delayed energy
$\bar{\nu}_\mu \to \bar{\nu}_e$	1-10 μs	0-53 MeV	10-100 μs	8 MeV
$\nu_e C \to e N_{gs}$, $N_{gs} \to C e^+ \nu_e$	1-10 μs	0-37 MeV	100 μs-10 ms	0-16 MeV

Table 2: The timing and energy of the prompt and delayed signals for IBD events and ν_e scattering of C.

2.1.3 Experiment Strategy

Our strategy is to put a detector with 17 tons of Gd-loaded LS at a baseline of ∼24 meters on the third floor of the MLF (maintenance area of the mercury target). We aim to start the experiment with one 17-ton detector in early 2019 to have world-competitive results soon. This TDR is dedicated to the construction of one detector, and its sensitivity only. If the construction of another detector is realized with the budget, we will submit an amended or another TDR.

2.2 Measurement of Neutrino-Induced Nuclear Reaction Cross Sections

2.2.1 Physics Motivations

Stars with initial masses greater than ∼8-10 times the mass of the sun are expected to end their lives with core-collapse supernovae (Type-II SNe). When such a massive star exhausts the nuclear fuel at its center, it produces no more heat to sustain its own weight, and materials in the outer layers begin to fall into the central core. As the density and the temperature of the core rapidly increase, the core is photo-dissociated into a mixture of nucleons and light nuclei which absorb free electrons by emitting neutrinos, forming a proto-neutron star. The core becomes so hard that material falling into it bounces at the surface and collides with still falling matter, generating an outgoing shockwave.

It has been found through a number of simulations on Type-II SNe that the kinetic energy supplied by the core bounce is not sufficient for the shockwave to travel to infinity, and the additional energy supplied by the interactions between the neutrinos and the nuclei contained in the shockwave should play a critical role in successful explosion [16]. This effect, called neutrino-heating, was studied by one-dimensional and two-dimensional simulations with different neutrino luminosities, and it was found that enhancement of the neutrino luminosity by ∼10-15% leads to an increase of the kinetic energy of the shockwave by $\sim 10^{50}$-10^{51} erg/s, which is sufficient for a successful explosion [17]. Since enhancement of the neutrino-nucleus reaction rates are expected to give the same effect as that of the neutrino luminosity, the neutrino-nucleus cross sections should be known with uncertainties smaller than ∼10-15%.

Another important role of neutrino-induced nuclear reactions is in r-process nucleosynthesis. A recent scenario of the r-process assumes the formation of a high-entropy, neutron-rich gas, called the neutrino-driven wind, in the atmosphere of a nascent neutron

star by neutrino-induced spallation reactions, and the synthesis of heavy elements from protons and neutrons up to the nuclides with mass number of ∼200-250 within about one second [18, 19, 20]. This scenario is preferred, because it does not require the existence of seed nuclei like iron, and naturally explains the universality of the r-elements (i.e. the similarity in the r-element abundances observed in stars with different metallicities). More recently, it was pointed out that the neutrino-induced spallation reactions on light nuclei such as ^{4}He and ^{12}C may efficiently produce lithium and boron in the oxygen/carbon layer of a Type-II SNe [21]. Such a process is interesting as a possible source of Li-Be-B in addition to spallation by cosmic rays, and also as a new probe to constrain the parameters of flavor oscillation in the neutrino sector. For a precise analysis of those light element abundances, it is necessary to carry out detailed simulations using accurate data of the neutrino-nucleus reaction rates.

2.2.2 Measurement Plan for the ^{12}C(ν_e,e$^-$)^{12}N Cross Section in JSNS^2

So far, experimental data on the neutrino-induced nuclear reaction cross sections has been obtained by using neutrinos produced by accelerators or radioactive isotopes. DAR neutrinos from stopped pions and muons generated with high-energy accelerators are very useful for studies of nuclear reactions induced by supernova (SN) neutrinos, because their energy spectra overlap with those of SN neutrinos as shown in Fig. 6.

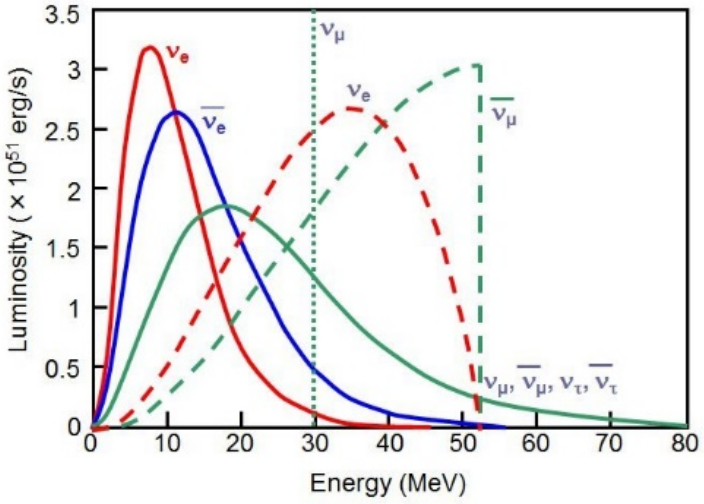


Figure 6: Energy spectra of neutrinos from Type-II SNe (solid curves) and DAR pions and muons (dashed curves, arbitrary units in luminosity).

Table 3 shows the list of the presently available experimental data for neutrino-induced nuclear reaction cross sections.

As shown in Table 3, even in best case, the accuracy of the experimental data on ^{12}C cross sections is not better than what is required for SN simulations, and therefore new experimental data with better accuracy is still needed. JSNS^2 is expected to provide an experimental opportunity to measure the neutrino-induced nuclear reaction cross sections with better accuracy thanks to a high-intensity neutrino beam from the J-PARC/MLF and a detector with excellent sensitivity as well as a high signal-to-noise ratio. Accord-

Table 3: Summary of the existing data for neutrino-induced nuclear reaction cross sections.

Reaction	Neutrino Source	Accuracy	Reference
^{12}C(ν_e,e$^-$)^{12}N$_{g.s.}$	Accelerator ν	$\sim$10%	[22][23]
^{12}C(ν_e,e$^-$)^{12}N*	Accelerator ν	$\sim$15%	[22][23]
^{12}C(ν,$\nu^{'}$)^{12}C(1$^+$1)	Accelerator ν	$\sim$20%	[22][23]
^{13}C(ν_e,e$^-$)^{13}N	Accelerator ν	76%	[22]
^{56}Fe(ν_e,e$^-$)^{56}Ni	Accelerator ν	37%	[22]
^{71}Ga(ν_e,e$^-$)^{71}Ge	RI (^{51}Cr)	11%	[24][25]
^{127}I(ν_e,e$^-$)^{127}Xe	Accelerator ν	33%	[26]

ing to the result of our realistic Monte Carlo simulation based on the background data measured near the site of the JSNS^2 detector, a very small statistical error of 6.0% is expected with three years of running and a fiducial detector mass of 17 tons. For more details on the estimation of the sensitivity, the reader is referred to [27].

2.3 Physics with neutrinos from charged kaon decay-at-rest

JSNS^2 has the unique ability to precisely measure monoenergetic 236 MeV neutrinos from charged kaon decay-at-rest (KDAR) ($K^+ \to \mu^+\nu_\mu$; BR=63.5% [28]) for the first time. These neutrinos represent (1) an unprecedented weak-interaction-only, known energy probe of the nucleus, (2) a standard candle for developing a thorough understanding of the neutrino interaction and cross sections critical for future long baseline neutrino experiments, and (3) a source for a sterile neutrino search using electron neutrino appearance [29, 30]. These neutrinos have also been cited as important for probing muon neutrino disappearance at short baseline [31] and as a possible dark matter annihilation signature [32].

Despite the importance of the KDAR neutrino across multiple aspects of particle and nuclear physics, these neutrinos have never been studied or even identified before. The decay-in-flight neutrino "background" in conventional beamlines drowns out the KDAR signal in such experiments. Decay-at-rest sources of neutrinos, most notably spallation neutron sources, are excellent locations for studying KDAR due to their minimal decay-in-flight background and intense beams. However, the historically most intense spallation sources have been too low energy to produce kaons readily. The J-PARC MLF 3 GeV primary proton energy is sufficient to produce kaons efficiently and, also in consideration of the facility's beam intensity (eventually 1 MW, currently 500 kW [33]), represents the best facility in the world to accomplish this physics. The KDAR neutrino can easily be seen in Fig. 7, which shows the neutrino flux at the J-PARC MLF source.

JSNS^2 expects to collect a sample of between 30,000 and 60,000 ν_μ charged current

events in 17 tons of fiducial volume in its 3 year run[1]. These events ($\nu_\mu n \to \mu^- p$ or $\nu_\mu {}^{12}\mathrm{C} \to \mu^- X$) are easily identifiable due to the characteristic double coincident signal of the prompt muon plus proton(s)/nucleus followed by the muon decay electron ($\mu^- \to e^- \overline{\nu}_e \nu_\mu$) a few μs later.

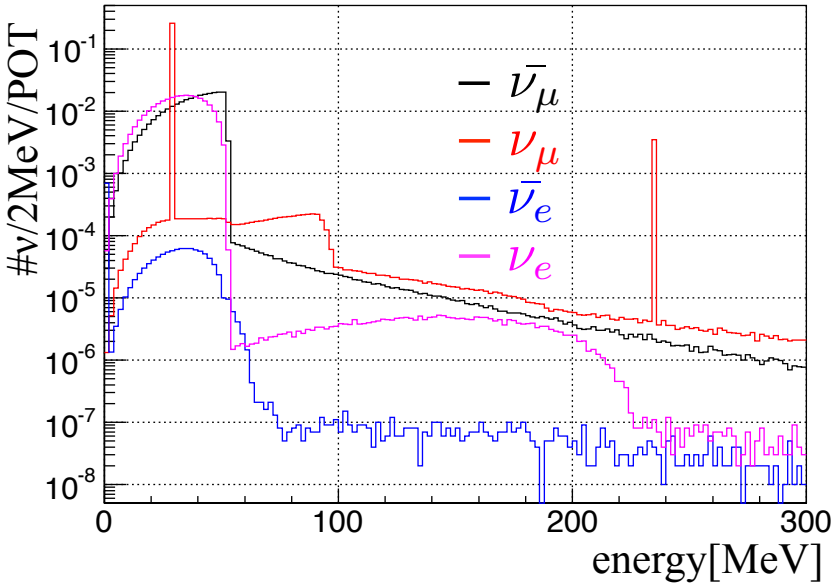


Figure 7: The neutrino flux at the J-PARC MLF source without timing cuts. The 236 MeV muon neutrino from charged kaon decay-at-rest can easily be seen.

The known energy KDAR neutrinos provide the exclusive tool, for the first time, to study nuclear structure and the axial vector component of the interaction using electron scattering variables such as ω ($\omega = E_\nu - E_\mu$). The importance of this unique access to the nucleus is potentially far-reaching. For example, a double differential cross section measurement in terms of ω vs. Q^2 allows one to distinguish effects of the form factors, which depend only on Q^2, and of the nuclear model, which depends on both. Figure 8 (left) shows a number of model predictions for the differential cross section in terms of energy transfer for 300 MeV ν_μ CC scattering on carbon. The disagreement between the models, in terms of both shape and normalization, is striking. Notably, the JSNS^2 muon energy resolution may allow the nuclear resonances, easily seen in Fig. 8 (right), to be measured via neutrino scattering. The KDAR neutrino is likely the only way to study these excitations with neutrino scattering and, in general, to validate/refute these models in the < 400 MeV neutrino energy range (see, e.g., Ref. [36]).

Along with studying nuclear physics relevant for future neutrino experiments, the large sample of KDAR muon neutrinos collected with JSNS^2 will provide a standard candle for understanding the neutrino energy reconstruction and outgoing lepton kinematics in the 100s-of-MeV neutrino energy region. While the KDAR neutrino is simply not relevant for experiments featuring significantly higher neutrino energies, most notably

[1] The large variation in the expected number of events is due to the highly uncertain kaon production at this energy. The lower and upper bounds come from Geant4 [34] and MARS [35] predictions, respectively.

for MINOS, NOvA and DUNE [37, 38, 39], it is highly relevant for experiments with a large or majority fraction of few-hundred-MeV neutrinos, for example, T2K [40], MOMENT [41], the European Spallation Source Neutrino Super Beam (ESSνSB) [42], and a CERN-SPL-based neutrino beam CP search [43]. In particular, MOMENT and ESSνSB both feature ν_μ spectra which peak at about 200-250 MeV.

The KDAR neutrino can also be used to search for electron neutrino appearance ($\nu_\mu \to \nu_e$) for providing a probe of the sterile neutrino that will be highly complementary to the JSNS^2 IBD search ($\overline{\nu}_\mu \to \overline{\nu}_e$). The advantage of the KDAR technique over other sterile neutrino searches is that the signal energy (236 MeV) is known exactly. A background measurement on either side of the signal energy window around 236 MeV can allow an interpolated determination of the expected background in the signal region with high precision. However, as compared to ν_μ CC interactions, ν_e events ($\nu_e n \to e^- p$ or $\nu_e\,^{12}\mathrm{C} \to e^- X$) are more challenging to identify over background, since they do not feature a double coincidence signal. While the KDAR ν_e events are expected to be distinct, in the sense that their reconstructed energy will lie close to 236 MeV, beam-induced neutrons can interact inside of the detector to produce an energetic single flash of light (e.g. a proton), mimicking a 236 MeV ν_e event. Pulse shape discrimination can be used to mitigate this background, but the background event rate expectation remains significant. This is worrisome because the oscillated signal expectation is < 100 events in consideration of the global best fit region at high-Δm^2. The possibility of probing ν_e appearance using KDAR neutrinos at the MLF remains an intriguing possibility, however, especially given strong pulse shape discrimination.

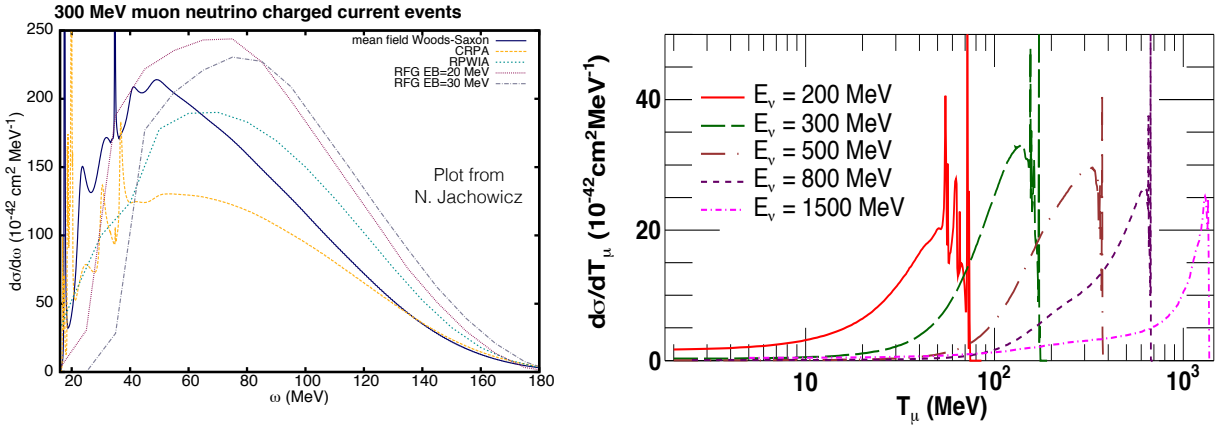


Figure 8: Left: The differential cross section in terms of energy transfer ($\omega = E_\nu - E_\mu$) for 300 MeV ν_μ CC scattering on carbon. Predictions from various models are shown. This plot is adapted from Ref. [44]. Right: The differential cross section in terms of muon kinetic energy for various neutrino energies within the Continuum Random Phase Approximation model; this plot is adapted from Ref. [45].

The KDAR neutrino opens up new avenues for research in neutrino oscillation, interaction, and nuclear physics, and the importance of these measurements is clear. Perhaps most intriguing, the nucleus has simply never been studied using a known energy, weak-interaction-only probe and KDAR provides the exclusive technique to explore this frontier. JSNS^2 represents the world's best hope to take advantage of the KDAR neu-

trino in the near future. Other existing facilities worldwide simply cannot match the large expected KDAR signal and small expected decay-in-flight background rate at the J-PARC MLF.

3 Experimental Components

3.1 The J-PARC MLF as a DAR Neutrino Source

The J-PARC MLF is the best suited facility to search for neutrino oscillations using neutrinos from stopped muon decay in the mass range $\Delta m^2 \sim \mathrm{eV}^2$ for the following reasons:

1. High available beam power (1 MW)
2. Suppression of μ^- free decay through absorption by the mercury target
3. A low duty factor, pulsed beam which enables elimination of decay-in-flight components and separation of μDAR from other background sources. The resulting $\nu_e, \bar{\nu}_e$ have well-defined spectra and known cross sections.

3.1.1 The RCS beam and the target

The proton intensity is expected to reach 0.33 mA (1 MW) after major upgrades to the mercury target. The protons are produced with a repetition rate of 25 Hz, where each spill contains two 100 ns wide pulses of protons spaced 540 ns apart. The 1 MW beam provides 3.8×10^{22} protons-on-target (POT) during 5000 hours / year operation (i.e. 4.5×10^{8} spills are provided during one year). The short pulsed beam provides the ability to distinguish between neutrinos from pion decay and those from muon decay.

Figure 2 shows a bird eye view of MLF in J-PARC. After penetrating a 2 cm thick muon production target made of carbon graphite, protons are introduced to the mercury target. A schematic drawing of the J-PARC spallation neutron source is shown in Fig. 9. 3 GeV protons interact in the mercury spallation target, producing pions and kaons that decay into ν_e and ν_μ and their anti-neutrinos after heavy shielding. Surrounding the target are cooling pipes, beryllium reflectors, and steel shielding.

A beam of protons enters from the left and strikes the target. The beam has a wide spot size (e.g.: 3.3 cm by 1.3 cm in root mean square) for reduction of the local heat load in the target. The target, shown in Fig. 10, has dimensions of 54 cm in width by 19 cm in height by 210 cm in length. Mercury is contained within a multiple wall structure made of stainless steel. To remove heat, the mercury of the target is constantly circulated at a rate of 154 kg/sec. Cryogenic liquid hydrogen moderators are located at the top and bottom of the target. The target and moderators are surrounded by a beryllium reflector and iron shielding which extends to a minimum radius of 5 m around the target. There are 23 neutron channels looking at the moderators, rather than at the target. Shutters are provided on each channel.

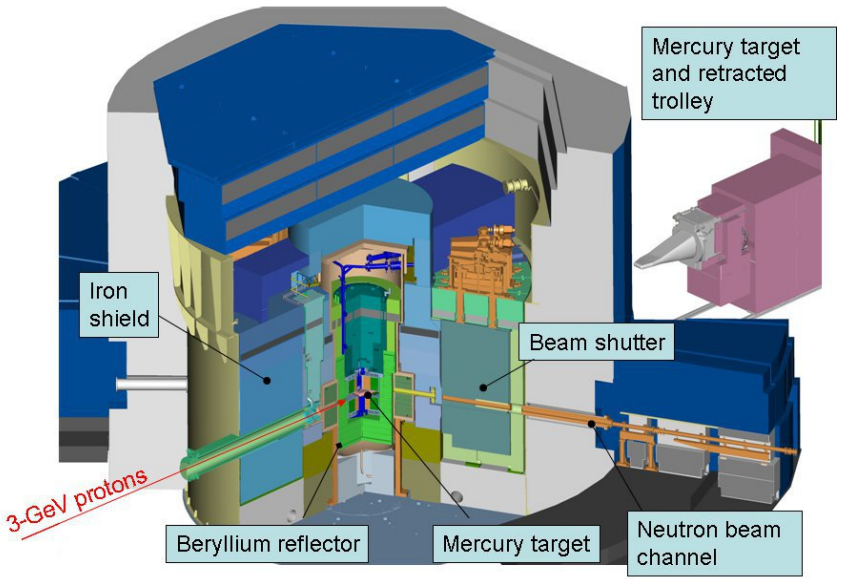


Figure 9: A schematic drawing of the J-PARC spallation neutron source.

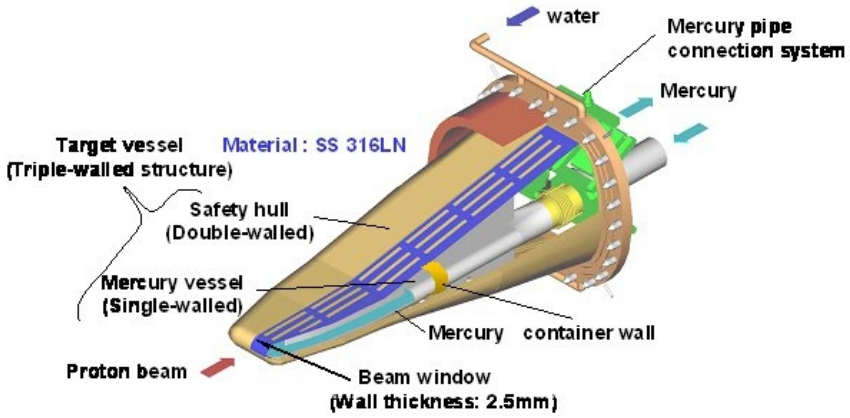


Figure 10: A schematic drawing of the mercury target in the J-PARC MLF.

3.1.2 Neutrino Beam

There are two time structures in the neutrino beam. One is the 'on- bunch' component (neutrinos produced during the proton bunch and within the pion or kaon lifetime) and features neutrinos from:

- $\pi^+ \to \mu^+ \nu_\mu$ decay at rest with monochromatic neutrino energy of 30 MeV
- $\mu^- + A \to \nu_\mu + A$ with a 105 MeV endpoint
- $K^+ \to \mu^+ \nu_\mu$ decay at rest with monochromatic energy of 236 MeV
- $K^+ \to \mu^+ \pi^0 \nu_\mu$ decay at rest with an endpoint energy of 215 MeV
- $K^+ \to e^+ \pi^0 \nu_e$ decay at rest with an endpoint energy of 228 MeV
- Small components from π and K decay in flight

The other time structure is the 'off-bunch' component (during the muon lifetime), which is produced by muon decay at rest:

- $\mu^+ \to e^+ \nu_e \bar{\nu_\mu}$
- If μ^- stops in a light material, μ^- also decays by $\mu^- \to e^+ \bar{\nu_e} \nu_\mu$

This 'off-bunch' component can be selected by gating out the first 1 μs from the start of the proton beam. Figures 4 and 7 show the expected neutrino energy spectrum from the MLF target with and without the timing cut (T $> 1\mu$s). Figure 3 shows the time distributions from various sources.

Tables 4 and 5 are summary tables for the production of neutrinos from μ decays.The μ decay at rest neutrino beam was simulated using the following steps.

1. Particle production by 3 GeV protons
   The interaction of the 3 GeV proton beam with the mercury target and beam line components has been simulated with FLUKA [46] and QGSP-BERT (in Geant4 [34]) hadron interaction simulation packages.

2. $\pi^\pm$ interactions and decay
   After production, both π^+ and π^- lose their energy mainly by ionization. In addition, they disappear by the charge exchange reaction $\pi^\pm(n,p) \to \pi^0(p,n)$, $\pi^0 \to \gamma\gamma$. The survived π^+ stop and decay with a 26 ns lifetime. On the other hand, the survived π^- are absorbed by forming a π-mesic atoms and getting absorbed promptly. Decay-in-flight takes place with very suppressed rate of about $\sim 8 \times 10^{-3}$ of produced $\pi^\pm$.

3. $\mu^\pm$ absorption and decay
   All μ^+ decay by $\mu^+ \to e^+ \nu_e \bar{\nu_\mu}$. Because of the muon lifetime and energy loss process, the decay-in-flight is negligible. μ^- are captured by nuclei by forming a mu-mesic atom and eventually produce ν_μ with an endpoint energy of 100 MeV. The absorption rate depends on the nucleus and becomes faster for heavier nuclei. The total nuclear capture rates for negative muons have been measured in terms of effective muon lifetime [47].

The resulting neutrino fluxes for each type of neutrino species are shown in Figure 4. Tables 4 and 5 are expected production rates of $\pi^{\pm}$ by 3 GeV protons on the mercury target and the resulting μ^+ and μ^- decay neutrinos per proton, based on a pion production model.

	$\pi^+ \to \mu^+ \to \bar{\nu_\mu}$	$\pi^- \to \mu^- \to \bar{\nu_e}$
π/p	6.49×10^{-1}	4.02×10^{-1}
μ/p	3.44×10^{-1}	3.20×10^{-3}
ν/p	3.44×10^{-1}	7.66×10^{-4}
ν after 1μs	2.52×10^{-1}	4.43×10^{-4}

Table 4: An estimate of μDAR neutrino production by 3 GeV protons using the FLUKA hadron simulation package.

	$\pi^+ \to \mu^+ \to \bar{\nu_\mu}$	$\pi^- \to \mu^- \to \bar{\nu_e}$
π/p	5.41×10^{-1}	4.90×10^{-1}
μ/p	2.68×10^{-1}	3.90×10^{-3}
ν/p	2.68×10^{-1}	9.34×10^{-4}
ν after 1μs	1.97×10^{-1}	5.41×10^{-4}

Table 5: An estimate of μDAR neutrino production by 3 GeV protons using the QGSP-BERT hadron simulation package.

Needless to say, there are many sources of ambiguities in pion production. For example, the production rates are sensitive to production by secondary particles in the thick target, target geometrical modeling, and uncertainty in pion production from mercury. We use these calculations as estimates and the actual μ^- backgrounds should be determined from the data based on their known spectrum and known cross section.

For this TDR, numbers from Table 4 are used to estimate the central values, and those in Table 5 are used for the cross checks.

3.1.3 Estimated Neutrino Flux

The proton intensity is assumed to be 0.33 mA, delivering 3.8×10^{22} protons on target (POT) per 5000 hour operation in one year. The stopping ν/p ratio is estimated from the FLUKA simulations to be 0.344. The $\bar{\nu}_\mu$ flux from the $\pi^+ \to \nu_\mu + \mu^+; \mu^+ \to e^+ + \nu_e + \bar{\nu}_\mu$ chain at 24 m is then equal to 1.8×10^{14} ν year/cm^2.

3.2 Detector Location and Constraints

We plan to place the detector shown in Fig. 11 on the third floor of the MLF. As previously noted, the detector is at a 24 meter baseline and contains 17 tons of Gd-loaded

LS inside the inner acrylic vessel, and ∼30 tons unloaded LS in the space between the acrylic vessel and stainless tank. There are 193 8-inch PMTs between the acrylic and stainless tanks and 48 5-inch PMTs in the veto region. The specific PMT locations will be described later.

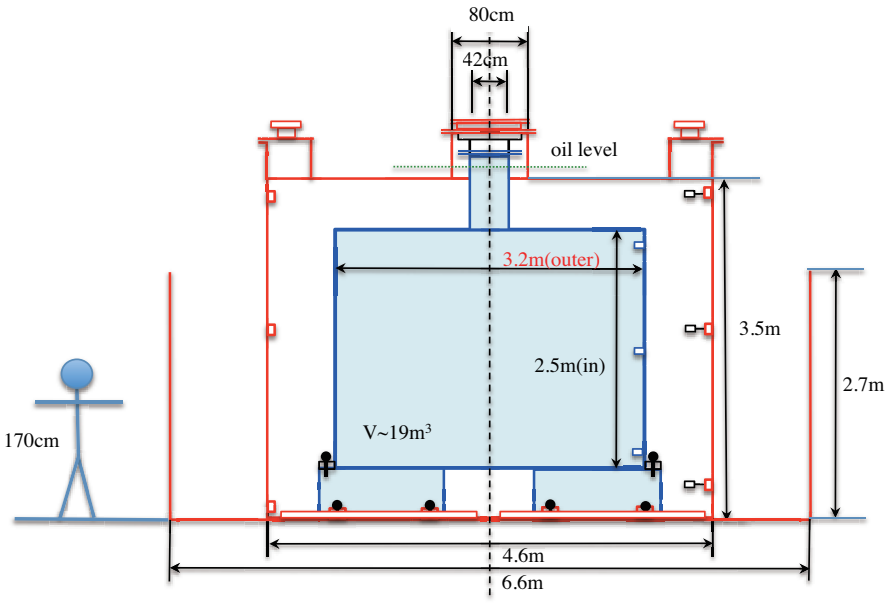


Figure 11: Conceptual structure of the JSNS^2 detector tanks.

Figure 12 shows two dimensional drawings of the MLF 3rd floor, and the red box shows the detector location based on the background measurements which were performed in 2014 (see Section 4.2 for more details). In this area, we need to put iron plates under the detector in order to provide shielding from beam gammas coming through the hatches. The left-hand side of the figure is upstream of the beam and the circle around the center of the figure corresponds to the location of the mercury target. You can see the hatches in the red box, which correspond to the concrete hatches used to exchange the mercury target. Under the hatches, there is a radiation hot room as shown in Figs. 20 and 25, and therefore we have to prepare safety systems so that LS does not leak into the radiation hot room. (Oil spill prevention system is described in Section 3.4).

The experts of MLF call this area "Large Component Handling Room", that is the maintenance area for the mercury target, the target cooling system, the beamline equipment and so forth. Therefore, the JSNS^2 detector must be moved outside the MLF during the maintenance period which is held typically from July to September (three months) each year in order to avoid interference between the maintenance work and JSNS^2 experiment.

To put the JSNS^2 detector on the MLF 3rd floor, the withstand load and the sinkage around the area of the building are quite important. Thus, we estimated the former with the Mitui-Zosen company and the results will be shown later.

For the latter, we have also estimated how much the MLF building will settle when the JSNS^2 detectors are placed inside the room. The total weight of the MLF building is about 40,000 tons. The Neutron Source Group in JAEA has measured the amount of

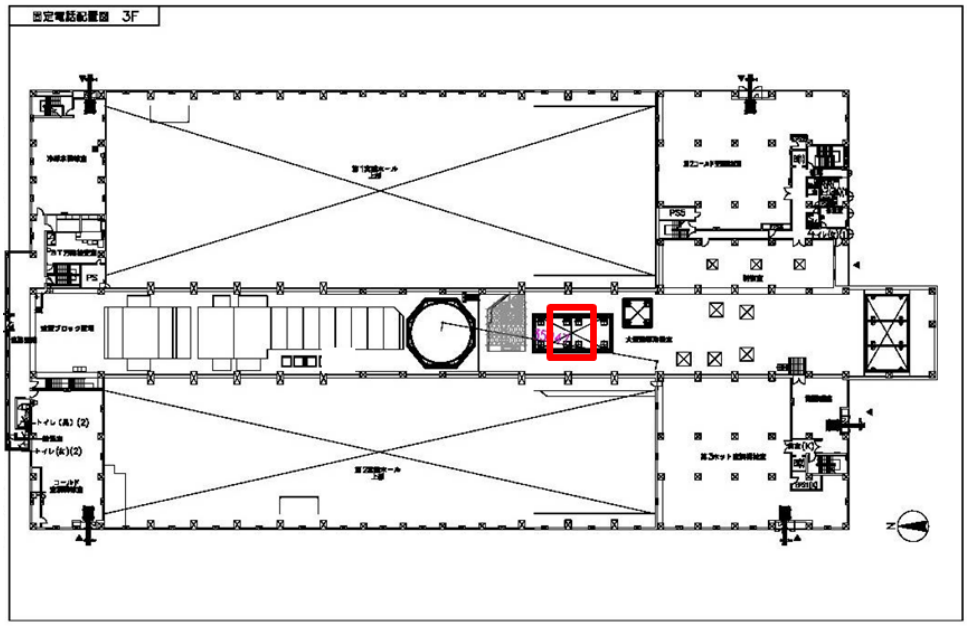


Figure 12: Two dimensional drawings of the MLF 3rd floor. The red box shows the detector location based on the 2014 background measurements described in Section 4.2

subsidence of the MLF building continuously from the construction phase, and a summary of the findings has been published in Reference [48]. According to the publication, the current sinkage has substantially stopped, and it estimated that a sinkage of 0.3 mm/1000 tons occurs when the weight load is increased in the MLF building. The weight of JSNS^2 detector is about $\sim$190 tons, thus the sinkage effect of the JSNS^2 detector is less than 0.1 mm, which can be considered to be negligible.

3.2.1 Withstand Weight Load

The JSNS^2 detector consists of liquid scintillator, containment tanks, support frames, and iron plates (γ shields) that have a total weight of about 190 tons. The position of the JSNS^2 detectors is currently planned to be around the large hatch (12 m $\times$6 m) as shown in Fig. 12. The hatches are moved to access to the irradiated components handling room as shown in Fig. 25. (The room has orange colored light in this picture.)

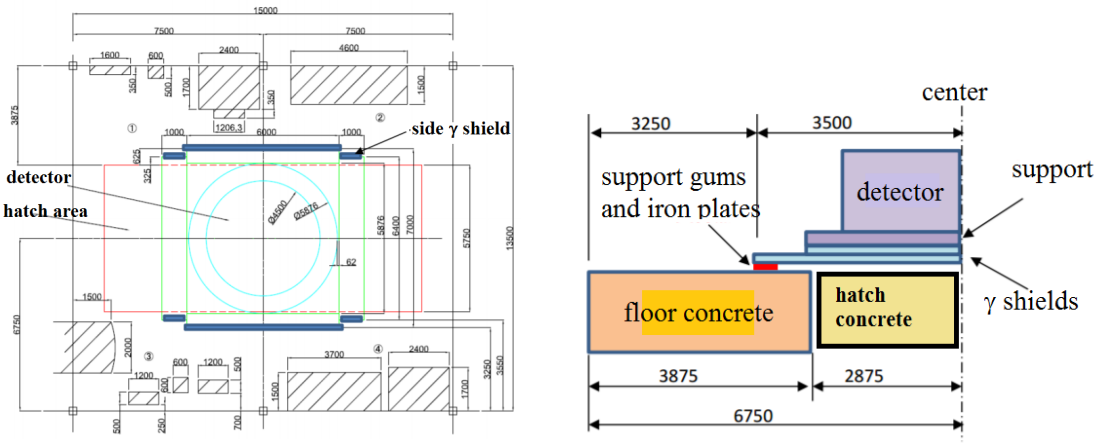
The hatches themselves cannot sustain 190 tons. For this reason, a detector support structure using side areas around the large hatches is necessary. Figure 13 shows the top and side views around the detector including the γ shields (iron plates) and detector support structure. This structure is designed to be as light as possible. The following considerations are taken into account by this design:

- The detector including stainless, acrylic vessels, anti oil-leak tanks, PMTs and LS is supported by I-beams (height of 25 cm) under the detector, and is transported from the MLF entrance to the 3rd floor by a 130 ton crane. Note again that the support structure is transported with the LS and needed for the transportation to support LS, and the iron plates are separated from the detector.

- To shield the detector from beam γs coming through the hatches, iron plates are placed underneath. To reduce the weight as much as possible, two iron plates are used. One plate has dimensions 6.0 (beam direction) $\times$ 5.88 (orthogonal direction to the beam) $\times$ 0.15 (thickness) m^3 and is placed just below the detector and the other has dimensions 6.0 $\times$ 7.0 $\times$ 0.15 m^3 and is put under the first plate.

- According to the MC simulation, a total coverage of 8.0 m in the beam direction is preferrable, and therefore we put additional plates of dimensions 1.0 (beam direction) $\times$ 6.4 (orthogonal direction to the beam) $\times$ 0.3 (thickness) m^3 on both sides of the detector along the beam direction.

Table 6 shows the weight of the detector components.



(a) The detector location (top view)

(b) The detector location (side view)

Figure 13: Top (left) and side (right) views around the detector. Blue bands on the left show the gums and iron support plates which reduce the bearing pressure on the floor. This structure is described in Appendix A. The green area (left) shows the γ shield regions, and the light blue corresponds to the detector and anti oil-leak tanks. Red area (left) indicates the concrete hatches to separate the 3rd floor and radiation hot area under the detector.

Components	Weight (tons)	comments
Supporting structure	10	
Acrylic vessel + LS	20.3	17.0 (LS) + 3.3 (tank)
Stainless tank + LS	36.9	30.0 (LS) + 6.9 (tank)
γ shield 1	41.5	5.88 $\times$ 6.0 m^2 $\times$ 15 cm (t)
γ shield 2	49.5	7.0 $\times$ 6.0 m^2 $\times$ 15 cm (t)
Side γ shields	30.1	6.4 $\times$ 1.0 m^2 $\times$ 30 cm (t) $\times$ 2
Total	188.3	

Table 6: Weight for the detector components.

This subsection describes whether the MLF building can support the withstand load

from the detector. Discussion of this topic has already taken place with the JAEA facility section and with "Nikken-Sekkei", which designed and built the MLF building.

The MLF building tolerance for additional weight loads is determined by two parameters: the bending moment of the floor concrete and the withstand load of the concrete floor itself. These parameters are defined by "Nikken-Sekkei" company.

Before the comparison between the tolerance and weight for the detector, we must investigate the weights and moment which are already used for the existing materials on the 3rd floor because they must be subtracted from the tolerance. The existing materials on the 3rd floor are shown as the shaded regions in Fig. 13 (a). Then, we subtract them from the tolerance of the building as shown in Fig. 14. The maximum tolerance values of the building before the subtraction are given by "Nikken-Sekkei".

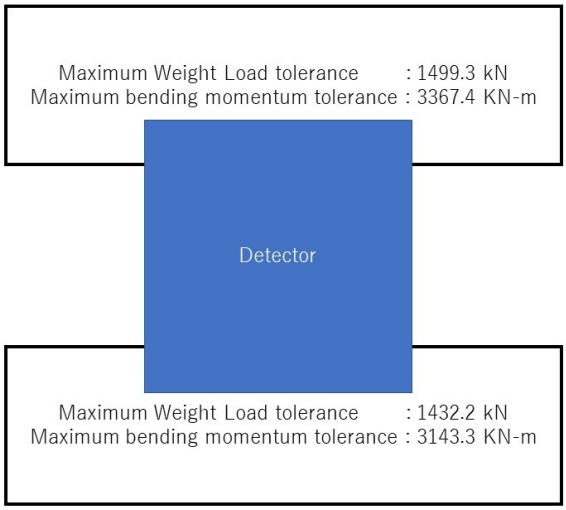


Figure 14: The maximum weight load tolerance values on the 3rd floor (after subtraction).

As mentioned, the expected total weight of the detector is about 190 tons. Therefore, the maximum weight load tolerance after subtraction is much larger than the expected detector weight (919.5 kN (detector) vs. 1432.2 kN (tolerance)). The bending moment of the 3rd floor assuming the detector design shown in Fig. 13 is 3032.7 KN·m (the bending moment is determined by the location of the support points of the detector (weight center) and weight of the detector). This is within the tolerance of the MLF building. Note that this calculation includes large safety factors.

After showing the calculation to the JAEA facility section and "Nikken-Sekkei", they agree that there are no issues with putting the detector on the MLF 3rd floor.

3.3 Tanks

3.3.1 General structure

Figure 11 shows a schematic drawing of the JSNS^2 detector tank system. The tank

system consists of, from inner to outer, an acrylic vessel, stainless steel (s.s.) tank and an anti oil-leak tank. The acrylic vessel contains the Gd-loaded LS which works as the neutrino target.

Unloaded LS, which vetoes the background signals is contained in the region between the acrylic vessel and the s.s. tank. 193 8-inch PMTs and 48 5-inch PMTs will be installed in the space between the s.s. tank and acrylic vessel. The tank system has to be moved at least once per year to make room for maintenance work on the MLF beam line.

3.3.2 Stainless Steel Tank and Anti Oil-Leak Tank

Figure 15 shows a drawing of the tank design. The diameter, height and volume of the cylindrical part of the s.s. tank are 4.6 m, 3.5m and 58 m^3, respectively. The diameter and height of the anti oil-leak tank are 6.6 m and 2.7 m, and the volume is 80 m^3, which can contain all the liquid even if there is a leak from the s.s. main tank. The thickness of

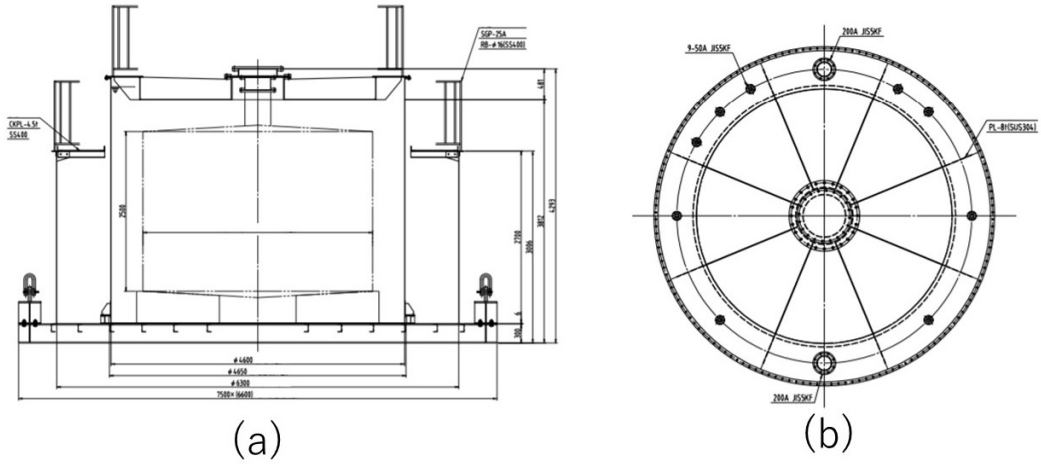


Figure 15: Design of the stainless steel tank. (a) Side view, (b) Top view

the side wall of the s.s. tank is 5 mm and the bottom plate is 6 mm. In order to prevent agitation of the oil surface while the tank is moved by a crane, the lid of the s.s. tank is designed to be below the LS level and the LS can push up the lid. The lid is reinforced by 8 welded beams. The nominal oil level is 10 cm higher than the s.s. lid. The diameter of the s.s. tank chimney is 80 cm. At the circumference of the stainless steel tank, there is 30 cm wide LS stabilization region for the veto area. This stabilizes the oil level with respect to temperature changes as described in the following sections.

3.3.3 Acrylic Vessel

Figure 16 shows side and top views of the acrylic vessel design. The diameter, height and volume of the cylindrical part of the acrylic vessel are, 3.2 m and 2.5 m and 19.3 m^3, respectively. The thickness of the acrylic is 3 cm. The maximum strength of the acrylic

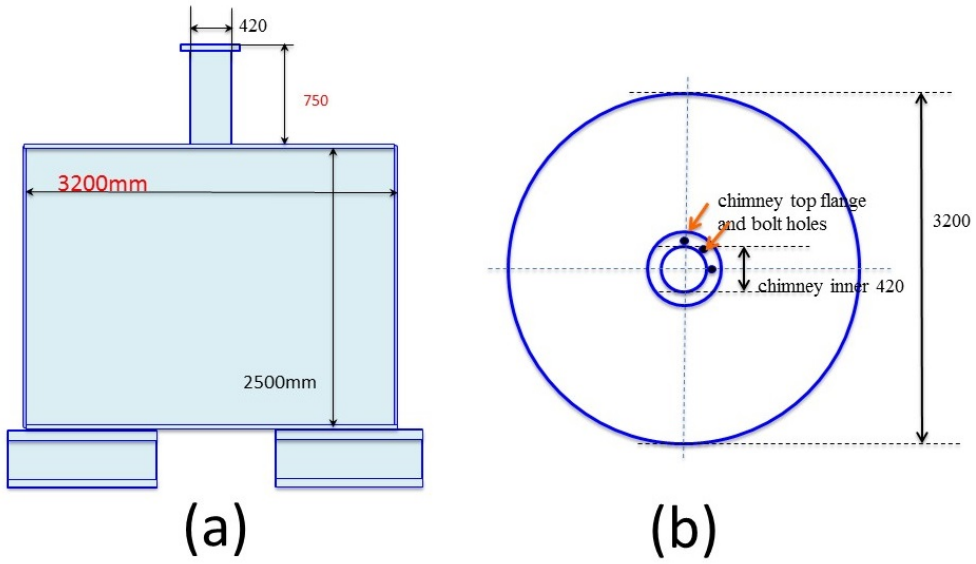


Figure 16: (a) Acrylic vessel side view, (b) view of lid.

vessel corresponds to ±15 cm head difference. Due to the pressure changes, the center of the acrylic lid moves at most ±2 cm.

The total volume of the vessel part of acrylic material is 1.2 m^3 and the total weight is 1.5 ton. Since the specific gravity of the acrylic is 1.2 and that of the LS is 0.86, the net weight of the acrylic vessel in the oil is 406 kg. This weight stabilizes the acrylic vessel in the oil. The acrylic vessel stands on the bottom of the stainless steel tank via six acrylic fin blocks as shown in Fig. 17. The support blocks are bolted to the bottom of the s.s. tank before the PMT installation. After the PMT installation, the acrylic vessel is put

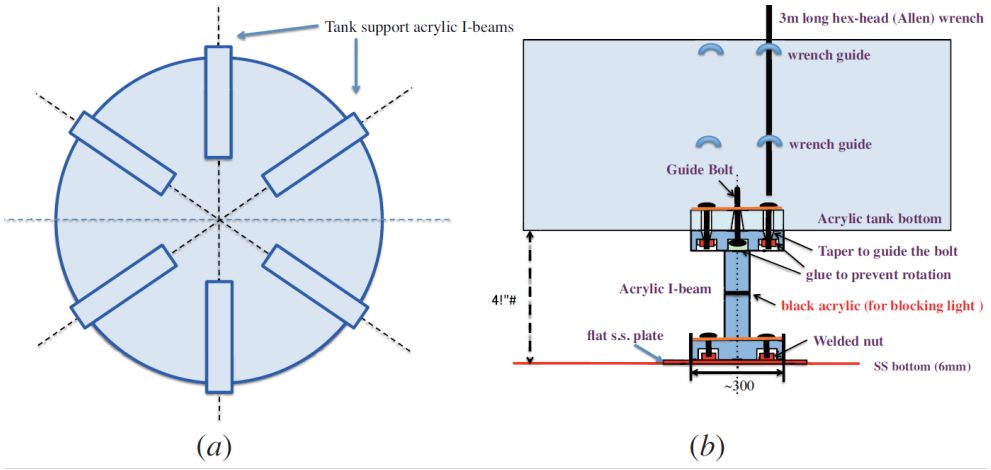


Figure 17: (a) Acrylic vessel support acrylic blocks, (b) Details of the support blocks and their installation.

in the s.s. tank and bolted to the support blocks from the above using a specially-made long Allen wrench (hex head wrench). Wrench guide rings are installed on the side wall of the acrylic vessel.

The acrylic vessel has a 42 cm diameter chimney which is connected to the s.s. tank through a 15 cm long bellows as shown in Fig. 18. The bellows have a movable span of ±7.5 cm and absorb mechanical changes and possible deformations of the tanks due to internal pressure variations.

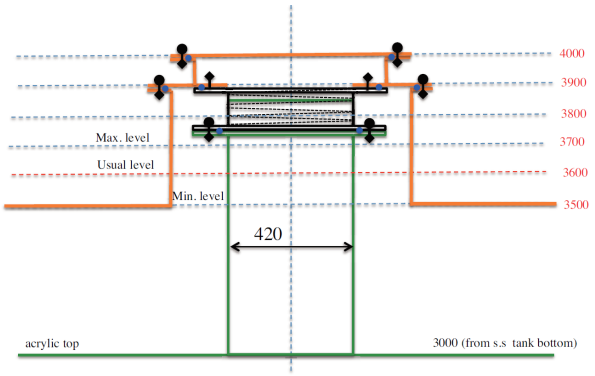


Figure 18: Chimney of the JSNS^2 detector tanks.

The elastic limit of the acrylic vessel lid deformation due to the internal pressure is ±2 cm.

Table 7 summarizes the parameters of the tanks and LS.

Table 7: Parameters of the tanks and liquids.

Item	Radius[m]	Height[m]	Volume [m^3]	Weight [ton]
Acrylic Vessel	1.6	2.5	19.3	1.5
s.s. tank	2.3	3.5	58	-
S.P.R.	3.15	2.7	84	-
Gd-LS	-	-	19.3	17
Buffer LS	-	-	35	30

3.3.4 Liquid level stabilizing mechanism

The thermal expansion coefficient of linear alkylbenzene is $\Delta V/V \sim 9 \times 10^{-4}/^{o}$C [49]. On the other hand, the maximum temperature variation of the experimental area is expected to be ±10 degrees and the liquid volume will change as much as ±0.9%. This volume change causes a change in the oil level. For example, the change of the Gd-LS level in the acrylic chimney is 14 cm/^{o}C and so a level stabilizing mechanism is necessary.

The oil level to be maintained is shown in Fig. 11. There is a 30 cm wide stabilization area along the circumference of the stainless tank which will stabilize the veto LS level.

The area of this outer surface (S_B) is ~ 4 m^2 and the change of the oil level caused by $\pm 10°$ temperature change is kept within ± 10 cm. As for the Gd-LS liquid, there is an oil level stabilizer tank on the s.s. tank lid as shown in Fig 19. The inner surface of the

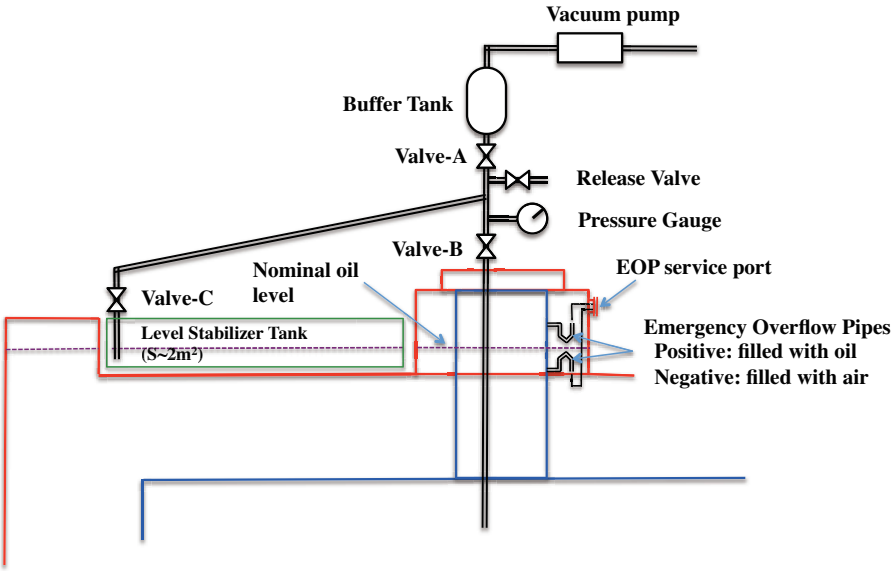


Figure 19: Oil level stabilizing mechanism

stabilizer tank is made of plastic in order to prevent potential instability of the Gd-LS. The area of the stabilizer tank (S_T) is $S_T = S_B \frac{V_T}{V_B} \sim 2.5$ m^2 to prevent any level difference due to temperature change.

The liquid in the stabilizer tank and the acrylic vessel are connected by a *reverse siphon* (RS) system. After oil filling, the RS system is established according to the following procedure.

1. At first, all the valves are closed.
2. LS is supplied to the stabilizer tank until the end of the siphon pipe is completely soaked.
3. Valves-A, B, C. are opened.
4. The vacuum pump is switched on and LS is sucked from both tanks.
5. When the LS becomes higher than Valve-A, the valve is closed and the RS is established.
6. The pressure gauge keeps monitoring the RS to ensure it is still established.

The measured pressure value also indicates the level of Gd-LS in the tank.

If, for some reason, the RS is broken, the LS inside the pipe is returned to each tank by opening the Release Valve and the RS establishing process ((1)-(5)) is performed again.

The reverse siphon method has been utilized effectively in the Double Chooz experiment.

3.3.5 Emergency overflow pipes

The V and Λ shaped pipes on the acrylic chimney in Fig. 19 are emergency overflow pipes. They are only used in the case that the RS system is somehow broken. The V-shape pipe is filled with LS using a pipe from the EOP service port and the Λ-shaped pipe is filled with air to separate the target and veto regions. If the Gd-LS level becomes high for some reason and reaches the inlet of the V-shape pipe, Gd-LS starts to flow out to the buffer LS region. If the Gd-LS level becomes low and reaches to the inlet of the Λ-shape pipe, the veto LS starts to flow in to the target region. In this way, the Gd-LS level is kept between the inlets of the V and Λ-shape pipes at all times.

If the overflow case were to happen, the Gd-LS and veto LS would mix. However, this would only occur in an emergency case and we expect it will not happen throughout the lifetime of the experiment.

3.4 Safety Protection System

Here we describe the safety protection systems. First, the additional "anti oil-leak tank" normally required by the Fire Law (one "anti oil-leak tank") is described.

Figure 20 shows the overall oil spill prevention systems in addition to the Fire Law requests.

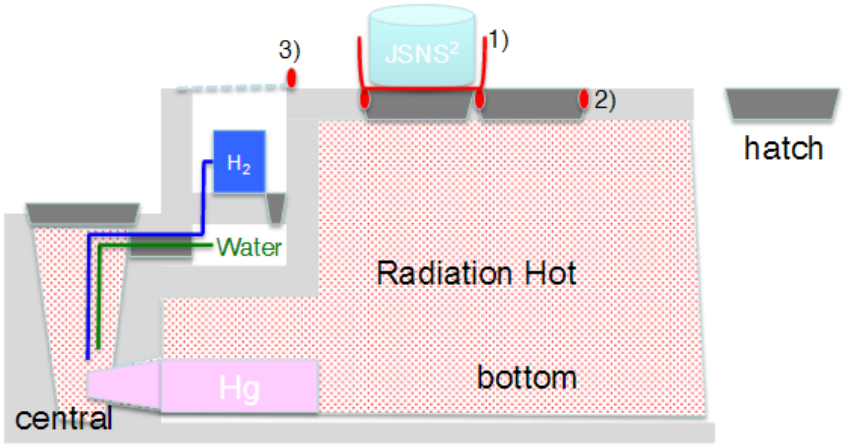


Figure 20: The additional oil spill prevention systems on top of the Fire Law requests including (1) A second "anti oil-leak tank", (2) Sealant in the space between the hatches and concrete, (3) The third oil spill prevention wall to prevent LS from flowing into the mercury target area.

There are three systems as follows;

1. A second anti oil-leak tank
2. Sealant in the space between the hatches and concrete
3. An anti oil-leak wall which prevents LS from flowing to the mercury target.

The details of the each system are described in subsections below. We also describe the safety slow monitor systems for the detector later.

3.4.1 Second Anti Oil-Leak Tank

As required by the Fire Law, we have the first anti oil-leak tank around the detector (shown as the red circle in the Fig. 21). In addition to the Fire Law requirement, we will have the second anti oil-leak tank which surrounds the detector tank and the first anti oil-leak tank (shown as the yellow box in the figure).

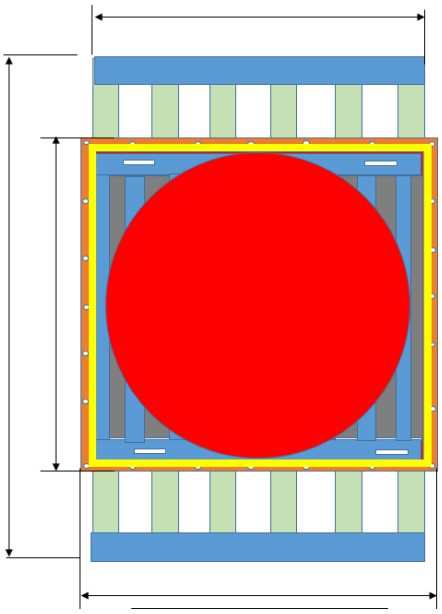


Figure 21: The top view of the tank including the first anti oil-leak tank (red), 2nd anti oil-leak tank (yellow) and the tank base. The height of 2nd anti oil-leak tank is about 1.4 meter with a thickness of a few mm.

This second tank is made of thin (a few mm) iron and is fixed by bolts and nuts (white circles inside the orange line in the figure). As explained in the next subsection, sealant can be used around the nuts and bolts to make the second tank even less susceptible to leaks.

3.4.2 Sealing the Space between Hatches and Concrete

Figure 22 shows the space between the hatches and the concrete which corresponds to several millimeters.

We propose to fill the space using air tight sealing materials. This sealing material has been successfully used by the MLF muon group [50]. Figure 23 shows the container for the sealing material.

We have created a mockup test to demonstrate the effectiveness of the sealing material against LS. The setup of the test is shown in Fig. 24. The sealing material is filled in the space between container and the gums, and LS is put on the sealing material layer. With the sealing material, no LS leaks were found during a period of over one month. In the case of an emergency, the expected duration that the LS is stored on the MLF third floor is a few days. Therefore, the sealant we have chosen ensures that LS will never fall down into the radiation hot areas, even in an emergency situation.

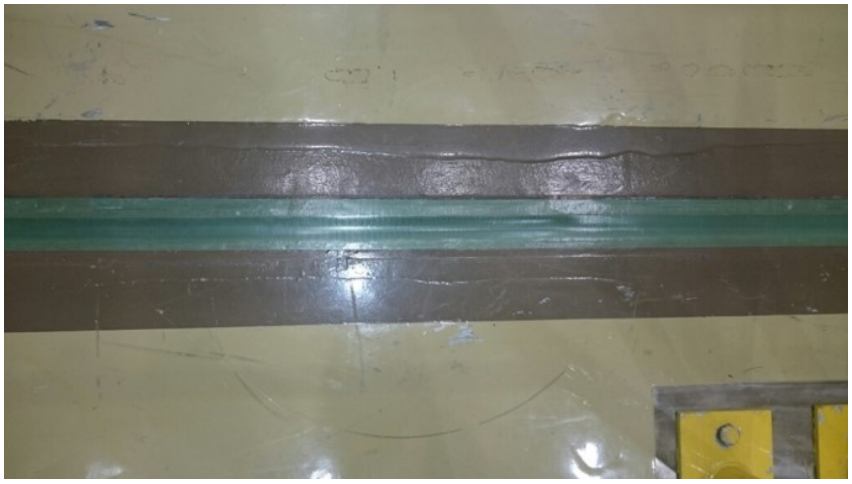


Figure 22: The space between hatches and concrete. The green tapes are used for the temporary sealing which has weak effects.



Figure 23: The container for the sealing material.

An additional concern is potential damage to the sealing material due to a large earthquake causing motion between the sealant and concrete. However, gum lines are put under the hatches to prevent motion of the concrete during an earthquake as shown in Fig. 25. We investigated the maximum coefficient of friction for the case that the gum line is inserted between concretes using various references, and concluded that it is between 0.7-1.5. Given that the MLF building can withstand an earthquake up 0.25G, the hatches will not be moved even if a large earthquake occurs.

PTFE or rubber sheets can be put above the hatches and below the detector in addition to the sealant in order to avoid oil leakage.

3.4.3 The Third Anti Oil-Leak Wall

We will put a steel L-type angular piece for the third anti oil-leak wall which prevents LS from flowing into the target area. The height of the wall is 5 cm just to prevent LS from moving past it. This wall will be fixed by bolts and nuts and will also be sealed using the sealing material.

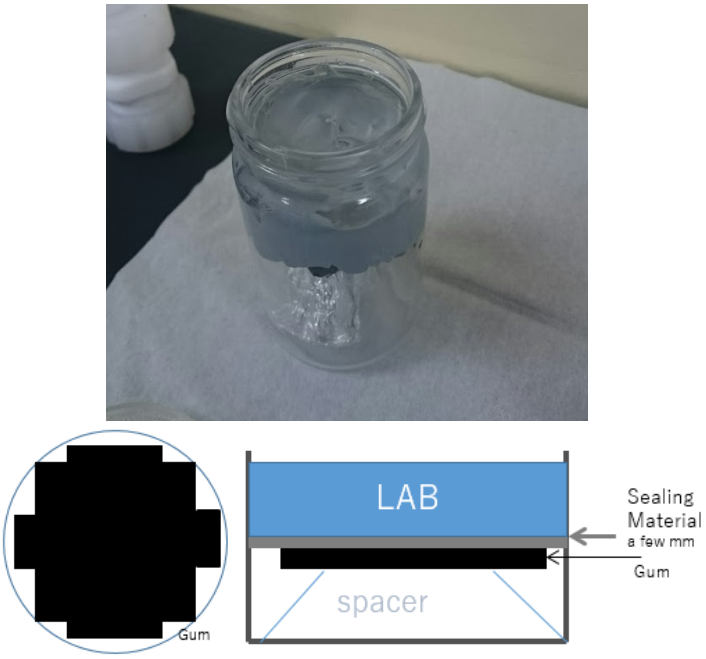


Figure 24: The setup for the mockup test to demonstrate the properties of the sealing material. Top: picture of the setup. Bottom: Cartoon to show the concept.

3.4.4 Slow Monitors

The JSNS^2 detector uses a large amount of organic oil and thus for safety reasons it is necessary to monitor various parameters of the detector at all times. Figure 26 shows a set of possible monitors to accomplish this goal. Generic safety monitors include: organic vapor monitors, and thermometers which will be placed around the detector. Internet cameras will also be used to view the whole detector, the inside the anti oil-leak tank, and the gauges of the slow monitors.

In addition, specific tools will be used to monitor the liquid scintillator. Thermometers will be placed in various depths in the stainless steel tanks to make sure the temperature does not change too much. Liquid level monitors will be placed in the chimneys of the tanks which measure the absolute level of the oils and the level difference between the outer and inner tanks. There will be also one set of absolute atmospheric pressure, humidity, and environmental temperature monitors.

An accelerometer will be used to monitor any shocks the detector experiences while it is moved by the crane or when earthquakes happen.

The gas phase of the tanks will be purged by nitrogen gas continuously. Figure 27 shows an idea for gas monitors. The gas flow will be monitored by internet cameras which view the flow meter and bubblers at the outlet of the nitrogen gas line. The relative pressure between the gas phases of the acrylic vessel and atmospheric pressure will be monitored by a differential pressure gauge. An oxygen monitors will measure the oxygen concentration in the Gd-LS vapor phase. The gauges will be readout online and checked by the shifters.



Figure 25: The gum lines are located under the hatches.

3.5 PhotoMultiplier Tube and its system

3.5.1 Overview of the PMT system

Figure 28 shows the PMT arrangement in the stainless steel tank. The dominant $\bar{\nu}_e$ background from μ^- is separated from the signal using the energy spectrum. The required energy resolution to perform this separation in JSNS^2 is $\Delta E/E < 15\%/\sqrt{E[\mathrm{MeV}]}$. In order to satisfy the requirements, JSNS^2 will use 193 8-inch photomultiplier tubes to detect the scintillation light from the neutrino target. The photocathode coverage achieved in this design is $\sim$ 11 %. Each PMT is covered by a magnetic shield (FINEMET: see later subsection for more details) to reduce the effect of the Earth's magnetic field. The PMTs are totally submerged in LS (organic oil) and the base circuit of the PMT is moulded in an epoxy resin to prevent the contact with the oil. This oil-proof treatment has been used in the KamLAND, Double Chooz, DayaBay and RENO experiments. The signal and HV are supplied by separated two 25 m Teflon jacket cables. Positive HV is supplied from the HV supply to the splitter and sent to the PMT after ripple and noise filters in the splitter circuit.

3.5.2 PMT

Figure 29 shows the structure of the 8-inch R-5912 PMT chosen for this experiment [51].

The PMTs are 8 inches in diameter with borosilicate glass windows and photocathodes at lease 190 mm in diameter. The photocathode material is a bialkali with a spectral response range between 300 nm to 650 nm and a peak wavelength of 420 nm. The typical quantum efficiency at 390 nm is 25 %. The typical gain with high voltage 1500 V is 1.0×10^7 giving single p.e. pulse heights of a few mV. The rise time of a pulse is typically 3.6 ns, the transit time (TT) and the transit time spread (TTS) are measured to be 54 ns and 2.4 ns (FWHM), respectively. The typical peak to valley ratio for a single photo-

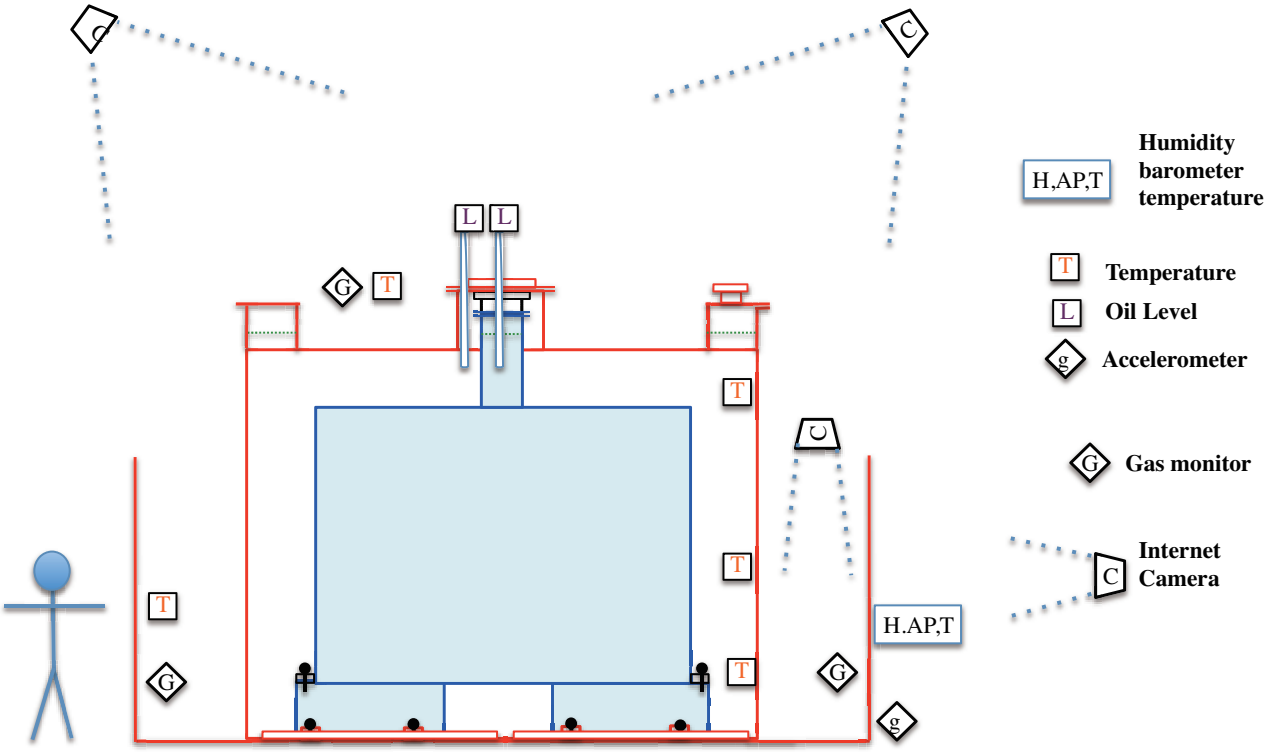


Figure 26: Safety and oil monitors.

electron signal is 2.8 and the typical dark count rate after 15 hours storage in darkness is 4 kHz.

Figure 30 shows an example of the divider circuit. Positive HV is supplied and the cathode potential is set to be ground. HV is provided by one cable and the signal is readout using a separate one. The cable is back-terminated to damp the signal reflections quickly.

For a neutrino with the maximum energy of ∼50 MeV right next to a PMT, the PMT will receive 2000 p.e. On the other hand, the pulse threshold of the PMT is ∼ 0.3 p.e. Therefore, the linear dynamic range required for the PMT is 1 p.e. to 2000 p.e. To realize such a large dynamic range, a tapered voltage divider will be used. Figure 31 compares the linear dynamic range for a standard breeder circuit and the tapered breeder circuit.

3.5.3 Test, Delivery

In this subsection, the PMT delivery scenario, including testing and transportation to the experimental site, is described. The PMTs will be delivered from the vendor to Kitasato University for the initial acceptance test, and then they will be transported to J-PARC for assembly at the experimental site. The PMTs will be attached to the support structure inside the outer stainless tank. In total, we need 193 PMTs 8-inch PMTs for the construction of a single detector.

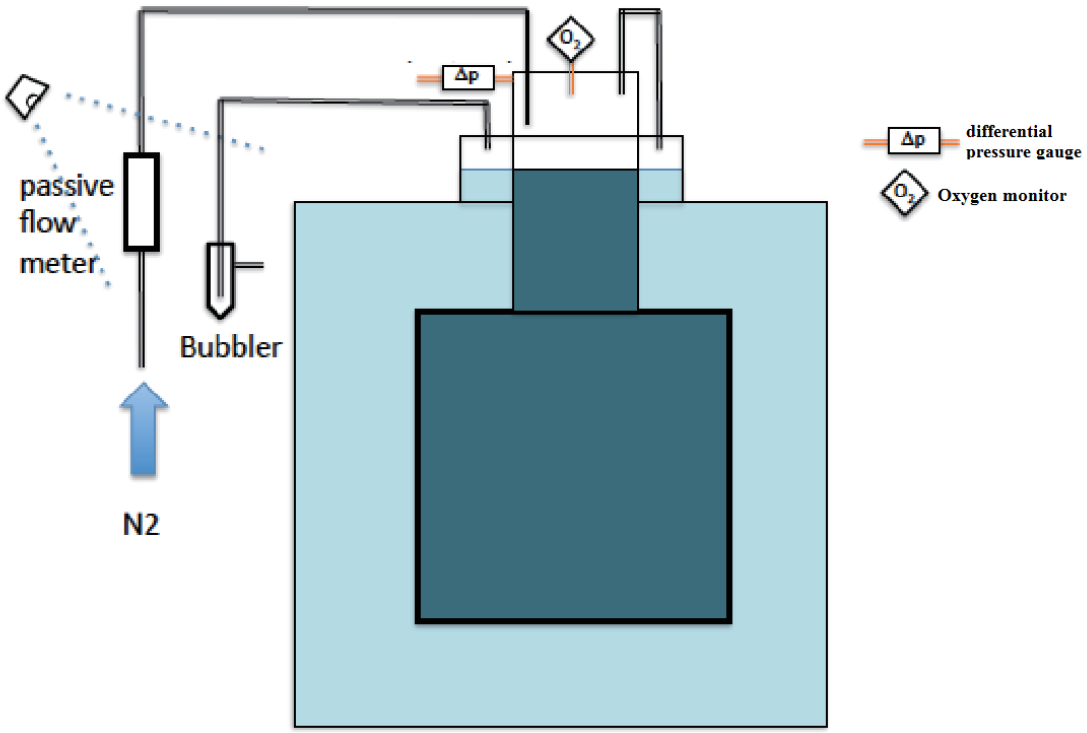


Figure 27: Gas monitors

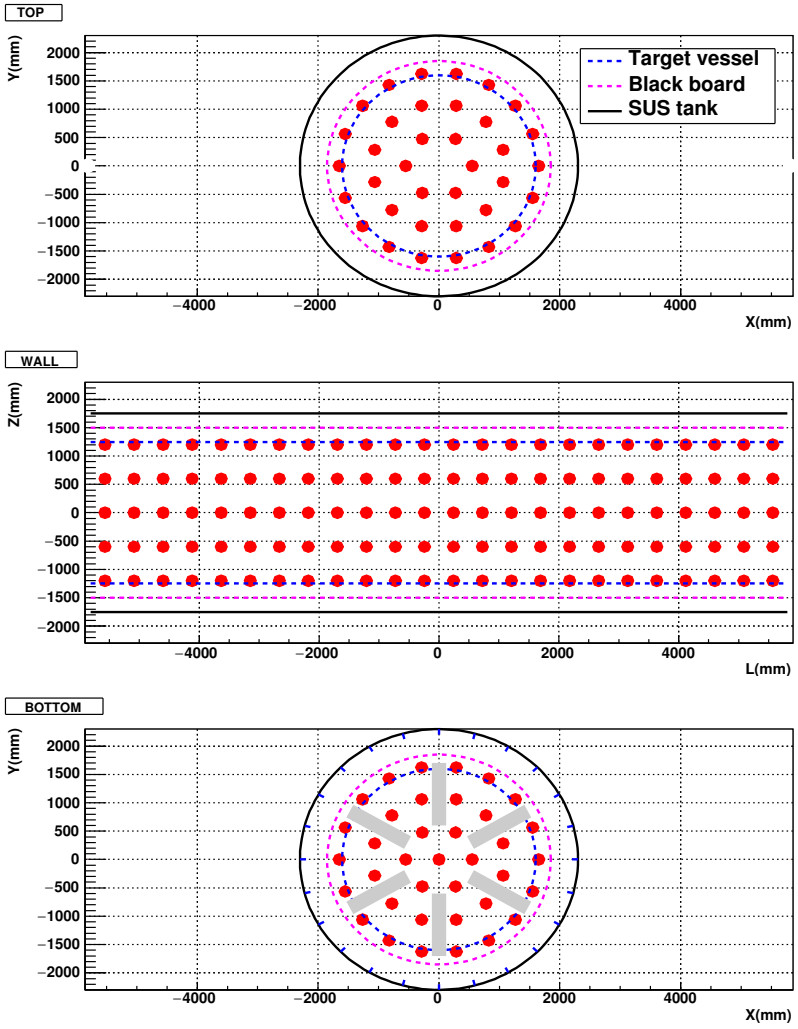


Figure 28: The 8-inch PMT map for the inner volume.

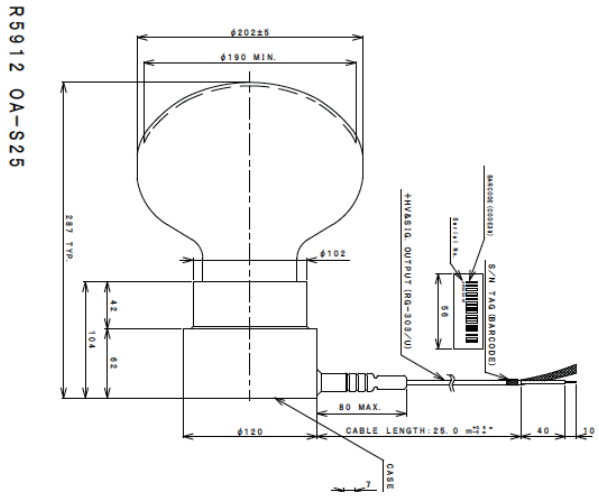


Figure 29: PMT structure

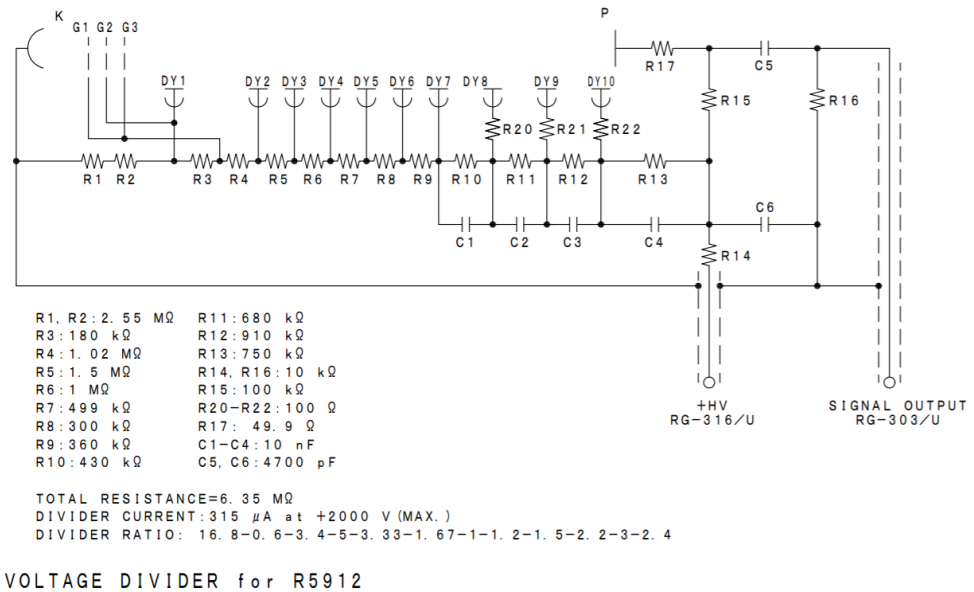


Figure 30: Tapered breeder circuit.

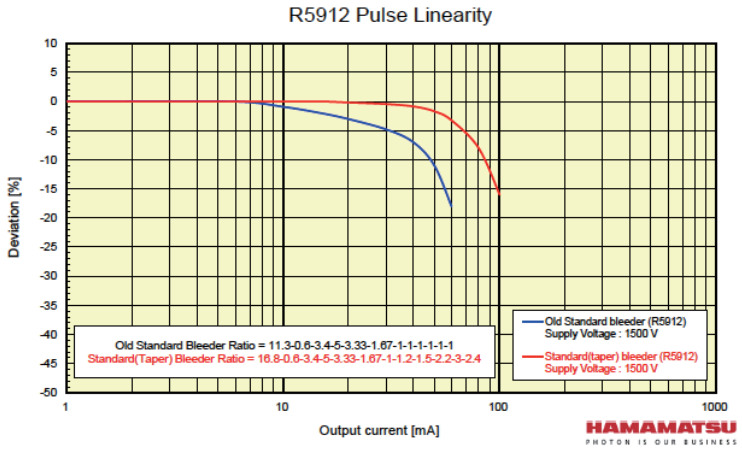


Figure 31: Comparison of dynamic ranges for the tapered base circuit and a normal one.

Testing and HV tuning We propose the following plan for testing the PMTs based on experience with the acceptance tests used for PMT delivery in the Double Chooz experiment [52]. The items included in the acceptance tests are:

i) Measure the gain value as function of the supplied HV in order to find the HV values which give specific gains ($10^6 \sim 10^7$). Compare the results with what is provided by the vendor and define the nominal HV value for each PMT.

ii) Measure the peak to valley ratio. This must be greater than 2.0. Compare the results with what is measured by the vendor.

iii) Measure the transit time spread which should be around 3 ns(FWHM). The average value and the deviation are used as input parameters to MC simulation.

iv) Measure the QE (quantum efficiency) $\times$ CE (collection efficiency) with a light source. The average value and the deviation are used as input parameters to MC simulation.

v) Measure dark counts at threshold (1/4 of the single photoelectron peak) with the nominal HV value.

vi) All PMTs are burned-in for more than 24 hours with the nominal HV. We will require the vendor to perform items i), ii), iii) and v) for all PMTs before delivery in order to compare to our results. During the acceptance test for the Double Chooz experiment, the position dependence of QE $\times$ CE at the PMT surface was measured in order to check the uniformity of the response. Figure 32 shows an example result of the uniformity mapping of QE$\times$CE for a Double Chooz PMT. We require the vendor to perform the QE $\times$ CE uniformity measurement on the PMT surface for $5 \sim 10$ % of all PMTs delivered so that the typical performance of delivered PMTs are obtained because this is an input to the MC.

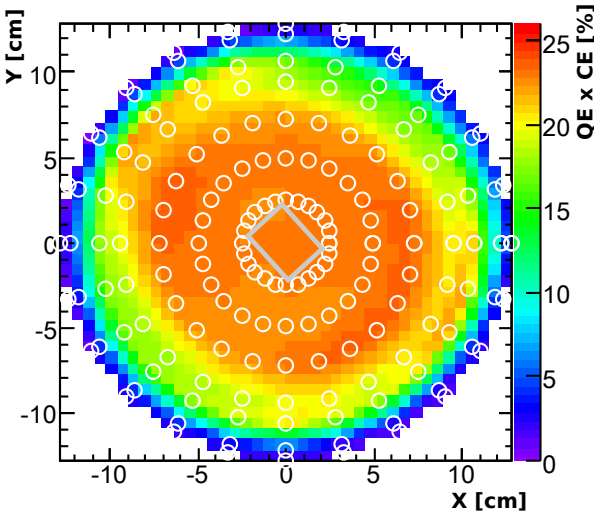


Figure 32: QE×CE map for a typical PMT, which is used for the Double Chooz experiment (Hamamatsu R7081, 10-inch). Although we will employ 8-inch PMTs, they have similar shape and dynode structure. Cable outlet is along the x-axis. The box at the center indicates the first dynode. White circles show the light injection points[52].

Test System For the PMT acceptance test, we plan to re-use the PMT test system developed for the Double Chooz experiment. Figure 33 shows the system. It consists of a black box and cylindrical μ-metals to protect PMT from the geomagnetic field. Some modifications are needed due to the difference of the PMT size.

A pico-second laser ($<$ 60ps width) with a wavelength of 440$\pm$3 nm (Advanced Laser Diode System Co,) is used as a light source since a short pulse and precise timing information are necessary to measure the transit time spread. The intensity of the laser pulse is adjusted with the laser driver box and an ND filter. The light is injected 20 cm away from the PMT surface with the diffuser in order to illuminate whole photocathode.

Test schedule The schedule of PMT delivery strongly depends on the vendor's production capability. The first delivery of 50 PMTs takes 4.5 months after the order is placed. The second delivery with another 50 PMTs takes 1 more month. The delivery rate will increase to 100 PMTs/month at most. In total, the delivery of 200 PMTs will take roughly 6.5 months. The PMTs will be delivered from the vendor to the testing site in a carton box which contains 8 PMTs. As a part of the acceptance test above, we perform the items from i) to iv) for a single PMT and items v) and vi) for eight PMTs at once. Therefore, we can treat 8 PMTs/day at most. Every week, we expect that a few cartons of PMTs will be delivered to the testing site and after testing they will be transported to the assembly site within a week. Therefore, a large space to store the PMTs at the testing site is unnecessary.

Example results by test system Figure 34 shows an example measurement of the charge distribution of an 8-inch PMT (Hamamatsu R5912) using the acceptance test system. The supplied high voltage (HV) is 1700 V, which is the typical value to obtain a gain of 10^7 for the R5912 PMT. The intensity of injected laser pulses for this test

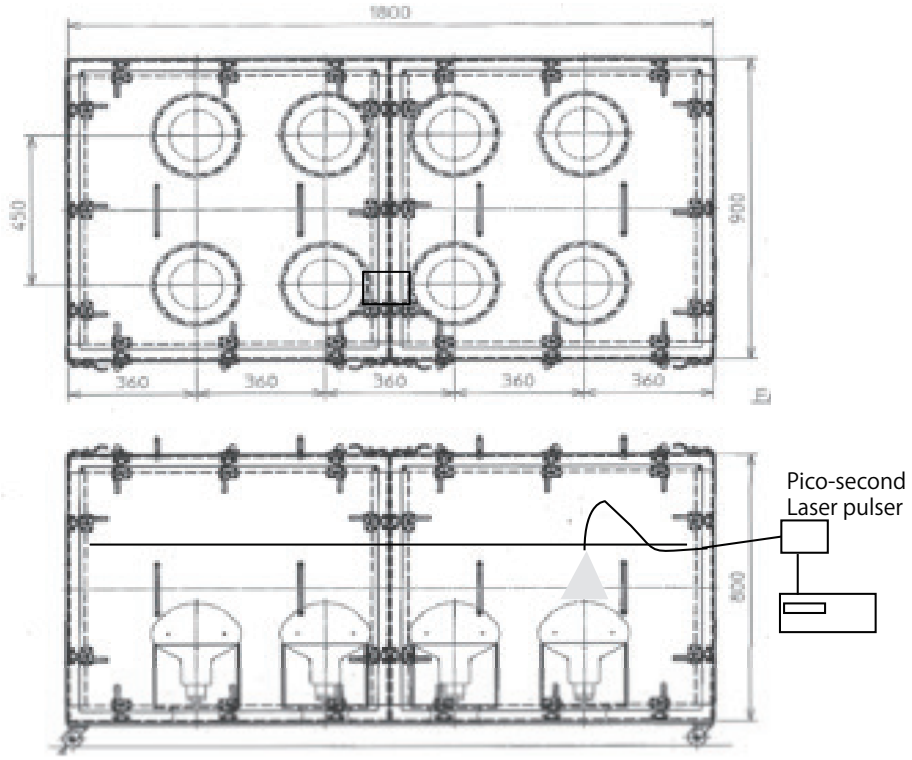


Figure 33: PMT test system, which was originally developed for the Double Chooz PMT test. Eight PMTs can be tested at once. We will perform some modifications due to the difference in PMT sizes. Laser light is used to illuminate each PMT.

corresponds to about 0.2 photoelectrons (PEs). In order to match the dynamic range of the ADC, we used a pre-amplifier with a gain of 10. The 1 PE peak is shown at around 570 ADC count in Fig. 34. The dashed line in Fig. 34 is the fitting function (exponential + Gaussian) for the 1 PE peak. From the fit result, the number of entries at the peak and valley were 862.8 and 425.7, respectively, so the peak-to-valley ratio was measured to be approximately 2.0.

The gain of a given PMT is calculated according to the following equation [52]

$$G = \frac{2 \times ADC_{count} \times G_{ADC}}{G_{Amp} \times e}, \tag{2}$$

where ADC_{count} is the ADC count of the 1 PE peak after subtracting the pedestal count, G_{ADC} is the calibration factor of charge ADC count, $G_{Amp} = 10$ is amplification gain of pre-amplifier, and e is the electron charge. The factor of 2 is a correction factor for the back-termination of the base circuit of our 8-inch PMT. From this expression, we obtained a gain value of approximately 0.8×10^6 with 1700 V.

We can also measure the related transit time (TT) and its spread (TTS) using the same PMT test system. The TDC used for this measurement was started with the trigger signal, which generates laser pulse, and was stopped with the signal created by

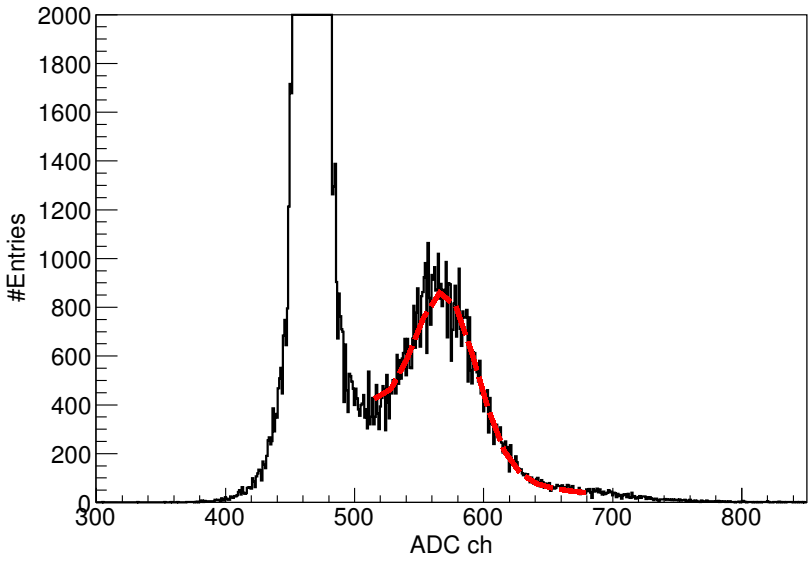


Figure 34: Example charge distribution for a Hamamatsu R5912 PMT measured in the acceptance test system.

discriminating the PMT signal with a threshold level of 0.25 p.e. We briefly evaluated TTS for a sample of 8-inch PMTs, and obtained $\sim$ 1.7 ns, which is consistent with the value $\sim$ 2.0 ns obtained by Hamamatsu.

3.5.4 Noise test at MLF 3rd Floor

We performed a noise test of the 8-inch PMT with a 500 MHz oscilloscope at the MLF 3rd floor while proton beam was on. Positive 1360 V was applied and samples were taken with a 2 mV trigger threshold, as shown in Fig. 35. The standard deviation of the baseline before the PMT signal region was measured to be $\sim$0.2 mV and the average pulse height of a single photoelectron was $\sim$5 mV.

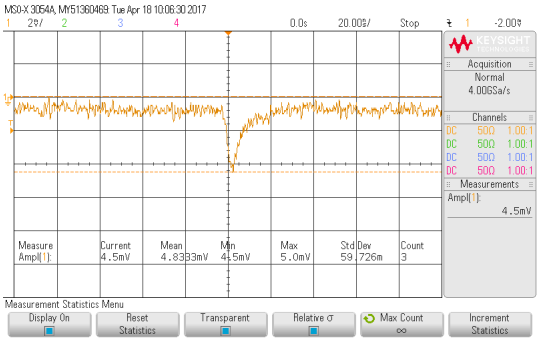


Figure 35: PMT signal in the oscilloscope. The x-axis bin size is 20 ns and the y-axis bin size is 2 mV. The RMS of the baseline is below 1 mV.

3.5.5 Magnetic Shield

The PMT is surrounded by FINEMET[53] which is used as magnetic shielding. The Daya Bay experiment also uses FINEMET for the Hamamatsu R5912 PMT. Figure 36 shows a cross section of the FINEMET magnetic shielding around a PMT and an unfurled FINEMET shield [54]. The slant height of the magnetic shielding is 16 cm.

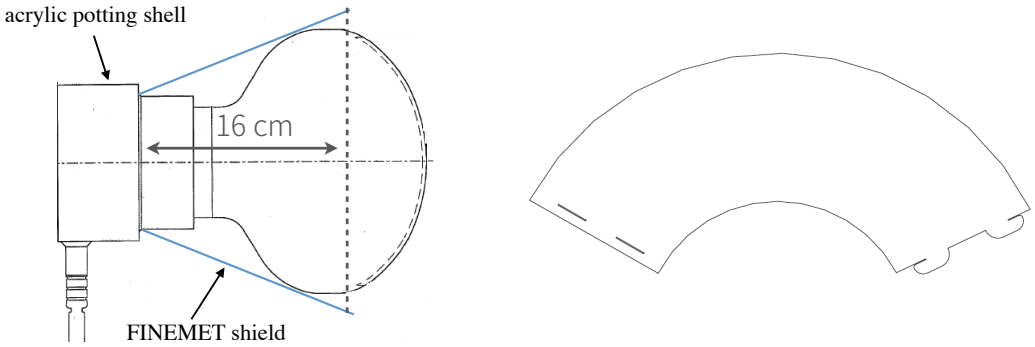


Figure 36: Cross section of the FINEMET magnetic shielding around a PMT (left) and an example shielding piece (right) [54].

3.5.6 Magnetic Field Measurement on the 3rd Floor of the MLF

Each PMT will be surrounded by FINEMET to eliminate interference from the geomagnetic field which will increase PMT performance. The required thickness of FINEMET is proportional to the magnetic filed strength. Therefore, we measured magnetic field strength at the proposed detector position on the 3rd floor of the MLF. We used a Fluxmaster magnetometer, which can measure magnetic fields up to 2000 mG. Three perpendicular direction components were measured at five different points and two different heights (floor level and 1.3 m above the floor). Figure 37 shows the magnetometer and the measurement points along with the definition of the three direction components. Table 8 summarizes the measurement result and shows that the magnetic field strength at the proposed detector position was ∼300-500 mG without FINEMET.

3.6 Veto system

The central target and buffer volumes are surrounded by a veto layer. The veto layer is used to reject charged and neutral particles coming from outside the detector, and to detect energy leakage from the central volumes. The veto layer is 25∼45 cm thick and filled with the same LS filled in the buffer region (LAB-based liquid scintillator without Gd). The inner and outer surfaces of the veto layer are covered by reflective sheets made of REIKO LUIREMIRROR [55]. This material has good reflectance above 380 nm wavelength and for wavelengths longer than 440 nm the reflectance is more than 94 % as shown in Fig. 38.

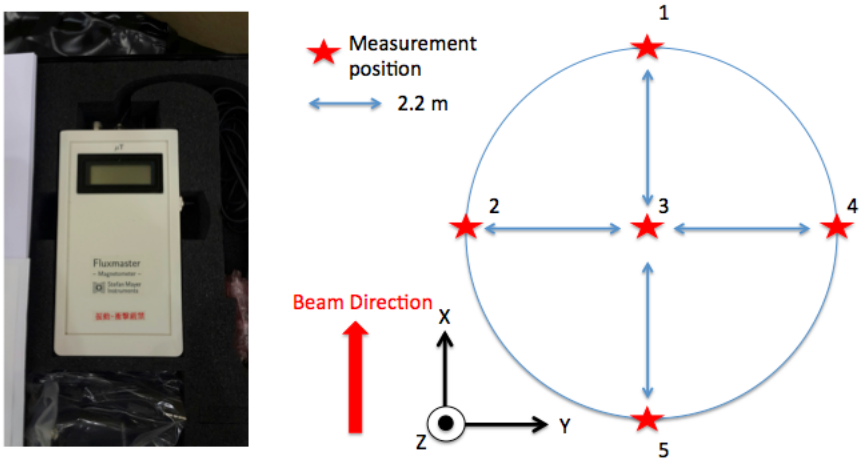


Figure 37: Left : Fluxmaster magnetometer. Right : Magnetic field measurement points at the proposed detector position. We chose five different points and two different heights (floor level, and 1.3 m above the floor), and measured three perpendicular components of the magnetic field at each point.

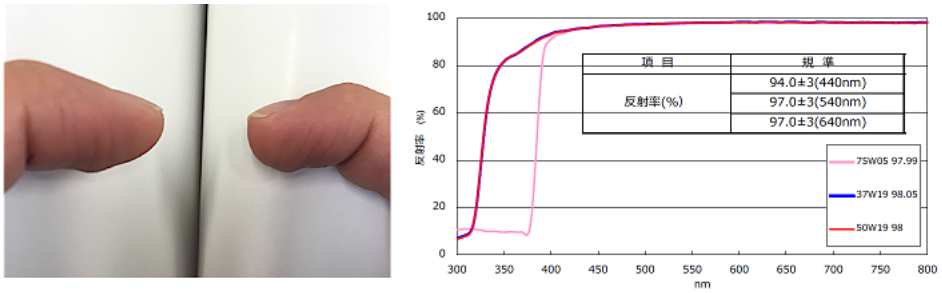


Figure 38: Left: Picture of the LUIREMIRROR reflection sheet, a real finger on the left and its mirror image on the right. Right: Reflectance as a function of wavelength [55].

Scintillation light in the veto layer is converted to the photo-electrons by Hamamatsu R6594 (5") PMTs which are located in the layer (Fig. 39). As shown in Fig. 40, the PMT arrangement has a 12-fold symmetry. Both the top and bottom layers are viewed by 12 PMTs, and the side region is viewed by 12×2 PMTs. This PMT arrangement was chosen because it provides a sufficient light yield, reasonable light uniformity, and reasonable position resolution with a finite number of PMTs and flexibility in the installation.

The expected performance was evaluated with a Geant4 based MC simulation. Here we assumed 90% reflectance for the reflective sheets. 4 GeV/c muons were vertically and uniformly injected into the veto layer and stopped at the surface of the buffer volume placed inside of the veto layer. Fig. 41 shows the expected light yield distribution. The absolute light yield is expected to be more than 25 photoelectron/MeV for all incident positions.

Floor	X (mG)	Y (mG)	Z (mG)	Total (mG)
1	- 309	- 3	- 233	387
2	- 317	- 20	- 186	368
3	- 292	- 22	- 159	333
4	- 336	18	- 140	364
5	- 378	- 5	- 92	389
1.3 m height	X (mG)	Y (mG)	Z (mG)	Total (mG)
1	- 227	15	- 233	326
2	- 291	- 97	- 82	318
3	- 71	- 36	- 465	472
4	- 353	- 24	225	419
5	- 478	10	- 40	480

Table 8: Magnetic field strength measured by the magnetometer. Between ∼300-500 mG was measured at the proposed detector position.

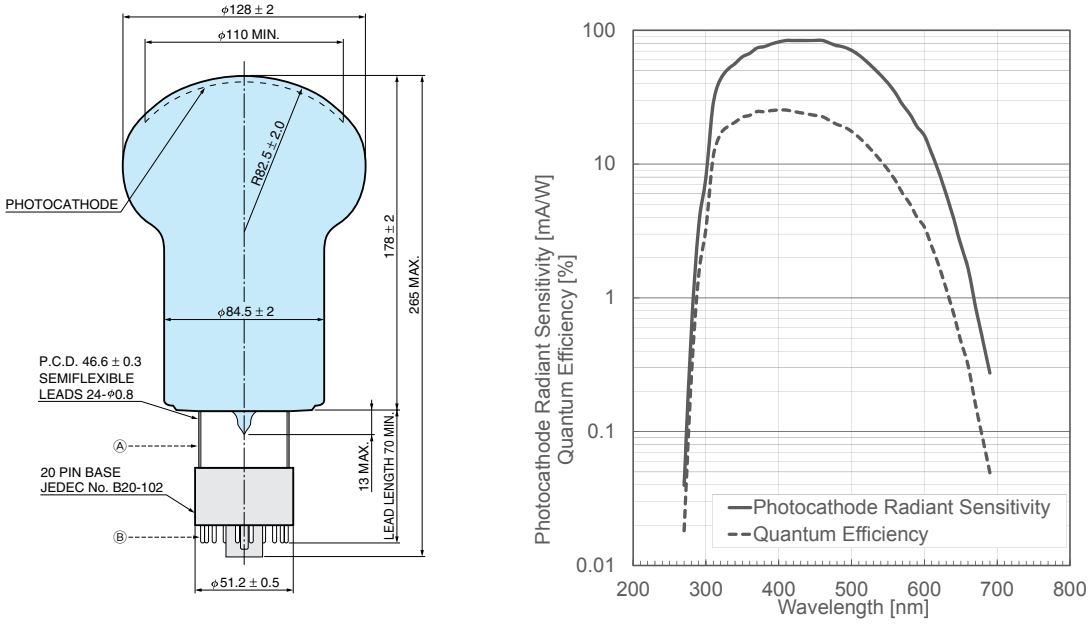


Figure 39: Schematic (left) and performance (right) of the Hamamatsu R6594 PMT [51].

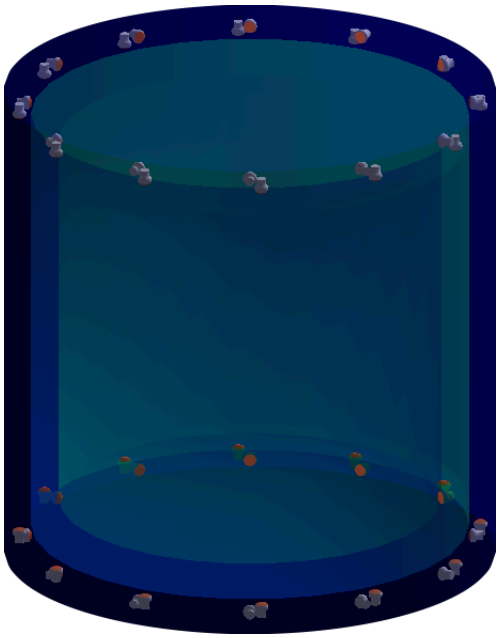


Figure 40: The PMT arrangement in the veto layer.

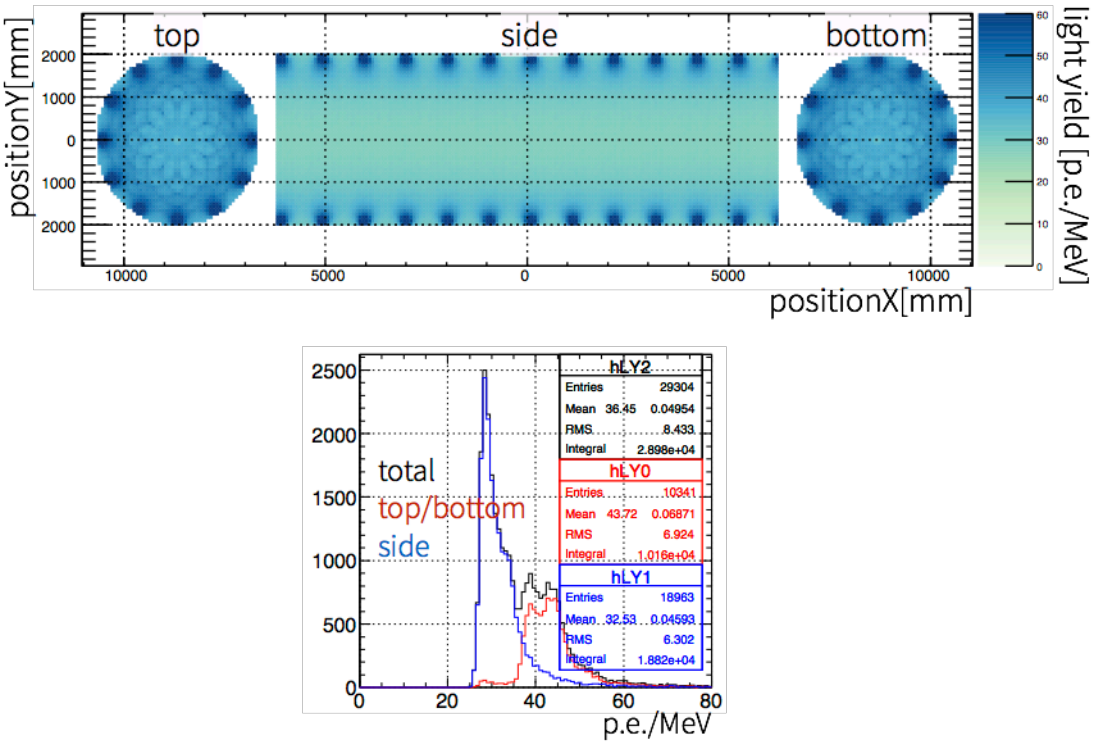


Figure 41: Expected light yields as a function of incident positions (top), and its projection (bottom).

3.7 High Voltage System

We plan to set up the high-voltage (HV) system on or close to the detector in order to reduce the required cable lengths and electrical noise.

The HV system consists of a CAEN-SY527 mainframe (Fig. 42) and A933KP modules (Fig. 43). Three SY527 and 29 A933KP have been donated from the Super-Kamiokande experiment, and were reliably working for over 20 years and it was confirmed at J-PARC that all channels are working. Each mainframe can contain ten A933KP and each A933KP has 24 positive-HV output channels. This system is old one, however, it has worked very well for a long time and we have a lot of reserve modules.

Each SY527 has power-supplies for 10 modules, control system circuits and cooling fans. All channels are controlled and monitored by a front panel console and via an RS232c connection to a PC, which provides a TV100-type emulator. It is also possible to use CAENNET to access the registers one-by-one. Through an internet connection to the PC, we can monitor and control the HV modules from outside the experimental area. It is possible to cut off all of the HV outputs using a front-panel lemo-connector interlock.

The A933KP HV module has one power supply and a 24-ch distributor. The power supply generates HV up to +2550 V and a current limit can be selected from 1 to 13mV. On each distributor channel, the voltage can be reduced by anywhere from 50 V to 900 V with a 0.2 V step. This means we can set the HV values for each channel as high as +2500 V. The maximum current for one channel is fixed as 0.5 mV. Within a given module, the HV values for each channel must be within 850 V of one another which can easily be achieved. The ramp up and down speed are also tunable and can be set anywhere between 10 to 500 V/sec. A block-type female connector (75 pins AMP201311-3 type) is used for HV outputs.

3.8 Liquid Scintillator

There are several requirements for the JSNS^2 liquid scintillator (LS). First of all, it should be an appropriate chemical substance to satisfy the J-PARC fire safety regulation. It should produce sufficient scintillating light for obtaining good energy resolution that is necessary for observing a spectral modulation due to possible oscillation into sterile neutrinos. The liquid needs to be able to differentiate the antineutrino signal from accidental and neutron backgrounds. It should also be stable to maintain the sterile neutrino search for several years.

LS is a mixture of base solvent, primary fluor, and secondary wavelength shifter (if necessary). Linear Alkyl Benzene (LAB, C_nH_{2n+1}-C_6H_5, n = 10 $\sim$ 13) is chosen as the base solvent because it is an environmentally friendly, non-toxic material with a high flash point of 152 °C. It also provides a long attenuation length of >10 m at 430 nm, and produces a large light yield of $\sim$10000 photons per MeV. Isu Chemical Company in South Korea produces high quality LAB and can deliver it in a clean storage container for JSNS^2 at a reasonable price.

The density of LAB is $\sim$0.86 g/L. LAB consists of four main molecules with different number of carbon and hydrogen atoms. These different components can be measured by a gas chromatography mass spectrometer (GC-MS). LAB suffers from non-linear energy



Figure 42: Photo of SY527, CAEN mainframe.

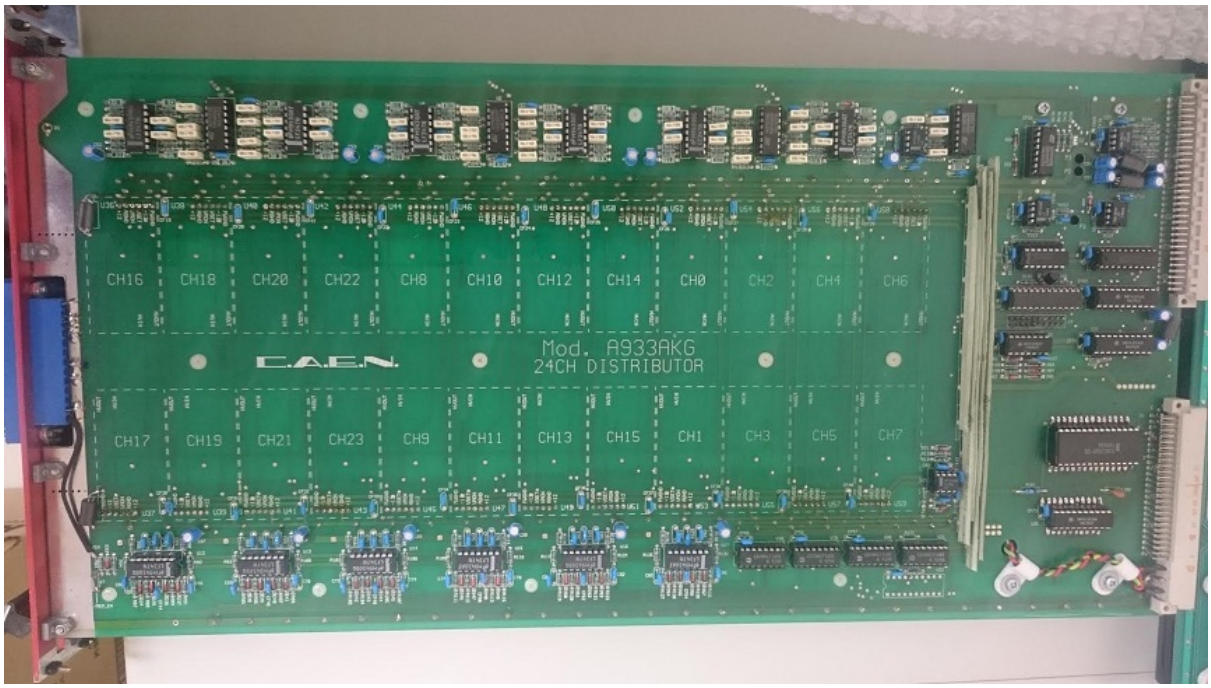


Figure 43: Photo of A933KP, positive HV supply and 24-ch distributor module.

Material	Company	Quantity	Spec
LAB	Isu Chemical Company	54,000 L	-
PPO	Alfa Aesar	162 kg	Scintillation grade
bis-MSB	Alfa Aesar	1.6 kg	Scintillation grade

Table 9: List of chemical elements to be used for JSNS^2 LS.

response due to quenching effects at low energies (i.e. no release of scintillating light even with deposited energy). The RENO experiment has measured the Birk's constant for LAB as ∼0.012 cm/MeV using a Ge detector [57].

3.8.1 Recipe of LS

Because of LAB's emission spectral peak at ∼340 nm, it should be mixed with a wavelength shifter to make the emitted light suitable for PMT detection. We have chosen scintillation-grade PPO (2,5-Diphenyloxazole, $C_{15}H_{11}NO$) for a primary fluor and scintillation-grade bis-MSB (1,4-Bis(2-methylstyryl) benzene, $(CH_3C_6H_4CH{=}CH_2)_2C_6H_4$) for a secondary wavelength shifter, as listed in Table 9. Figure 44 taken from reference [57] shows the emission spectra of LAB, PPO, and bis-MSB. The bis-MSB emission ranges from 390 nm to 500 nm and matches well with the spectral acceptance of the PMTs in JSNS^2. The LS recipe was shown to give satisfactory performance by the RENO and Daya Bay experiments with several years of stability. The JSNS^2 experiment will use LS with 3 g/L of PPO and 30 mg/L of bis-MSB.

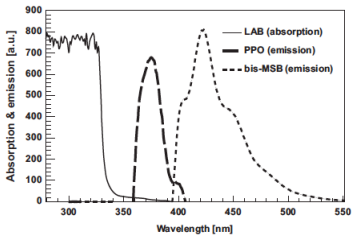


Figure 44: Emission spectra of LAB, PPO, and bis-MSB. The bis-MSB emission spectrum is well-suited for the high-quantum efficiency of the JSNS^2 PMTs.

3.8.2 Purification of LS

We will use a water extraction method and membrane filtering to purify the LS. High quality LAB can be contaminated by dust introduced during delivery, but it can be removed using a membrane filter produced by Meissner. A water extraction method will be applied to remove ^{40}K from the PPO. According to the RENO's measurement[58] the radio-impurity of LS is 13.9 ppt for ^{238}U, 17.7 ppt for ^{232}Th, and less than 0.32 ppt for ^{40}K meaning that additional purification of the LAB is not necessary.

3.8.3 Mass Production of LS

Mass production of the LS is expected to be done using RENO's facility as shown in Fig. 45. A refurbishment including cleaning is necessary to reuse the facility and will take place in the period of late 2017 to early 2018. A new pipeline will be added in order to fill an ISO tank with produced LS. The ISO tank will be used for delivery to J-PARC. Figure 46 shows a schematic diagram of the refurbished mass production system for the JSNS^2 LS. 200 L of 10 times enriched PPO and bis-MSB master solution will be prepared and purified by water extraction using 50 L of ultra-pure water to remove ^{40}K from the PPO. After the water is drained out, the master solution will go through nitrogen purging to eliminate any moisture. The master solution will be mixed with pure LAB to make LS that will be transported into an ISO tank after additional nitrogen purging. The ISO tank will then be delivered to J-PARC to fill the gamma-catcher and veto layers with the LS.



Figure 45: LS production facility to be used for the RENO experiment. This will be used for making the JSNS^2 LS after necessary refurbishment and addition.

3.8.4 Gadolinium-loaded LS

The JSNS^2 experiment will use 17 tons of Gd-loaded LS as a neutrino target. The IBD reaction is utilized to detect antineutrino appearance from sterile neutrino oscillations. A neutron coming from the IBD reaction is captured by either hydrogen (H) or Gadolinium (Gd). While the 2.2 MeV gamma-ray from the neutron capture on H suffers from a large radioactivity background, the ∼8 MeV gamma-rays from the neutron capture on Gd can be well identified to reduce the background events greatly. The mean neutron-capture time on 0.1w% Gd is ∼30 us, more than 6 times shorter than that on H, and can results in significant reduction of accidental backgrounds.

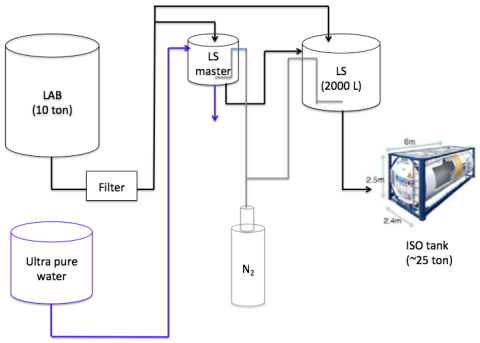


Figure 46: A schematic diagram of the LS mass production system modified from the one that was used for the RENO experiment. This will be used for making the JSNS^2 LS after necessary refurbishment and addition. The LAB will go through a micro-filter of 0.5 μm pore size. The black lines show LAB or LS flow routes, the blue lines show the flow routes of ultra-pure water, and the grey lines show where nitrogen gas will flow.

3.8.5 Synthesis of Gd-LAB

It is necessary to prepare a organometallic complex of Gd using carboxylic acid as an organic ligand. We will make the Gd-carboxylate complex of $Gd(RCOO)_3$ from 3,5,5-trimethylhexaonic acid (TMHA) and Gd powder in the form of $GdCl_3$. The chemical reaction for the synthesis consists of the following steps;

- $RCOOH + NH_3 \cdot H_2O \rightarrow RCOONH_4 + H_2O$
- $3RCOONH_4 + GdCl_3 \rightarrow Gd(RCOO)_3 + 3NH_4Cl$

The first step is a neutralization process of TMHA and ammonium hydroxide. The second step is to make the Gd-carboxylate complex which is formed by mixing an aqueous Gd solution with the neutralized TMHA solution. We will apply a liquid-liquid extraction technique to load the Gd-carboxylate compound into LAB (Gd-LAB). The two solutions will be dropped directly into the LAB under strong stirring. The Gd-LAB yield depends on the solution, dropping speed, and stirring power [57]. The solubility of the organic metal is higher in the organic solvent than in water. Gd-LAB and water can be separated due to the difference in their densities. The separated layer of water can be removed through a drain valve at bottom of the mixing tank.

3.8.6 Mass production of Gd-loaded LS

The mass production of Gd-loaded LS is expected to be done using the RENO facility after necessary refurbishment. Fig. 47 shows the mass production system of Gd-loaded LS consisting of a 10 ton LAB stainless steel tank, a 600 L Gd-LAB acrylic tank, two 20 L acrylic tanks of Gd aqueous solution and TMHA neutralization solution, a 250 L LS master acrylic tank, and a 2000 L Gd-loaded LS acrylic tank.

The LAB from the 10-ton storage tank is purified by a 0.5 μm membrane filter. Gd-loaded LS is produced by mixing Gd-LAB, LS master solution, and pure LAB. Each batch produces 400 L of 0.5w% enriched Gd-LAB to be diluted with LAB. The LS master

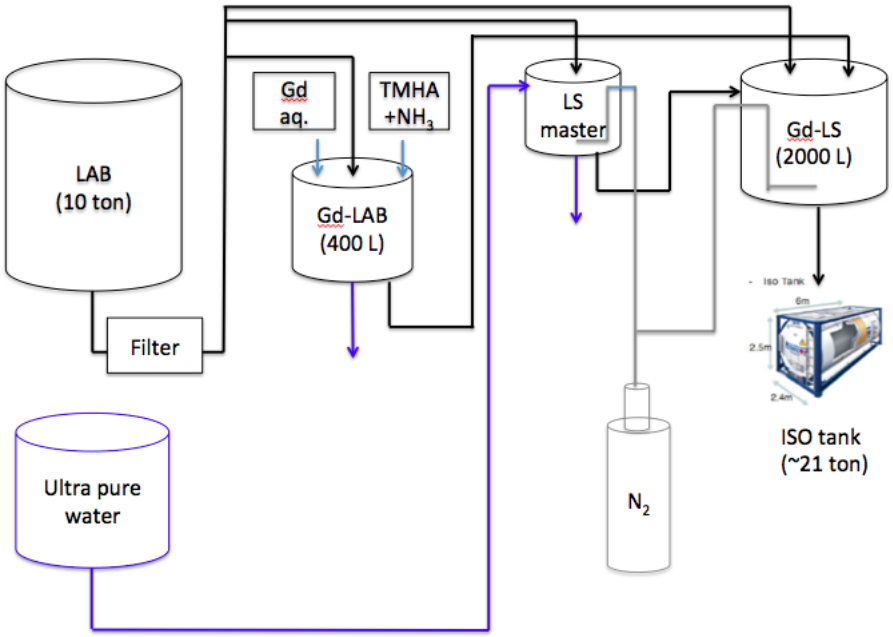


Figure 47: A schematic diagram of Gd-loaded LS mass production system refurbished from the one used for the RENO experiment. The black lines represent flow routes of LAB, master LS, Gd-LAB, and Gd-loaded LS. The Gd-LAB is produced by mixing a Gd aqueous solution and a TMHA neutralization solution that are dropped from the top of the mixing tank.

solution is prepared as described in the earlier section. The Gd-LS mixing tank produces 2000 L of 0.1w% Gd-loaded LS based on 400 L Gd-LAB, 200 L LS master, and 1400 L LAB. Additional nitrogen purging is done to remove any remaining moisture before the Gd-loaded LS is transported into an ISO tank.

3.9 Electronics, DAQ

Flash ADCs (CAEN V1730 [56]) are employed as wave-form digitizers for the PMT signals. We have already made liquid scintillator (LS) performance measurements using a V1730 digitizer [27], and have found its 500-MHz sampling with a 14-bit resolution provide good energy resolution and pulse shape discrimination (PSD) performance. The Double Chooz experiment [52] is also taking data successfully with the older version (V1721, 8-bit resolution). It is expected that the V1730's needed for the experiment will be delivered 3 months after they are ordered.

Table 10 shows the specifications of V1730. Its size is 1U height and 1-unit width of VME with 16-channels of analog inputs. One VME crate can contain all the modules required for a single detector. The FADC has 2 V dynamic range (or 0.5 V selective by software) and 14-bit resolution. The maximum sampling rate is 500 MHz, meaning pulse-height measurements are made every 2 ns. The DC offset can be selected anywhere between ± 1 V, so measurement between 0 V to -2 V is possible. Data buffers are available for each channel and can hold 640 k-samples. The data buffer can be divided into 1024

event buffers for multi-event data-taking, which reduces readout dead time. The record length of the wave form is 1.28 μsec which is enough to utilize PSD techniques, but it can be made shorter in order to limit the data size. A longer record length is also possible, but would require reducing the number of event buffers. A daisy-chain with clock-in/out connectors allows synchronization of the FADC chips on all the modules. The front panel include connectors for many different signals including: trigger-in, reset-in, and busy-out.

The trigger is generated using analog outputs corresponding to the number of hit PMTs (Fig. 48). Each module has one digital-to-analog converter (DAC), which provides an output corresponding to how many channels exceed a preset value on the FADC-chip. These analog signals are fed into an analog sum module then discriminated in order to make logic signals with rough energy information. The signal from the veto PMTs is also built in the same way. This information is used to make a trigger as well as the spill timing signal.

Optical link readout is also possible with these modules and a single link can read up to 8 modules at a time. The average event size is expected to be less than 1 Mb/channel (14 bit, 512 sample) and the number channels to be read is less than 300 ch. Thanks to the larger size of the event buffer (1024 event buffers), data can be readout continuously. Assuming 4 optical-line readout, the data transfer speed from all FADC module to the readout PC is about 320 Mb/sec, therefore 1 k-event/sec is possible. We can add more optical links, if additional performance is required. Collected data are sent to KEKCC for analysis.

Size	VME 6U 1-Unit wide
Sampling	500 MS/s
Resolution	14 bit
Number of channels	16 ch
Dynamic range	0.5 or 2 Vpp
DC adjust	$\pm$1 V
Data buffer size	640 kS/ch
Maximum data transfer speed	80 MB/sec by optical link 200 MB/sec by VME
Power requirement	+5 V, 8.2 A and +12 V 840 mA

Table 10: Specification of CAEN V1730 [56].

3.10 Calibration System

One of the most important calibration sources for the JSNS^2 detector is stopped cosmic ray muons inside the detector because they emit Michel electrons or positrons, which have the same range of the energy as the oscillated signals and dominant backgrounds. They are easily identified using the veto region of the detector, and provide quite useful information.

In addition to the natural source, we plan to use two calibration systems with complementarity purposes. One is an embedded LED system. It calibrates gain and timing

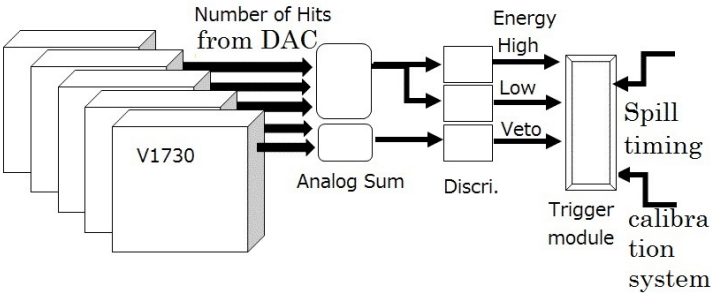


Figure 48: Conceptual design of the trigger circuit. Logic signals of energy information, veto information, beam spill timings and calibration triggers are fed into trigger system in order to make gate signals for the FADCs.

characteristics for the PMTs and other electronics in a short time whenever we want. It can be performed regularly (e.g. weekly or monthly) to check for stable detector performance and to apply corrections when necessary. It is also useful to check the health of the detector during commissioning or after power loss, for example. Low cost and easy installation can be also expected thanks to simple embedded design. The other calibration system we will use is a laser system with better precision. It measures the PMT gains, PMT charge response functions, PMT time offsets, and timing distributions, as well as the effective speed of light, quantities which are essential in determining the performance of the reconstruction and particle identification algorithms. The timing offsets can be determined with better precision using very short laser pulses (FWHM = 50-70 ps), and the charge response functions can be extracted over a wider range due to the dynamic range of the laser output intensity. In addition, the known positions of the laser diffusers in the JSNS^2 detector will provide an in-situ test of the accuracy of the position reconstruction algorithms. Details of those systems are described in following sections.

3.10.1 LED System

The LED system is a conventional system developed and validated by experiments like SNO+ [59] and Double Chooz [60]. The principle of the calibration by a general LED system is as follows. LED light illuminates PMTs in the detector with variable light intensity. Low intensity light give the charge distribution of the PMT at the single photoelectron level. This allows us to calibrate the PMT gain by fitting the distribution with multiple Gaussian functions as found in Fig. 49. According to MC study for the Double Chooz experiment, we can expect $\sim$2% precision in the relative gain calibration. On the other hand, high intensity light allows us to calibrate timing. Different distances between light injection points and PMTs provide a slope of observed times as a function of distance. Using variations in the timing measurements from the fitted slope, we can obtain relative timing offsets for PMTs as found in Fig. 50. In the case of the MC study for the Double Chooz experiment, $\sim$0.3 ns precision of the relative timing offset was expected. As the detector size and structure are similar, we can expect similar calibration precision for the JSNS^2 experiment.

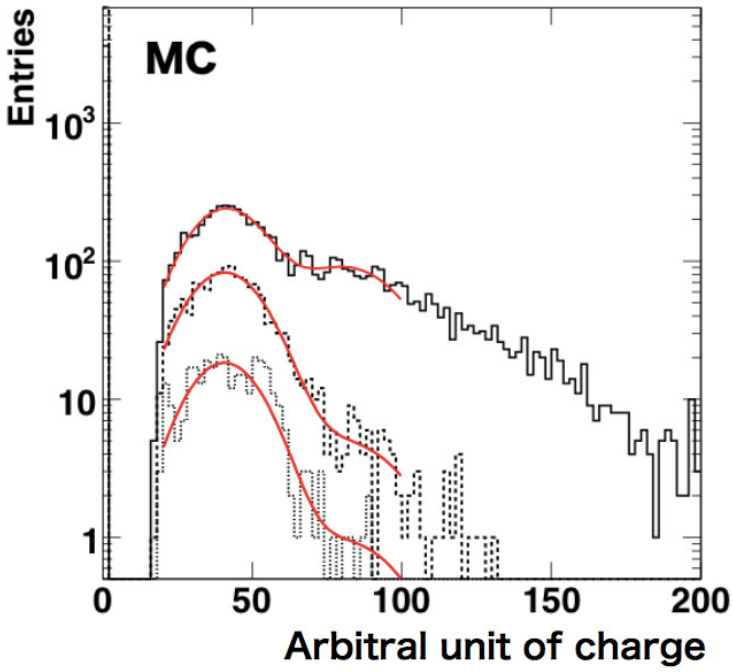


Figure 49: MC study of gain calibration for the Double Chooz experiment [61]. These charge distributions are obtained from FADC waveforms over a certain threshold. Then the pedestal-subtracted distribution is fitted by multiple Gaussian functions using Poisson statistics. The first peak represents the gain used to convert charge to photoelectrons.

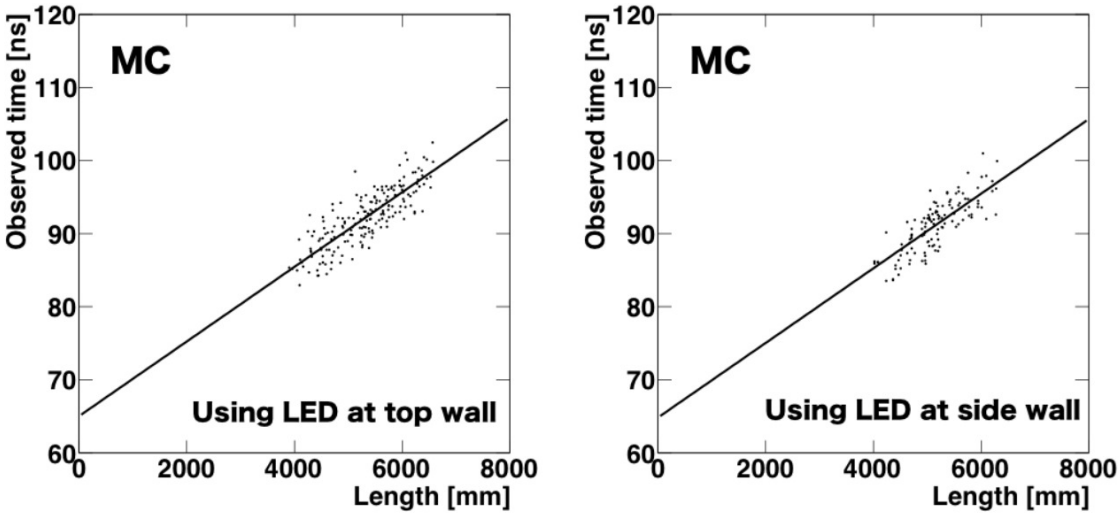


Figure 50: MC study of timing calibration for the Double Chooz experiment [61]. Timing distribution are extracted from FADC waveforms by finding a peak in the pulse shape. Then mean timing values for various positions of PMTs are plotted. The different TOF for each PMT gives the overall slope, and the variation of an individual PMT from this slop gives the appropriate timing correction.

We will employ a "nanopulser system" developed by Sussex University shown in Fig. 51. One difference between this system and conventional LED systems is the use of direct LED light in the detector without an optical fiber. This gives us the capability to provide higher light intensity and no bias on the timing properties as function of LED emission angle. Therefore, better calibration accuracy is expected than the traditional technique. Furthermore, the device is suitable for the JSNS^2 detector because optical fibers are not compatible with LAB. In the case of a conventional system, the LED is located outside detector and an optical fiber is used to guide LED light into the detector. The Nanopulser system, on the other hand, can embed an LED with small driver board in the detector. The LED and drive board are encapsulated in a material compatible container made of acrylic. The specifications of the Nanopulser system are summarized in Table 11.

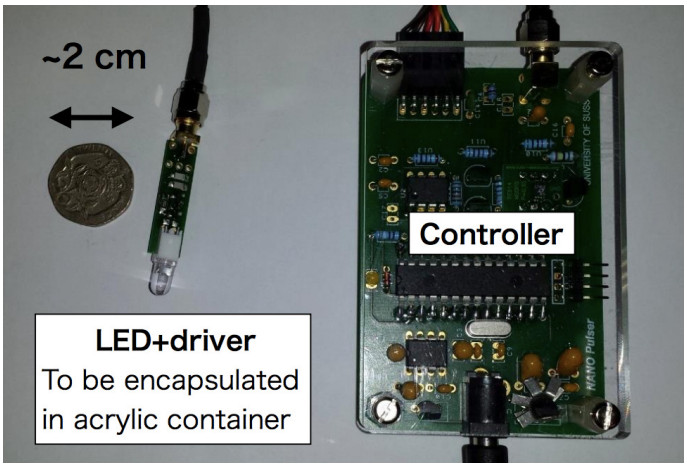


Figure 51: A picture of Nanopulser prototype. The left board has an LED and its driver and to be mounted in the detector after being encapsulated in an acrylic container. A twenty pence coin is placed as a size reference. The right board is a controller for the system and connects to the LED with an electrical cable.

Item	Performances
Wavelength	355 and 420 nm
Timing profile of light pulse	355 nm: 0.40 nsec (rise), 0.75 nsec (fall), 0.79 nsec (width)
	420 nm: 0.40 nsec (rise), 0.63 nsec (fall), 0.65 nsec (width)
Opening angle of LED light	355 nm: 30.2 $\pm$ 3.5 degree
	420 nm: 26.9 $\pm$ 1.8 degree
Light intensity	Capability to provide single to thousands of photoelectrons
Flushing rate	Up to 100 kHz
Trigger	Capability to produce/accept a TTL trigger

Table 11: Major specification of the Nanopulser system

A schematic drawing of the system with multiple channels in the detector is shown in Fig. 52. The LED and driver boards are encapsulated in an acrylic container and mounted in the support structure. A single electric cable from the board is placed along

the support and taken from the inner detector. It is connected to the controller, which provides a trigger to the DAQ and receives a command through an easy interface with python. The light intensity and flushing rate can be controlled within the specifications of the system.

To achieve full coverage for gain and timing calibration, 12 LEDs with 420 nm wavelength are located in the detector; 2 positions at the top and bottom of the detector, and 4 positions for 2 rings on the side wall. In addition 2 LEDs are mounted with 355 nm for possible calibration of the attenuation length of the liquid scintillator and angular dependences of the PMT response. Therefore, a total 14 LEDs will be mounted with two different wavelengths.

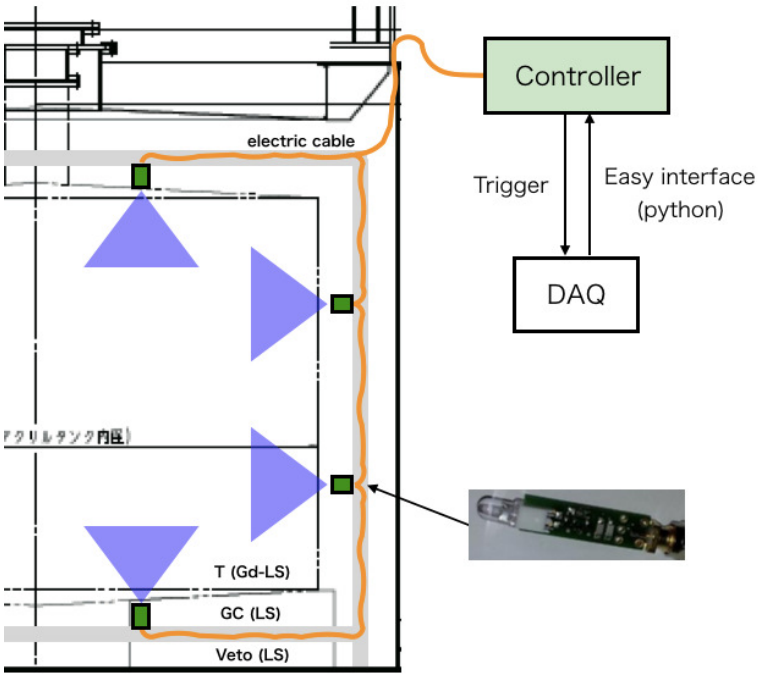


Figure 52: Schematic drawing of the Nanopulser system with multiple channels in the detector.

3.10.2 Laser System

The system consists of a short-pulsed PicoQuant PDL-800B laser driver and two laser heads, LDH-P-C-375B and LDH-P-C-470 of wavelengths 375 and 470 nm, respectively. The system can be operated with a repetition rate up to 40 MHz, which is well above the rate envisaged for the experiment. Typical calibration runs are expected to be taken at rates of $\mathcal{O}(100)$ Hz, which means that reasonably high statistics can be achieved in a relatively short time. The system can be driven by either an external pulser or internal trigger, and will deliver a reference timing signal and trigger bit to the JSNS^2 DAQ. The intensity of the laser light can be adjusted through the PDL-800B driver and through additional neutral density attenuation filters.

The UV laser light is used to extract the PMT gains – when operated at very low

intensities, as well as the charge and time likelihoods – when operated over a large range of intensities. The charge likelihoods, $\mathcal{L}_q(q;\mu)$, characterize the probability for any given PMT to measure a charge q for a predicted charge μ, while the time likelihoods, $\mathcal{L}_t(t;t^{pred},\mu)$, characterize the probability to measure a time t for a predicted time t^{pred} and charge μ. The UV laser light is delivered to a diffuser through a multi-mode optical fibre, as additional widening of the original pulse is irrelevant compared to the long time constants of the scintillator. The $\Lambda = 470\,\text{nm}$ laser light does not excite the scintillator, and therefore is ideally suited to extract the PMT time offsets. This light has to be delivered to a different diffuser through a single-mode optical fiber, in order to preserve the short-pulsed characteristics of the laser driver. In Double Chooz such a system was shown to be able to measure the time offsets with a precision of about 0.1 ns.

Although light isotropy is not a requirement for the laser light diffusers, their design will attempt to maximize the isotropy and the diffusers will be fully characterized before installation. A known diffuser light output profile will allow additional quantities to be extracted, such as optical medium or PMT characteristics (e.g., effective attenuation length, relative quantum efficiencies, etc.).

3.11 Installation works inside Tank

In this subsection, the procedure for the installation of the PMTs, optical separators between different detector regions, reflection sheets, and FINEMET magnetic shields is described.

First, each PMT is covered by a thin black PET sheet under the FINEMET sheet to establish light separation between the inner and veto volumes, and to prevent light noise in the base circuit of the PMT as shown in Fig. 54. Furthermore, the PMT support structure shown in Fig. 54 is attached to each PMT.

In parallel to the installation of the optical separators for each of the PMTs, stainless L-type angle bars to fix the PMTs are welded to the stainless tank (Fig. 53), and the inner surface of the stainless tank is covered by reflective sheets made from REIKO LUIREMIRROR (see veto sections). To fix the sheets, welded L-type angle bars are placed in advance.

Next, the PMTs are attached to the stainless tank wall. The PMT support structure is attached to a box unit assembled with stainless L-type angle bars (40 mm width) including the welded bars. Then, a total of five PMTs are attached to the box unit as shown in the left image of Fig. 54. Black acrylic boards are attached to the box unit for further light separation from the veto region. A total of 24 box units are attached along the stainless tank wall. The right image in Fig. 54 shows an overview inside the stainless tank after the installation of the box units. After the box units are in place, the PMT cables are fixed with cable ties along the welded angle bars on the wall.

Six acrylic bases (supports) are installed on the bottom part of the stainless tank as shown in Fig. 55. After that, the PMTs and the blackboards in the bottom part of the detector are installed using stainless L-type angle bars (30 mm width) welded on the bottom part of the stainless tank. Figure 56 shows an overview of the inside of the stainless tank after the installation of the acrylic supports and the bottom PMTs.

While the PMT installation on the walls and bottom part of the detector is performed, the PMTs and the black acrylic boards for the top part are attached to the stainless tank

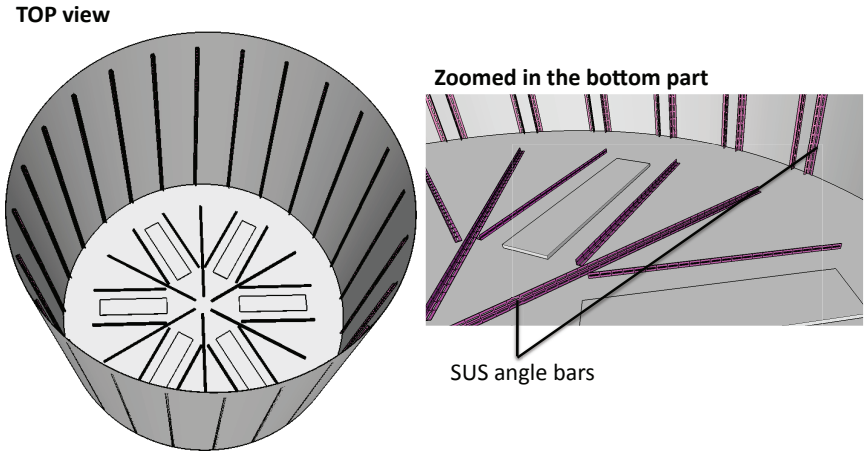


Figure 53: Inside of the stainless tank before the PMT installation. The left figure shows the top view, and right figure shows a zoomed-in view of the bottom part.

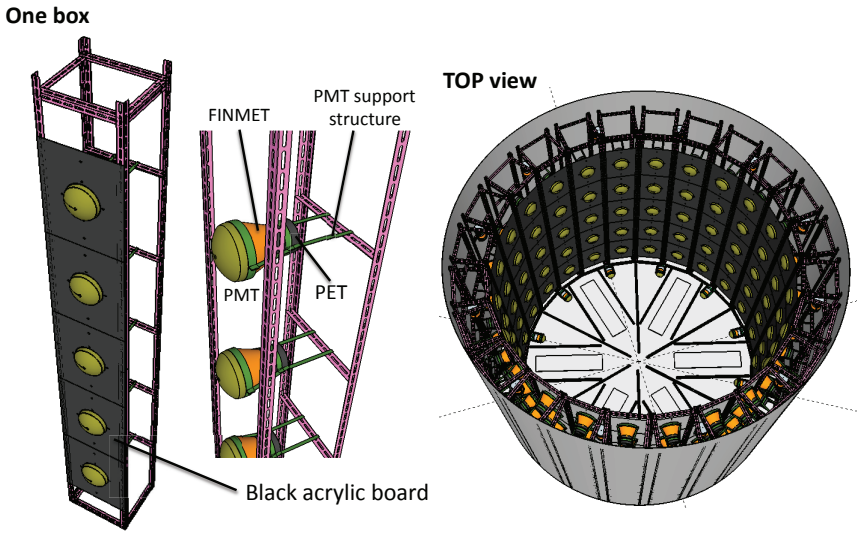


Figure 54: Wall PMT installation. The left figure shows one unit of wall PMT support structure. The right figure shows the inside of the stainless tank after the installation of the box units on the walls.

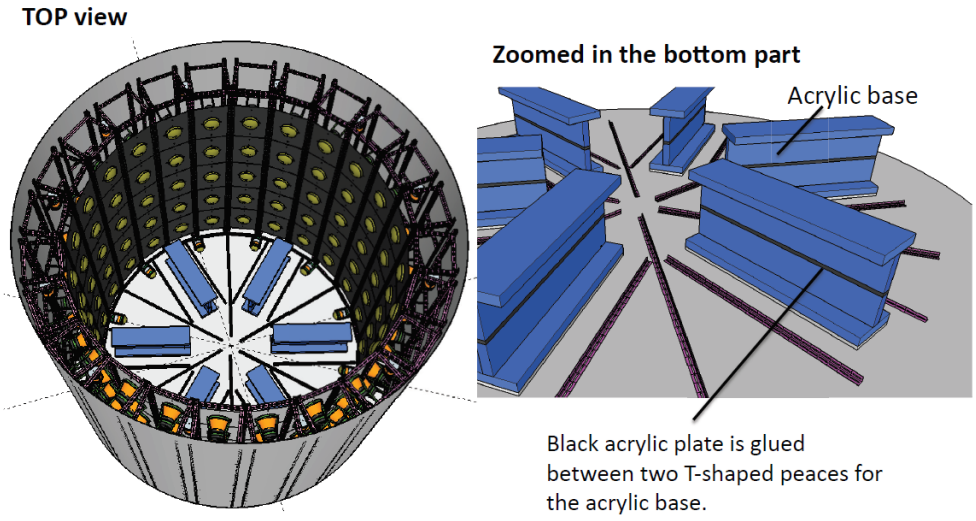


Figure 55: Installation of the acrylic base. The left figure shows a top view and the right figure shows a zoomed-in view of the bottom part of the detector.

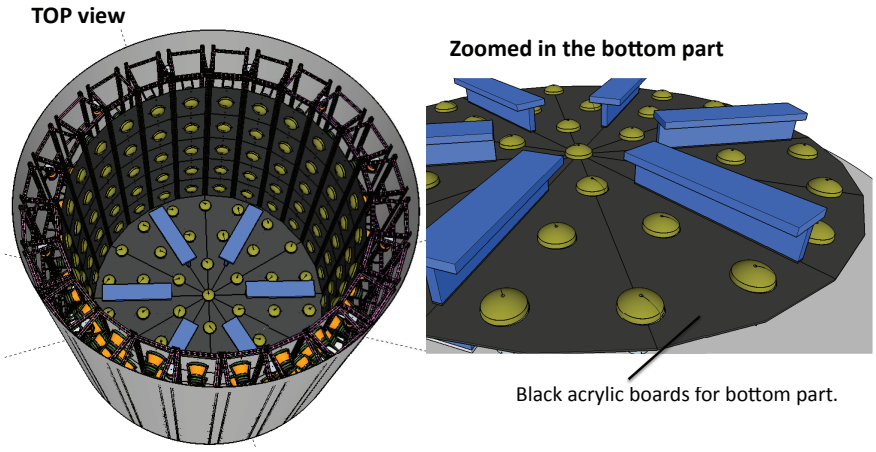


Figure 56: Installation of the bottom PMTs and optical separators. The left figure shows a top view and right figure shows a zoomed-in view of the bottom part of the detector.

lid using the same method as the bottom part. The installation of the PMTs and the optical separators in the stainless steel tank lid are done in parallel to the other installation work. Figure 57 shows the lid part after attaching the PMTs and the black acrylic boards.

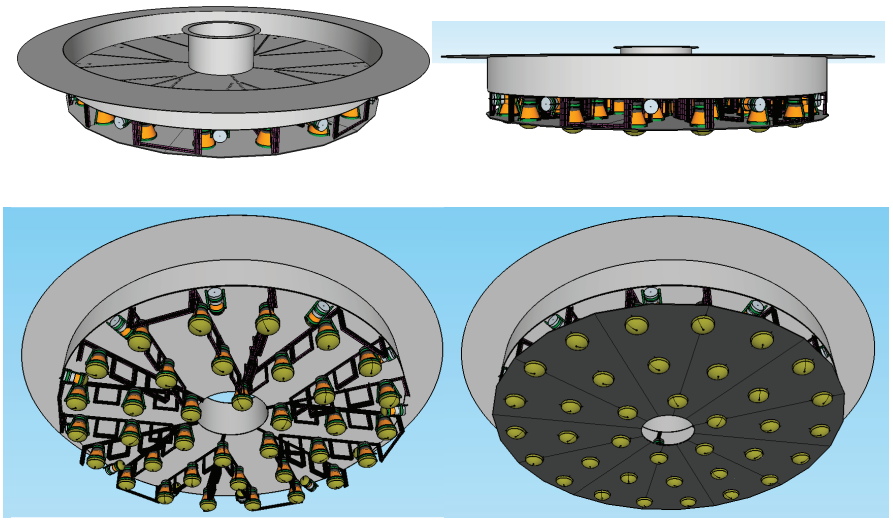


Figure 57: The stainless tank lid after attaching PMTs and black boards. The upper left and right figures show the top and side views, respectively. The lower left figure shows the bottom of the lid after attaching the PMTs and the stainless L-type angle bars, and the right figure shows the bottom after covering the lid with black acrylic boards.

After the installation of the wall and bottom PMTs, the acrylic target vessel is lifted down by the crane and is fixed to the acrylic bases with screws. Finally, the lid is placed on the stainless tank. (Fig. 58).

3.12 Expected Experimental Operation

3.12.1 Normal Operation

The expected detector operation through a given year is illustrated in Fig. 59. The following are the phases of operation for the detector:

- In October, we fill the detector with LS at the entrance of the MLF using ISO tanks (used to store the LS). The ISO tanks, pumps and pipes are prepared by experimental group.

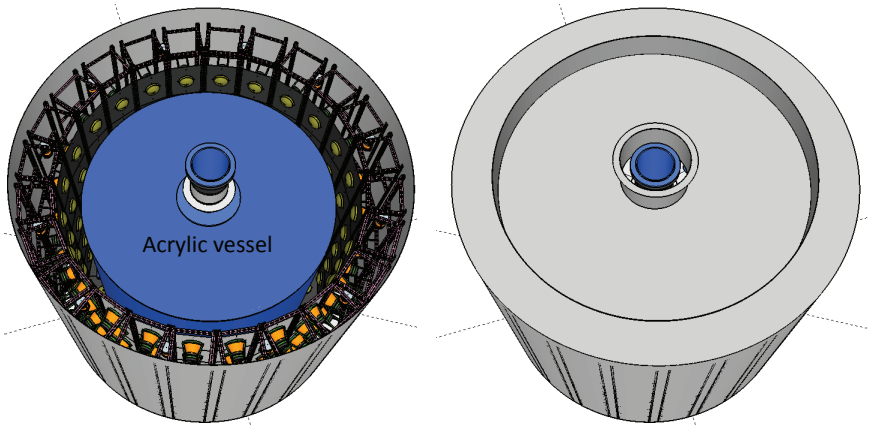


Figure 58: Inside of the stainless tank after the acrylic vessel is inserted (left), and after the lid is on (right).

- After filling, the detector will be moved from the entrance to the 3rd floor ("Large Component Handling Room") using a 130-ton crane.
- Physics data is taken from October until the following June. (5000 total hours)
- In June, the detector is moved from the MLF 3rd floor to the MLF entrance area again. The LS is extracted from the detector and put into the ISO tanks.
- The ISO tanks are stored in Kasawaki by a privae company. They can regularly inject cool nitrogen gas into the detector to preserve the integrity of the scintillator and have experience with this procedure.
- The weight of the empty detector is small (∼20 tons) and the Fire Law is not applicable after the extraction of the LS, therefore the detector can be stored in a normal area (i.e.an area not registered under the Fire Law). We plan to put the detector in the HENDEL building at J-PARC during that period (no beam).

We have already contacted two companies to arrange purchase of ISO tanks, and the procedure above has been verified to be realistic.

ISO Tank and Filling/Extracting System

An ISO tank is a safe container made based on an international standard (ISO standard). Because ISO tanks satisfy international shipping standards, it is possible to ship

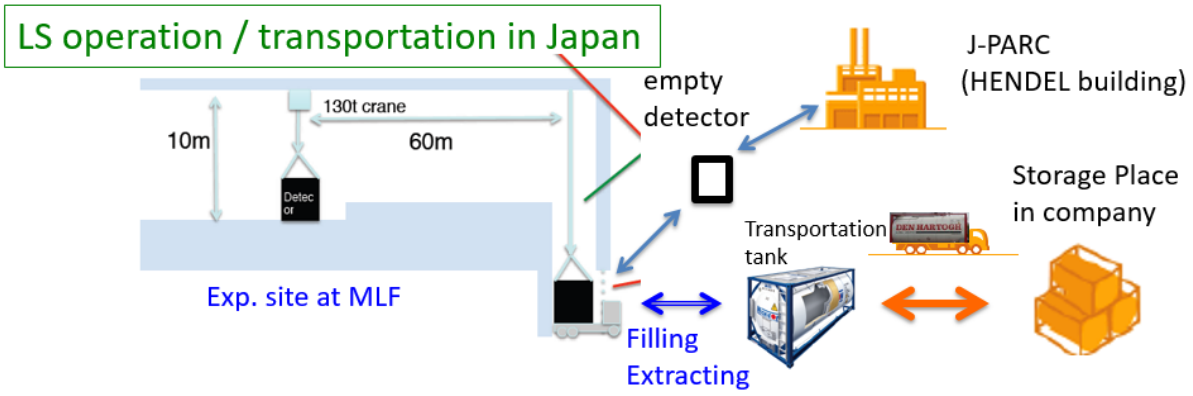


Figure 59: The detector and LS operation during the experiment through a given year. Details are given in the main text.

them not only in Japan, but also overseas. Since each ISO tank is equipped with the relevant parts for filling, extracting, and maintaining the liquid, the LS can be safely handled. The ISO tank has satisfactory performance as a dangerous goods container, and thus can be used as a transportation container and as a storage container for the LS with out concerns over degraded quality.

The ISO tank has a capacity of about 25,000 L, though other smaller sizes exist as well. When transporting ISO tanks, it is required that the tank only be filled to between 80 to 95 % of the total volume. In the JSNS^2 detector, the volume of Gd-LS is about 19,300 L, and the volume of the standard LS is 35,000 L, so it is possible to store all the liquid in a total of 3 tanks. ISO tanks have heat insulation to cover the inner tank part of stainless steel, and the exterior is covered in FRP. This structure reduces heat intrusion. A metal frame surrounds the container and makes loading the tank easier. Figure 60 shows construction and size of an ISO tank.

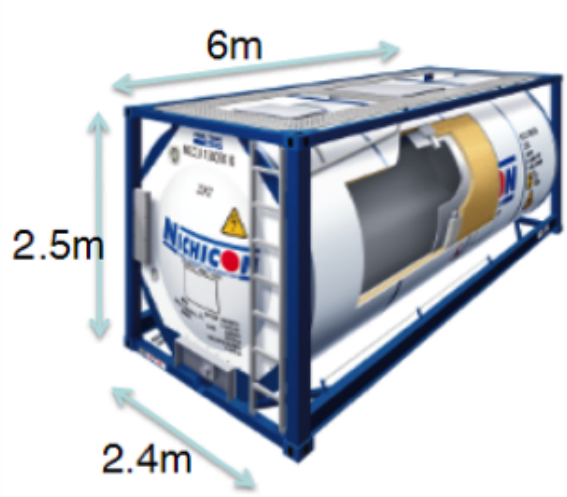


Figure 60: Cut model of an ISO tank with the dimensions labeled. Figure is reprinted from http://n-concept.co.jp/service/tank/

Any metal contact with Gd-LS could accelerate the aging effect of the Gd-LS, re-

sulting in diminished performance. We decided to teflon coat the inside of ISO tank and outlet valve that will be used for storage of the Gd-LS. Two standard stainless-steel ISO tanks will be used to store the veto LS.

We need to consider several things in designing the liquid handling system. First of all, filling and extracting should be done within a few days because if an emergency happens, the detector must be moved to HENDEL within one week. In addition, the flow path of Gd-LS should be made with non-metallic materials. 1 inch teflon pipe will be used to construct the liquid handling system. Because filling and extracting will be done around the equipment entrance of MLF building, 1 inch teflon pipe will be wrapped with black sheet to reduce exposure to sunshine. We will use a MEGA 960 pump from TREBOR, which is pneumatically driven with 95 LPM of max flow rate and whole flow path is coated with either PFA or PTFE. The max suction lift is 5.5 m, which is larger than height of the JSNS^2 detector. Even if the quality of the Gd-LS and the LS is good enough, contamination can occur with dust particles while filling or extracting. We will install a 0.1 μm pore size membrane filter made by Meissner before the detector while filling and before the ISO tank while extracting. A flow meter will be used to check the accumulated amount of liquid and to control the spontaneous flow rate to prevent a difference of liquid level at target, gamma-catcher, and veto layers. Figure 61 shows a schematic design of the handling system for the filling case.

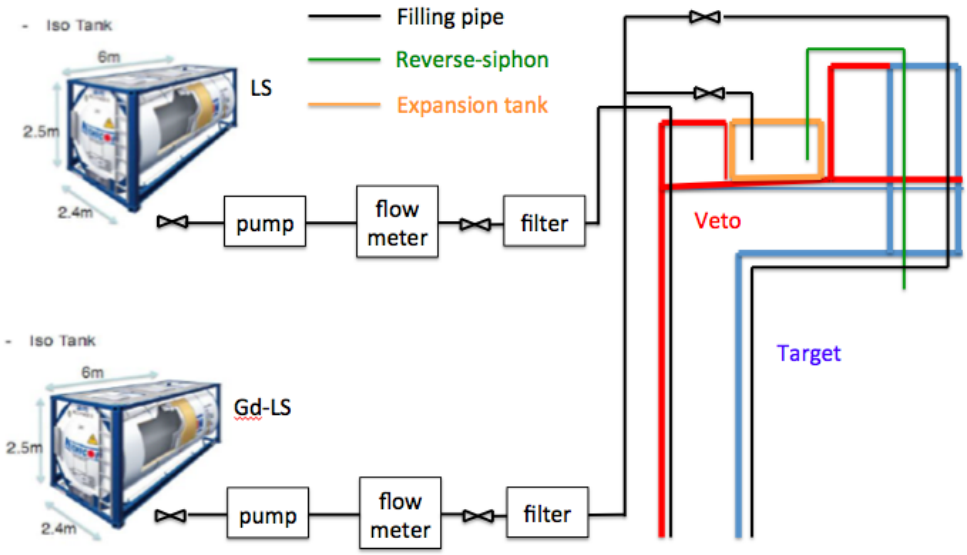


Figure 61: Schematic diagram of the liquid handling system while filling. The thick blue line is acrylic vessel, the thick red line is stainless-steel tank. The green line shows the revrese-siphon system, and the black line is the installed filling pipe. At the target, there are two filling pipes to help protect the fragile chimney region.

Filling and extracting will be performed according to six stages. These stages are important to ensuring that the liquid level in the different detector layers is kept the same. Figure 62 shows each stage for safely filling / extracting and Table 12 summarizes detailed information on each stage. The max flow rate is assumed to be 30 LPM in reality because of resistance in the liquid handling system. Extracting will be performed in reverse order.

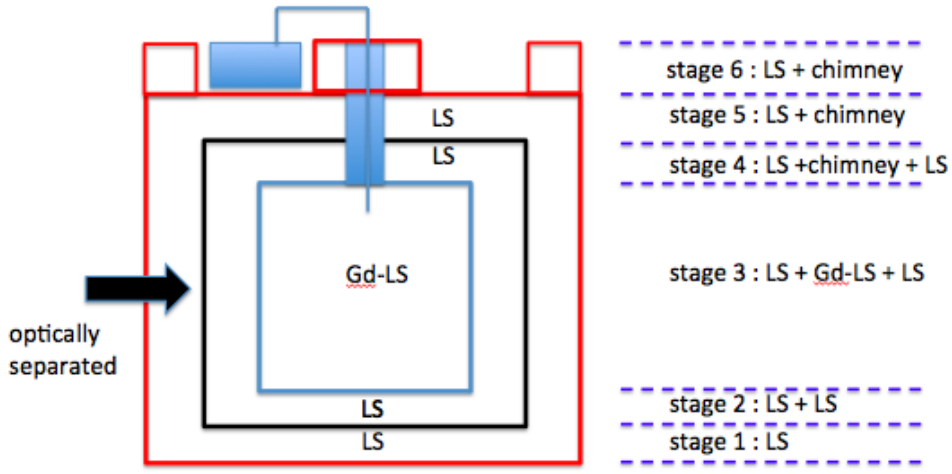


Figure 62: Definition of each stage for safely filling and extracting.

	Target [LPM]	Catcher+Veto [LPM]	Height [cm]	Target [L]	Catcher+Veto [L]	Time [h]
stage 6	0.1	1	12	4 + expansion	expansion	few
stage 5	0.1	30	25	8	4000	2.2
stage 4	0.1	30	25	8	4000	2.2
stage 3	30	29.5	250	19350	19000	10.8
stage 2	0	30	25	0	4000	2.2
stage 1	0	30	25	0	4000	2.2
Total				19370	35000	19.6

Table 12: Flow rate, height, volume, and expected time of each stage.

Because the chimney is much narrower than the detector vessel, a small difference in the amount of liquid between the target and veto layers can generate a liquid height difference of more than 15 cm, especially at target chimney. We will install two filling pipes for the target to avoid such a situation. Near the target chimney, the valve of the detector filling pipe will be closed and valve of expansion tank filling pipe will be opened. Then, the Gd-LS expansion tank will be moved automatically to target chimney through reverse-siphon system. In the veto case, the detector itself contains a donut-shaped, region which prevents liquid level changes in response to thermal variations (i.e. we do not need to change filling method at the chimney part for the veto). Extraction will be performed in reverse order.

3.12.2 Operation in the Emergency

If the MLF faces an emergency, the JSNS^2 detector should be removed from the MLF building as soon as possible. We expect that the detector can be moved within a few days to ∼1 week using the 130-ton crane. The MLF usually needs more than a week

to exchange the target so that the target area can become radiation cool. Therefore no interference in the case of an emergency is expected.

In the case of a detector emergency such as an LS leak, all of the liquid will be contained in the first and second oil-leak tanks. On the off chance that LS gets onto the floor of the MLF, it is not possible for the LS to get into the target area due to the sealant and oil leak barriers. In this case, the LS will be removed from the floor immediately.

3.13 Offline Software

3.13.1 Event Reconstruction and Particle Identification

The event reconstruction developed for JSNS^2 is based on a maximum likelihood algorithm that makes use of all information available in any given event. An event is fully characterized by the four-vertex (x, y, z, t) in the coordinate system of the detector, direction (ϕ, θ), and energy (E). Thus, for any given event defined by the set of parameters $\vec{\alpha}$,

$$\vec{\alpha} = (x, y, z, t, \phi, \theta, E),$$

the likelihood for measuring a set of PMT charges (q_i) and times (t_i) in the JSNS^2 detector is the product over the individual charge and time likelihoods at the PMTs:

$$\mathcal{L}_{event} = \prod_{i=1}^{N_{pmts}} \mathcal{L}_q(q_i; \vec{\alpha}) \mathcal{L}_t(t_i; \vec{\alpha}).$$

Reversing the meaning of the likelihood function, $\mathcal{L}_{event}$ is the likelihood that the event is characterized by the set $\vec{\alpha}$ given the set of measured charges (q_i) and times (t_i). Maximizing the event likelihood $\mathcal{L}_{event}$ (or equivalently minimizing $-\ln \mathcal{L}_{event}$) with respect to $\vec{\alpha}$ determines the optimal set of event parameters.

Given the neutrino energies and detector size in JSNS^2, all events can be assumed to be point-like. Neutron/proton events can be well approximated to produce only isotropic scintillation light, where the flux Φ (photons per steradian) is proportional to the event energy E. The average number of photoelectrons (PEs), μ_i, expected at a PMT of quantum efficiency ε_i, at a distance r_i from the event vertex, and subtending a solid angle Ω_i is given by

$$\mu_i = \varepsilon_i \, \Omega_i \, \Phi \, \exp(-r_i/\lambda_s),$$

assuming that light attenuation is only due to extinction. Although the scintillation attenuation length λ_s and the individual quantum efficiencies of the PMTs are wave-length dependent, only average, effective values are used in this approach. All reconstruction parameters (attenuation lengths, solid angles and quantum efficiencies) are determined self-consistently, from control data samples. Furthermore, since any constant can be easily absorbed in the definition of the light flux Φ, only the relative quantum efficiencies are relevant in this approach.

The charge likelihood $\mathcal{L}_q(q; \vec{\alpha})$ for any given PMT is directly obtained from the (normalized) probability of measuring a charge q for a predicted value μ, $\mathcal{P}(q; \mu)$, since μ itself

depends on the set of event parameters $\vec{\alpha}$. The negative charge log-likelihood look-up tables will be obtained from the laser calibration data.

The time likelihood for any *hit* PMT is a function of both the corrected time, $t^{(i)}_{corr}$:

$$t^{(i)}_{corr} = t_i - t - \frac{r_i}{c_n},$$

and also the predicted scintillation and Cherenkov charge at that particular PMT, $\mu^{(i)}_s$ and $\mu^{(i)}_c$, respectively, namely

$$\mathcal{L}_t = w_s\, T_s(t^{(i)}_{corr}, \mu^{(i)}_s) + w_c\, T_c(t^{(i)}_{corr}, \mu^{(i)}_c),$$

with the weights

$$w_s = \frac{\mu^{(i)}_s}{\mu^{(i)}_s + \mu^{(i)}_c} \qquad \text{and} \qquad w_c = \frac{\mu^{(i)}_c}{\mu^{(i)}_s + \mu^{(i)}_c}.$$

The underlying scintillation and Cherenkov time likelihoods, $T_s(t_{corr}, \mu_s)$ and $T_c(t_{corr}, \mu_c)$, respectively, will be extracted from laser calibration data, and verified self-consistently from the regular data.

Particle identification (PID) can be based on the standard pulse shape discrimination, which exploits the difference in the scintillation timing profile between positrons and neutrons (protons). In particular, the fraction of late light calculated under a single hypothesis event reconstruction can yield a PID which yields sufficient separation between signal and background events. Alternatively, a stronger separation can be achieved using the event likelihood ratio (or log-likelihood difference), where each event is reconstructed under two hypotheses, an electron hypothesis – which yields $\mathcal{L}_e$, and a neutron hypothesis – which yields $\mathcal{L}_n$. The resulting log-likelihood difference, $\ln(\mathcal{L}_e/\mathcal{L}_n)$, fully utilizes all differences between electrons and neutrons, both in timing and in spatial charge distribution.

4 Understandings of the Background and Expected Detector Performance

4.1 Expected Detector Performance

4.1.1 Energy Resolution

The light yield of the 0.1w%Gd-LS is 10000 photons/MeV, and the attenuation length is more than 10 m at a wavelength of 430 nm. The acceptance of the 193 8-inch PMTs is ∼11% at the detector center, and considering the QE x CE for the PMTs, the total number of photoelectrons detected for all 8-inch PMTs is ∼200/MeV. Figure 63 shows the visible energy resolution as a function of the energy. The energy resolution can be assumed to be approximately given by $\sqrt{\frac{p0^2}{E} + p1^2}$, where, E is energy, $p0$ is contribution of the total number of photoelectrons, and $p1$ is a constant term related to hardware. The constant term is assumed to be 2% in Fig. 63, consistent with the choice in reactor neutrino experiments [62]. The black point at each energy in Fig. 63 shows the energy

resolution of the MC result including the light yield, attenuation length of the Gd-LS and uniformity of the energy resolution due to vertex position dependence. The red line shows the fit result to the black points with the approximate formula from above. The overall energy resolution (p0) from the fit result is calculated as $7\%/\sqrt{MeV}$. In the higher energy range of several tens MeV, the effect of the constant term on the energy resolution is dominant in this detector design.

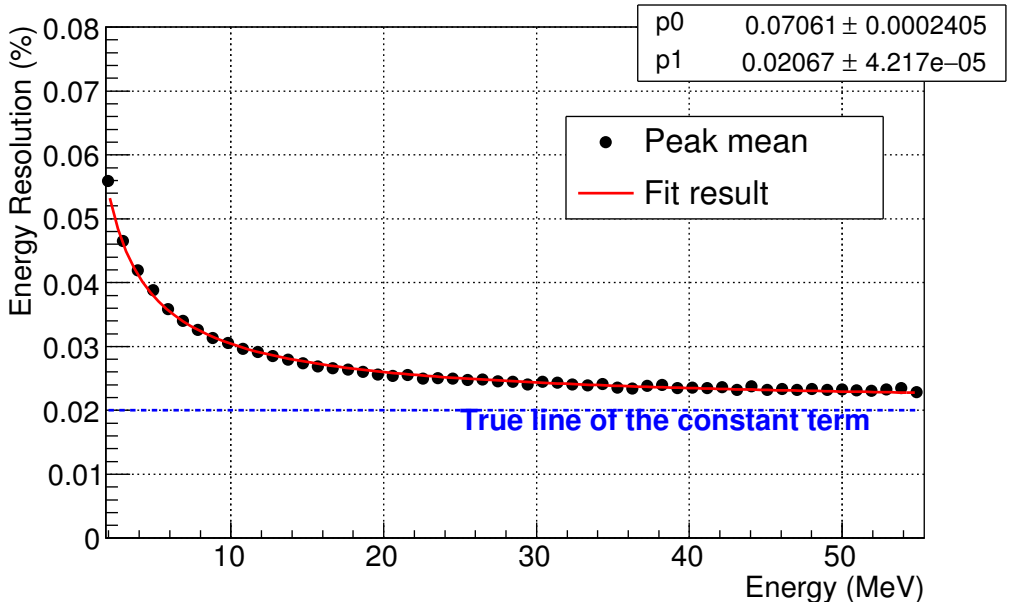


Figure 63: Correlation between energy resolution and energy. Black points show the MC result, red line shows fit result to the black points with an approximate formula.

4.1.2 Pulse Shape Discrimination (PSD) capability

Because the JSNS^2 detector is set above ground, it is necessary to reduce the cosmic-induced fast neutron background dramatically compared to an equivalent underground experiment. It is then indispensable for the JSNS^2 detector to have strong PID capabilities to be able to reject signals from cosmic-induced fast neutrons. Cosmic-induced fast neutrons mimic the IBD coincidence. Recoil protons from the fast neutron mimic the prompt IBD ionization signal and the neutron eventually thermalizes and captures on Gd. This completely mimics the IBD process. Compared to the positron from the IBD signal, the waveform generated by a recoild proton is wider due to differences in the dE/dx between the two particles. By exploiting this difference, the IBD signals can be distinguished from the cosmic-induced fast neutrons analytically. In this TDR, a ratio of the integrated charge in the tail of the prompt waveform to the charge in the full waveform is used as a PSD variable for the analysis (Tail Q/Total Q).

In order to evaluate the PSD capability of the JSNS^2 detector, the PSD performance of the RENO type Gd-LS was measured using a 100 mL vial exposed to a 70 MeV neutron beam produced by CYRIC [63] at Tohoku University in Japan in November,

2015. The data was taken using a CAEN V1730 (500MS/s, 14bits) digitizer. The top image in Fig. 64 shows the experimental room at CYRIC. The proton beam comes from the left side, and hits ^{7}Li target, which causes the emission of neutrons. The neutrons pass through a collimator and interact with hydrogen and carbon in the Gd-LS. The scintillation light is viewed by a 2-inch PMT. The bottom pictures in Fig. 64 show the experimental setup.

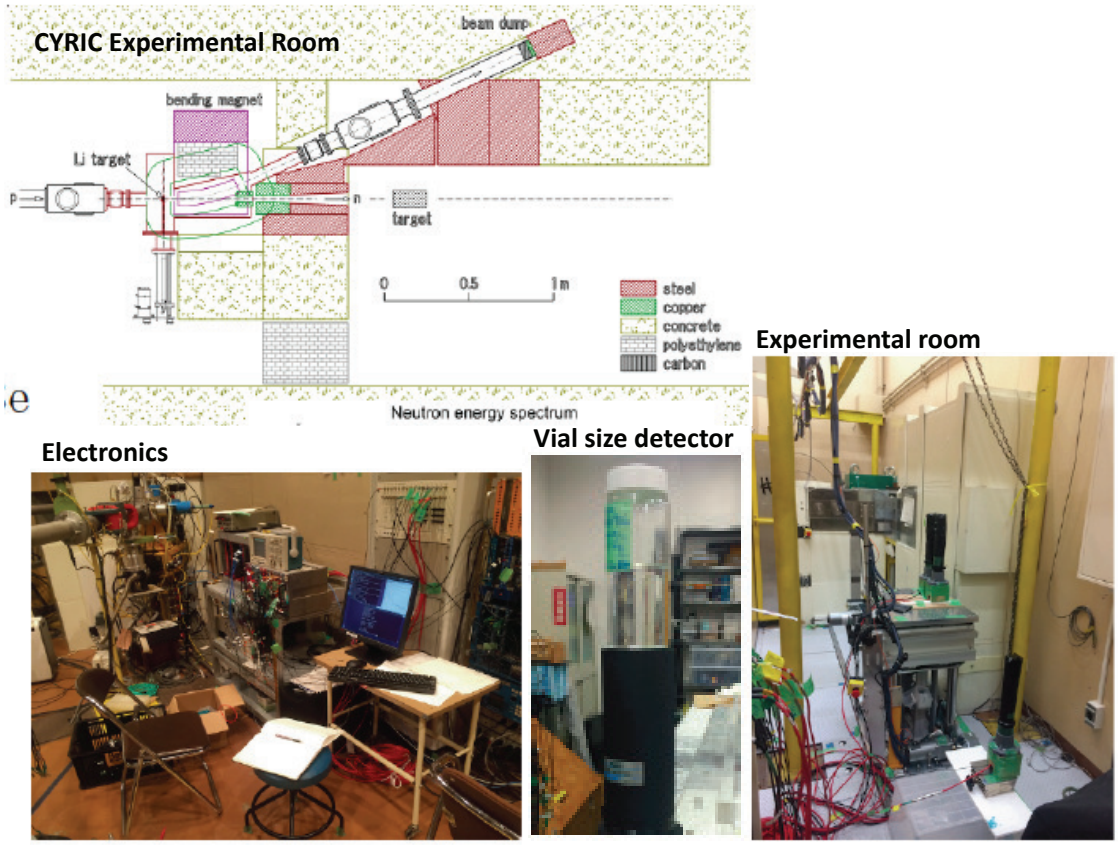


Figure 64: Figure showing the CYRIC experimental room and pictures of the experimental setup.

The measured data is compared to the MC samples produced by Geant4 which include the optical process and reconstruction of the waveform including electronics effects. The MC simulation was already tuned with radioactive sources of ^{60}Co and ^{241}Am^{9}Be before the test-beam. Figure 65 shows mean waveforms of the recoiled protons of measured data and MC, the measured waveform is reproduced well in MC. Figures. 66 and 67 show correlations between the TailQ/TotalQ and the visible energy of measured data and the MC samples, respectively. The TailQ/TotalQ definition is shown in Fig. 65. Figure 68 shows correlations between the mean (RMS) of the TailQ/TotalQ distributions and the visible energy for the measured data and the MC samples. Though there is a small discrepancy between the RMS curves and the mean curves, the MC samples reproduce the measured data reasonably. The PSD performance of the scintillator when exposed

to fast neutrons with several tens MeV in the Gd-LS is well-understood using the MC simulation.

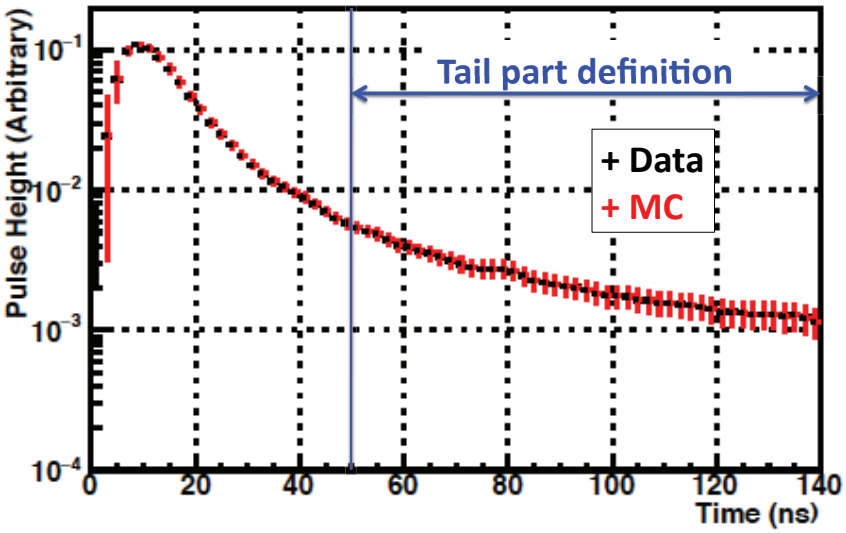


Figure 65: Mean waveforms of the recoil protons of data and the MC simulation. The blue arrow shows the definition of the tail region for computing Tail Q/Total Q.

Finally, using the MC simulation, the PSD capabilities of the real JSNS^2 detector are checked. Figure 69 shows the Tail Q/Total Q distributions for the neutrino signals and the cosmic-induced fast neutrons after applying the usual neutrino selection criteria. The neutrino signals and the fast neutrons are generated with same methods as the previous status report [64]. The result indicates that the JSNS^2 detector has good enough PSD capability to distinguish the neutrino signals from the cosmic-induced fast neutrons, and most of fast neutron events can be rejected without reduction of the signal efficiency. For example, if we cut the events by 0.135 in the horizontal axis in Fig. 69, the detection efficiency for the signal is 99±0.1%. Usually, the PSD capability of a large detector such as JSNS^2 detector becomes worse than the vial size test sample because the waveform containing the timing information from the scintillation emission is distorted by vertex reconstruction bias. In that case, the discriminating power offered by the Tail Q/Total Q distribution becomes worse and the PSD performance suffers. Such and effect is considered in this result.

4.1.3 Selection criteria and the signal efficiency

Table 13 shows selection criteria for the neutrino signals and the signal efficiencies. A detailed explanation is given in [64]. The total signal efficiency is 38%.

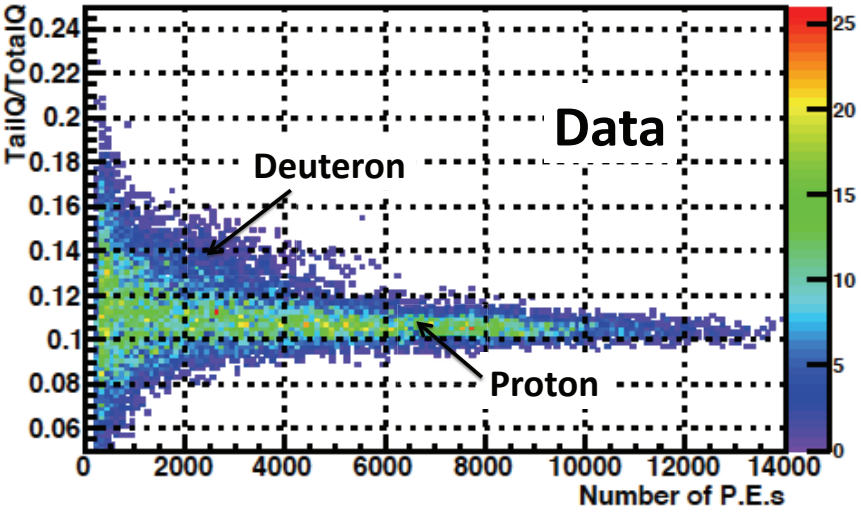


Figure 66: Correlation between the Tail Q/Total Q and the visible energy of measured data.

4.2 Summary of 2014 Measurement

To investigate the feasibility of the experiment, we measured the background at the detector location using 500 kg of plastic scintillator in 2014. The results were summarized in the status report and a PTEP publication [64, 65], and therefore only the relevant parts are written in the TDR.

There are four categories for the backgrounds:

- For the IBD prompt region ($20 < E_p < 60$ MeV, $1 < T_p < 10$ μs)
  - Beam neutrons and gammas
  - Gamma rays and neutrons induced by cosmic rays.
- For the IBD delayed region ($7 < E_d < 12$ MeV, $T_p < T_d < 100$ μs)
  - Gammas and neutrons induced by beam
  - Gammas and neutrons induced by cosmic rays

The dominant background for the IBD prompt region comes from gammas induced by cosmic rays, not from the beam. Figure 70 shows the energy (MeV) vs timing (ns) of the neutral particles (neutrons or gammas) around the proton beam timing. As seen in the plot, there are no backgrounds in the prompt (positron) signal region.

We also measured the neutral particle backgrounds induced by cosmic rays. As shown in the Fig. 11 of [64], the MC simulation reproduces the data well and the estimated background is shown in the table.

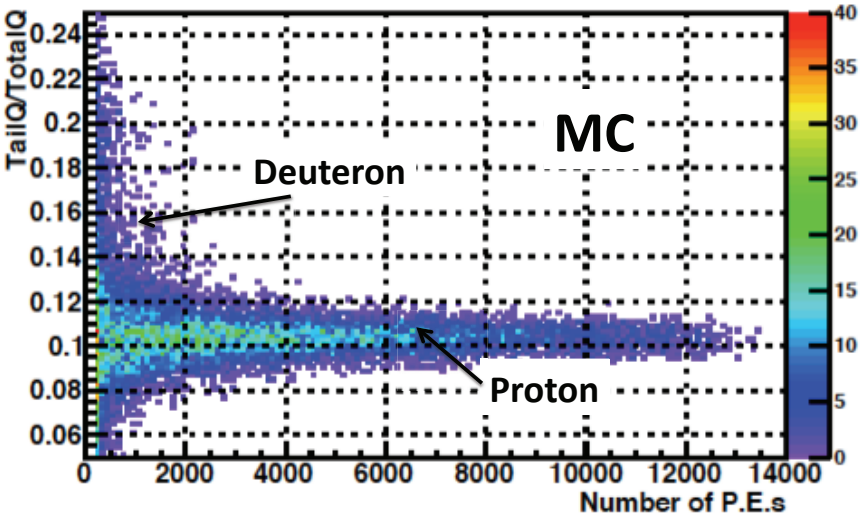


Figure 67: Correlation between the Tail Q/Total Q and the visible energy in the MC samples. The recoil proton events are reproduced especially well.

The delayed backgrounds are due to beam, especially, gammas from the floor concrete under the detector induced by beam. You can see the neutral particle activity with less than 10 MeV in Fig. 70 as well. To terminate the gammas, we plan to put 30 cm thick iron plates (equivalent to 12.5cm thick lead blocks) under the JSNS^2 detector which makes this background manageable. The effect of the lead with thickness up to 10 cm was measured and is shown in Appendix C of [64]. For this background, we also created a MC model for the gammas, and the energy and relative rate as a function of lead thickness is well reproduced by the MC.

Thermal neutrons are not observed in the plastic scintillator, and the rejection power for the thermal neutrons coming from outside of the detector within the veto region of the JSNS^2 detector is quite high as shown in Fig. 17 in [64]. The rejection power is more than 10^5, and therefore the effects of thermal neutrons are negligible. The delayed background from neutrons comes from beam neutrons which thermalize inside the detector. The neutrons in the beam timing window can be tagged using LS light, therefore the thermal neutron backgrounds from beam are significantly reduced using the proton on-bunch timing activity inside the LS.

In summary, all dominant backgrounds were measured by a 500 kg detector and were well reproduced by MC simulations which we implemented. The simulations were used to estimate the backgrounds in the real JSNS^2 detector. As a result of the simulation, we found that all these backgrounds can be controlled by the detector design presented here allowing us to perform the experiment effectively, and therefore the PAC recommended stage-1 status after seeing the results in 2014.

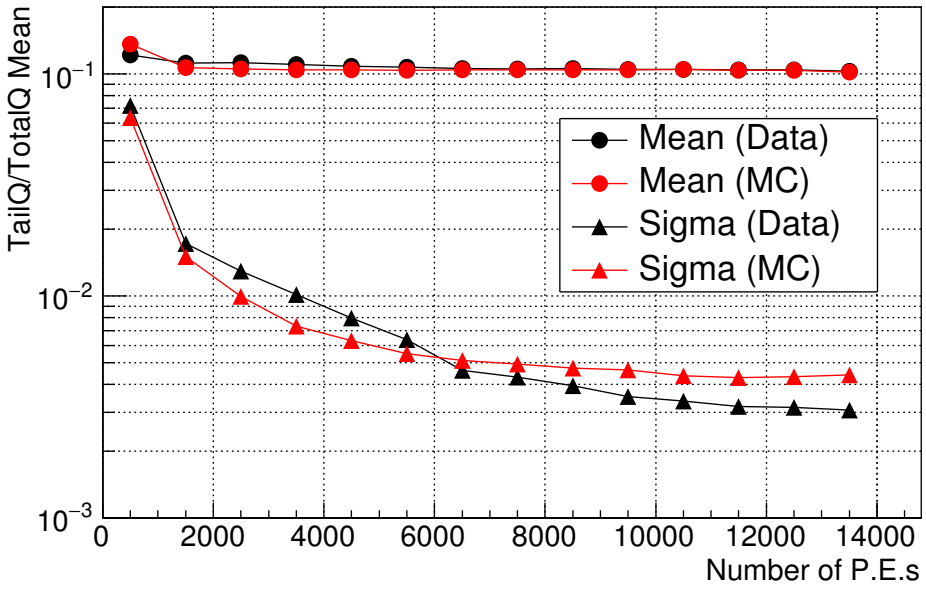


Figure 68: Correlations between mean (RMS) of the TailQ/TotalQ and the visible energy for the measured data and the MC samples.

4.2.1 Revised Numbers from the Reference

After submitting [64] to PAC, we found that the gammas induced by cosmic rays (Fig. 12 in [64]) can also be a prominent background in the IBD delayed region. We discarded this due to the time window difference unintentionally.

The estimated number of gammas / spill / 100μs is 4.4×10^{-3}/spill/100μs. This gives a larger accidental background 3.8 times higher than the rate given in [64].

We use the latest estimation of the accidental background in this TDR.

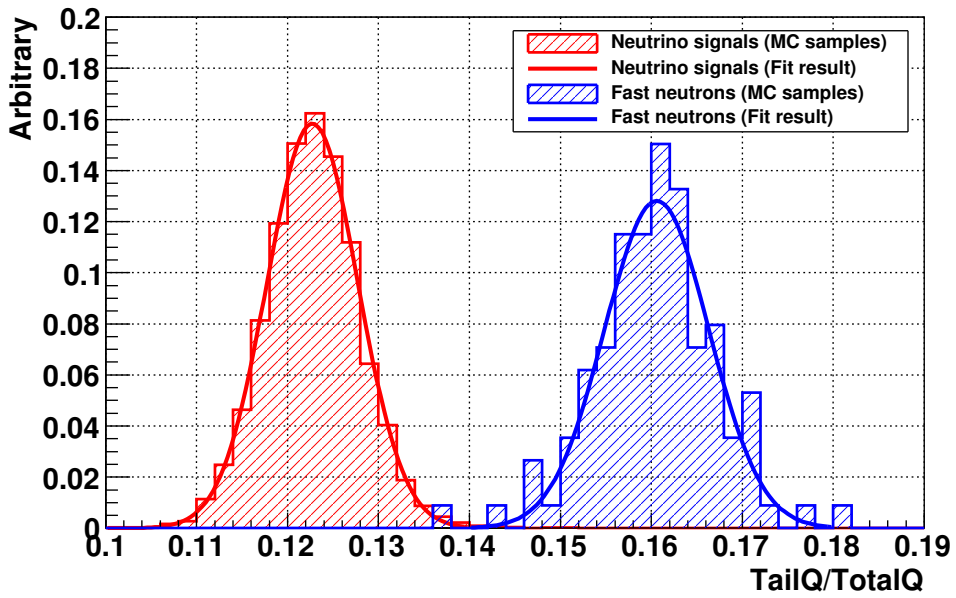


Figure 69: The Tail Q/Total Q distributions for the neutrino signals (red) and the cosmic-induced fast neutrons (blue) after applying the usual neutrino selection criteria.

Cut condition	Efficiency
$1 \leq \Delta t_{prompt} \leq 10\mu s$	74%
$7 \leq E_{delayed} \leq 12MeV$	71%
$20 \leq E_{prompt} \leq 60MeV$	92%
$\Delta t_{delayed} \leq 100\mu s$	93%
$\Delta VTX_{prompt-delayed} \leq 60cm$	96%
$\Delta VTX_{OB-delayed} \geq 110cm$	98%
Life Time ≤ 11	91%
PSD cut	$\sim$ 99%
Total	38%

Table 13: Selection criteria for the neutrino signals and the signal efficiencies.

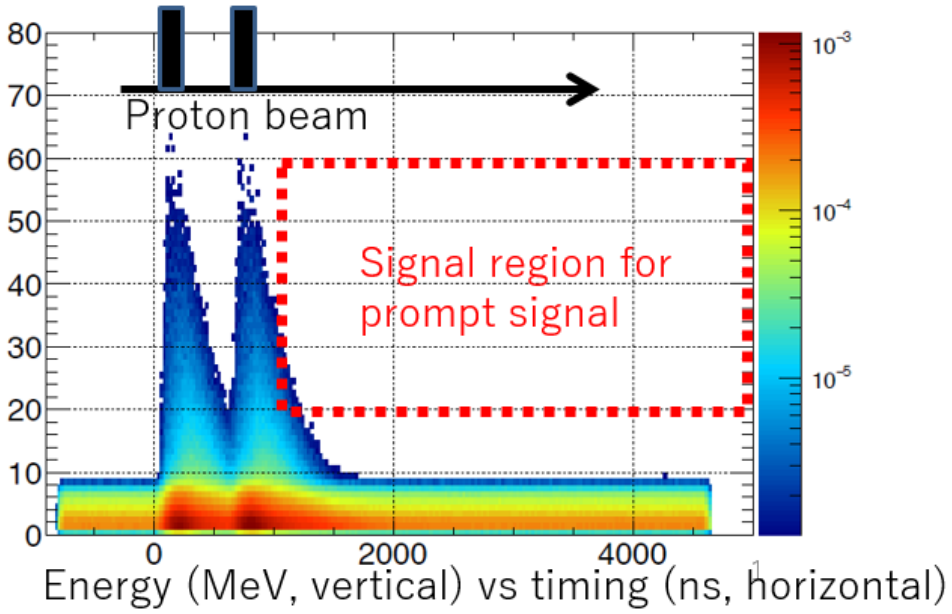


Figure 70: The measured energy vs timing w.r.t. the proton beam timing of neutral particles using 500 kg plastic scintillator [64, 65].

4.3 Summary of Backgrounds

Table 14 shows a summary of the number of background and signal events in the JSNS^2 experiment. The baseline of the detector from the target is 24 meters and the operation period is 5000h×3 years for one 17-ton detector, which includes the latest accidental background estimation described in section 4.2.1. and it also shows the 5000h×5 years case with the 50 tons used in [64].

The dominant background is $\overline{\nu}_e$ from μ^-, which is 43, while the signal is 62 in case of the best fit values of LSND, with a 17-tons detector and a 3-year measurement period (5000 h×3 years).

	Contents	this TDR 1 detector 5000h×3y	Reference 50tons 5000h×5y
Signal	$sin^2 2\theta = 3.0 \times 10^{-3}$ $\Delta m^2 = 2.5eV^2$ (Best fit values of MLF)	87	480
	$sin^2 2\theta = 3.0 \times 10^{-3}$ $\Delta m^2 = 1.2eV^2$ (Best fit values of LSND)	62	342
background	$\overline{\nu}_e$ from μ^-	43	237
	$^{12}C(\nu_e, e^-)^{12}N_{g.s.}$	3	16
	beam-associated fast n	$\leq$2	$\leq$13
	Cosmic-induced fast n	negligible	37
	Total accidental events	20	32

Table 14: Summary of the event rate for 5000h×3years for one 17-ton detector (middle) and the same for 5000h×5years for the 50 ton case[64](right). Note that the event rate for 5000h×3years for one 17-ton detector (middle) includes the latest accidental background estimation described in section 4.2.1

5 Sensitivity for the Sterile Neutrino Search

5.1 Fit method

The binned maximum likelihood method is used for the analysis. The method fully utilizes the energy spectrum of the background and signal components, and thus the amount of the signal can be estimated efficiently.

The typical energy spectrum from μ^- decay (blue), the oscillated signal with (Δm^2, $\sin^2 2\theta$) = (2.5, 0.003) (brown shaded; best Δm^2 case) and (1.2, 0.003) (LSND best fit case), are shown in Figs. 71 and 72, respectively. Here we assume the fiducial mass of the detector is 17 tons, 1 MW beam power is available at the MLF, the detector is 24 m from

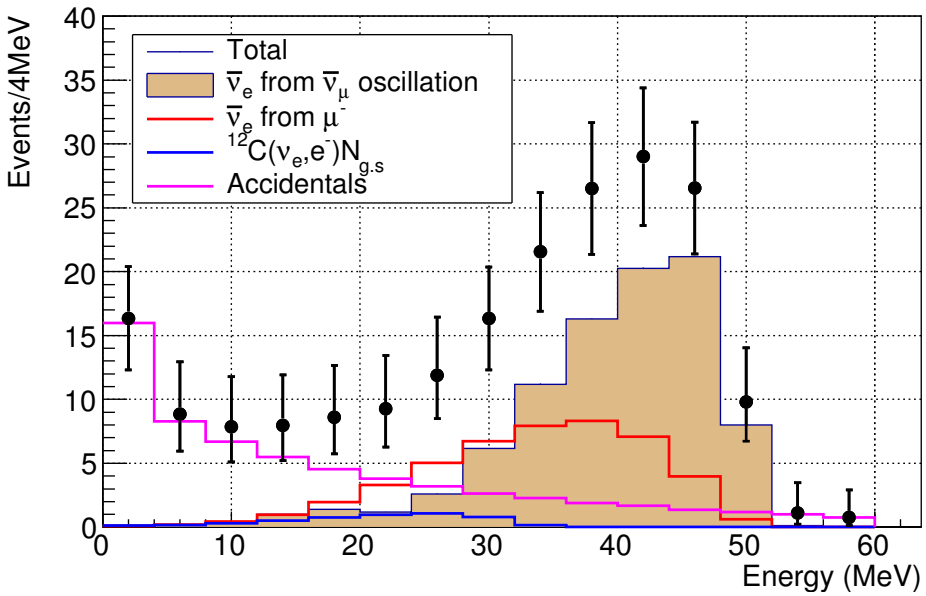


Figure 71: Energy spectra of $\bar{\nu}_e$ from μ^- (red),$^{12}C(\nu_e, e^-)N$ (blue), accidentals (pink), and the oscillated signal with $(\Delta m^2, \sin^2 2\theta) = (2.5, 0.003)$ (brown shaded; best Δm^2 for the MLF experiment) are shown. Black points with error bars correspond to the sum of the all components. All spectra of the neutrino signals and all backgrounds except for the beam neutrons include the effect of the energy resolution shown in Fig.63.

the target, and three years of operation with 5000 hours of exposure each year is achieved. The signal detection efficiency is assumed to be 38% in Table 13. The number of events in each energy bin is statistically small, therefore we use maximum likelihood instead of the usual minimum χ^2 method. The fitter estimates the oscillation parameters by varying the size and shape of the brown histogram to best reproduce the energy distribution of the black points.

For this analysis, the following equation is used to compute the likelihoods:

$$L = \Pi_i P(N_{exp}|N_{obs})_i \quad (3)$$

$$P(N_{exp}|N_{obs}) = \frac{e^{-N_{exp}} \cdot (N_{exp})^{N_{obs}}}{N_{obs}!} \quad (4)$$

where, i corresponds to i-th energy bin, N_{exp} is expected number of events in i-th bin, N_{obs} is number of observed events in i-th bin. i starts from 20 MeV and ends at 60 MeV because the energy cut above 20 MeV is applied for the primary signal as explained before. Note that $N_{exp} = N_{sig}(\Delta m^2, \sin^2 2\theta) + \sum N_{bkg}$, and $N_{sig}(\Delta m^2, \sin^2 2\theta)$ is calculated using the two flavor neutrino oscillation equation shown before, $P(\bar{\nu_\mu} \to \bar{\nu_e}) = \sin^2 2\theta \sin^2(\frac{1.27 \cdot \Delta m^2(eV^2) \cdot L(m)}{E_\nu(MeV)})$.

The maximum likelihood point gives the best fit parameters, and $2\Delta lnL$ provides the uncertainty of the fit parameters. As shown in the PDG [28], we have to use the $2\Delta lnL$ for 2 parameter fits to determine the uncertainties from the fit.

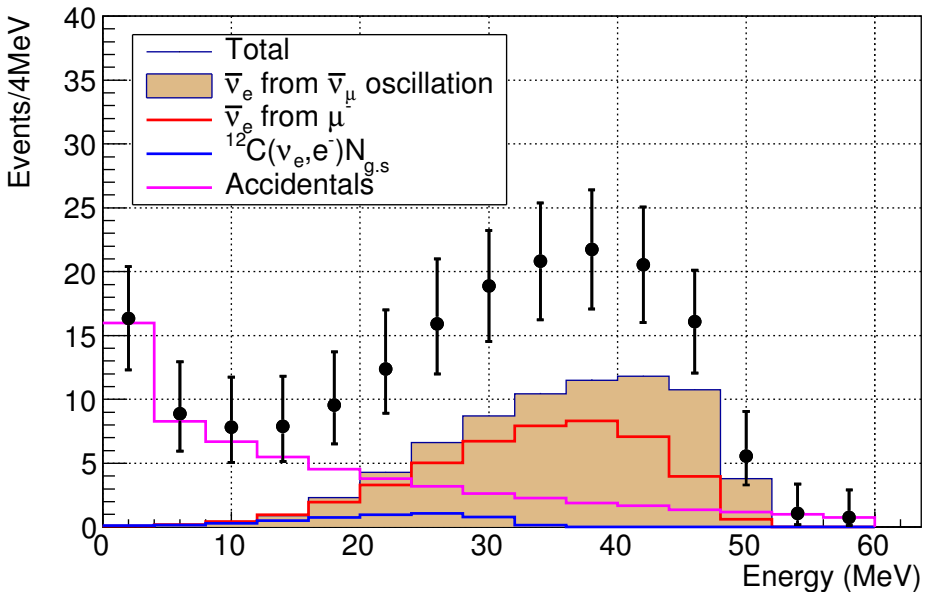


Figure 72: Energy spectra of $\bar{\nu}_e$ from μ^- (red),$^{12}C(\nu_e, e^-)N$ (blue), accidentals (pink), and the oscillated signal with $(\Delta m^2, \sin^2 2\theta) = (1.2, 0.003)$ (brown shaded; LSND best Δm^2 for the MLF experiment) are shown.

5.2 Systematic uncertainties

Equation 3 takes only statistical uncertainty into account, therefore the systematic uncertainties should be incorporated in the likelihood. Fortunately, the energy spectrum of the oscillated signal and background components are well known, thus the error (covariance) matrix of energy is not needed. In this case, uncertainties on the overall normalization of each component have to be taken into account, and this assumption is a good approximation at this stage.

In order to incorporate the systematic uncertainties, constraint terms should be added to Equation 3 and the equation is changed as follows:

$$L = [\Pi_i P(N^{'}_{exp}|N_{obs})_i] \times e^{-\frac{(1-f_1)^2}{2\Delta\sigma_1^2}} \times e^{-\frac{(1-f_2)^2}{2\Delta\sigma_2^2}} \quad (5)$$

where f_j are nuisance parameters to give the constraint term on the overall normalization factors. $N^{'}_{exp} = f_1 \cdot N_{sig}(\Delta m^2, \sin^2 2\theta) + f_2 \cdot N_{bkg}$. $\Delta\sigma_i$ gives the uncertainties on the normalization factors of each component.

In this TDR, the profiling fitting method is used to treat the systematic uncertainties. This method is widely known as the correct fitting method. The profiling method fits all nuisance parameters as well as oscillation parameters.

As mentioned above, the flux of the $\bar{\nu}_e$ from μ^- decays around the mercury target has very poor constraints from external information. For this situation, the uncertainty of this background component is set to be 50% and the uncertainty of number of $^{12}C(\nu_e, e^-)N$ events is set to be 10%. We neglect the contributions from the beam and the cosmic-induced neutrons in this study.

5.3 Sensitivity for $\bar{\nu_\mu} \to \bar{\nu_e}$ oscillation

Figure 73 shows the 90% C.L sensitivities with this condition.

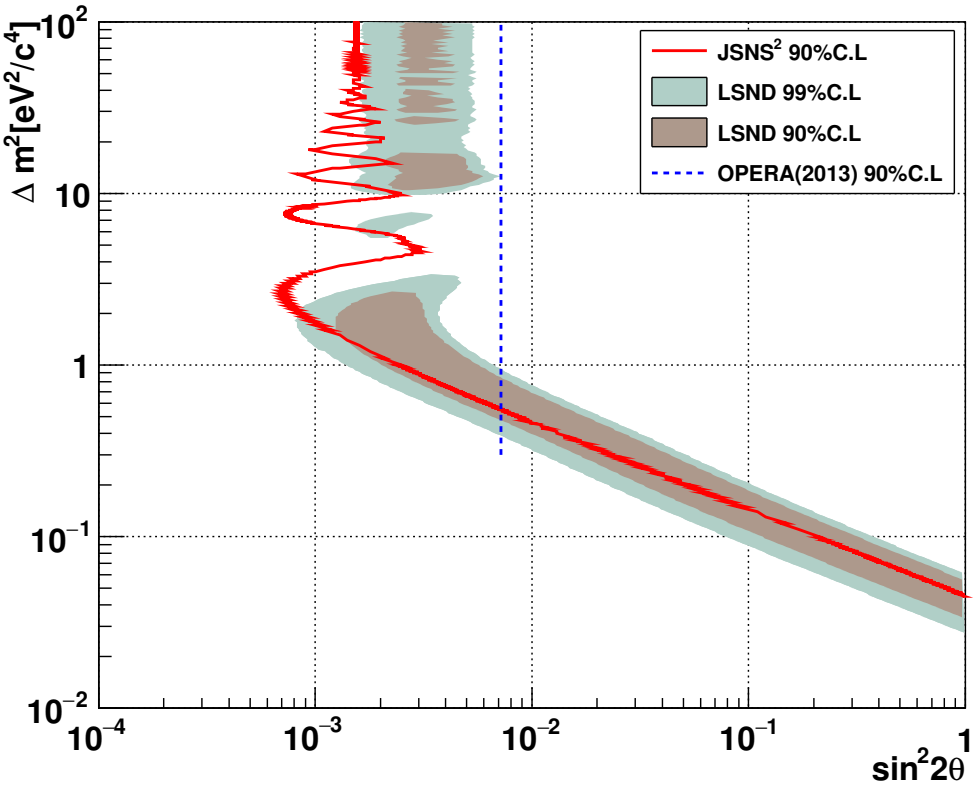


Figure 73: Sensitivity of the JSNS^2 experiment with the latest configuration (1 MW $\times$ 3 years $\times$ 1 detector). The red line shows the 90% C.L.. The exclusion line of the OPERA experiment is also shown [66]. The region to the right of the line is excluded with 90% confidence.

We expect to have the preliminary result in 2021 because our background and energy reconstruction uncertainty is small using the *DAR* neutrino flux and IBD signal. The calibration scheme is relatively straight-forward (with only 200 PMTs). Compared to the world experiments, especially, the SBN program, it is possible to have competitive results from JSNS^2.

6 Summary

The JSNS^2 experiment can provide timely, competitive results in the sterile neutrino search via the $\bar{\nu_\mu} \to \bar{\nu_e}$ mode by utilizing the best existing facility (the J-PARC MLF) and established detector techniques. JSNS^2 is a direct test of LSND and can have a large impact on our current picture of neutrino physics. JSNS^2 can also provide measurements

of other important physics processes including cross section measurements using neutrinos from μDAR and KDAR.

Most of the hardware components of the detector are reliable to use because they have been used in other reactor experiments, and are ready to order. They need about a half of year to be produced. We plan to produce the stainless tank and the acrylic vessel at first in JFY2017, and plan to install the vessel, PMTs, the reflection sheet by the middle of JFY2018. Meanwhile, the Gd-LS and LS will be produced in Korean facility site, and the electronics will be produced by CAEN. The timescale to start the experiment is around of end of JFY2018. In pursuit of these goals, the JSNS^2 collaboration continues to work hard to realize this important experiment.

7 Requests to J-PARC PAC

We request the stage-2 approval to the J-PARC PAC.

8 Acknowledgements

We warmly thank the MLF people, especially, MLF Division leader, the neutron source group, muon group and user facility group for the various kinds of supports. This work is also supported by the JSPS grant-in-aids (Grant Number 16H06344, 16H03967), Japan, and the National Research Foundation of Korea (NRF) Grants 2009-0083526 and 2017K1A3A7A09015973. Finally, we thank the continuous supports from J-PARC and KEK.

A Strength Calculation around the Stainless Tank

In this section, the analysis for the strength calculation for the stainless tank, the tank support structure, the lifting structure during the earthquake as well as the static status. This includes how to fix the tank to the building with the anchors. Note that these calculations are done by the Mitsui-Zosen company, and the cross checked between hand calculation and FEM analysis each other.

A.1 Thickness of the Stainless Tank for the Static Operation

A.1.1 Wall

Table 15 shows the inputs for the calculation for the stainless tank.

Parameter Name	Parameter
Diameter (D)	4600 mm
Height (H)	3500 mm
Maximum liquid pressure (P_1)	0.35 kg/cm^2
Internal Pressure (P_2)	1.0 kg/cm^2
Design Pressure (P)	1.37 kg/cm^2
Material	SUS301
Maximum allowable stress of SUS301 (σ_a)	13.1 kg/mm^2
Liquid inside tank	Water (for conservative calc.)
Density of water	1g/cm^3
Efficiency of Welding (η)	0.70
Corrosion factor (C)	0.0

Table 15: Parameters of the inputs of the strength calculations.

The minimum thickness (t) of the stainless tank wall is given by the following formulae;

$$t = \frac{P \cdot D}{200\sigma_a \cdot \eta - 1.2P} + C \tag{6}$$

and it is t = 3.4 mm. The minimum commercial (available) thickness of the stainless sheet is 5.0 mm and this calculation contains the safety factors (4.3) due to the liquid density (LAB 0.86 g/cm^3) and internal pressure of 1.0 kg/cm^2 (we will use N_2 gas with 0.0 level internal pressure but not in the such high pressure). The thickness of 5.0 mm is safe with the safety factor of 6.3.

A.1.2 Top

In this calculation, we need another parameter, "curvature radius of the top roof (flange) of the tank (R) ", which we assume 12,000 mm. If we use similar equation as

the Eq. 6 as follows,

$$t = \frac{P \cdot R}{200\sigma_a \cdot \eta - 0.2P_2} + C \tag{7}$$

we obtain the minimum thickness of the top flange. It is 6.5 mm. We use 10mm thickness of stainless for this part, and also the internal pressure is almost 0.0, therefore the safety factor is very large.

A.2 Strength of Stainless Tank during the Earthquake

A.2.1 Wall Part

When the earthquake is occurred, the detector must not have buckling effects. We assume 0.25G is loaded to the detector wall during the earthquake. Note that 0.25G is the same assumption of the weight load as the other MLF building materials during the earthquake.

The total weight of the stainless tank and the first "Anti oil-leak tank" is about 58.5 tons, therefore the maximum horizontal weight load during the earthquake is 0.25×58.5 = 14.6 tons.

The center of gravity for the height is 1.75 meter, then the corresponding bending moment (M_h) is 25.6 ton · m.

The cross sectional second moment for the detector wall is

$$I = \pi r_m^3 t = 1.90 \times 10^{11} mm^4 \tag{8}$$

where, t is the thickness of the detector wall (5mm) and r_m^3 is the average radius of the detector (2297.5 mm). The cross section coefficient ($Z = I/r_m$) is $8.29\times10^7 mm^3$. **The expected stress from the bend compression ($\sigma_m = M_h/Z$) during the earthquake is 0.31 kg/mm^2.**

On the other hand, the maximum compression stress from the theory is expressed as:

$$\sigma_{cr} = \frac{E}{\sqrt{3(1-\nu^2)}} \cdot \frac{t}{r} \sim 0.6E\frac{t}{r} \tag{9}$$

where, ν is Poisson ratio (0.3 at this case) and E is the elastic coefficient which is 21000 kg/mm^2. Then the maximum stress is 28.0 kg/mm^2, therefore this value is much larger than the expected stress. **The detector is not broken during the earthquake.**

A.2.2 Welding Condition to Prohibit Sliding of the Detector

In this subsection, we consider the welding condition not to have sliding between the detector tank and the support structure.

The maximum horizontal weight load during the earthquake as shown in the previous subsection is 0.25×68.5 = 17.1 tons. Although the friction coefficient of the detector tank is 0.1∼0.3, here we assume all 17.1 tons acts as the sliding force because of the safety reason.

The welding part can stand up to 7.24 kg/mm^2 for shearing force at most[2], thus the needed welding area to prohibit the sliding is 17.1 tons / 7.24 kg/mm^2 = 2363.7 mm^2.

According to Fig. 74, the resistance area of against the shearing force is a$\times \cos \pi/4 =$ 3.5mm, therefore the required length of the welding region is 2363.7 / 3.5 = 668.6 mm. **Our welding design satisfies this requirements.**

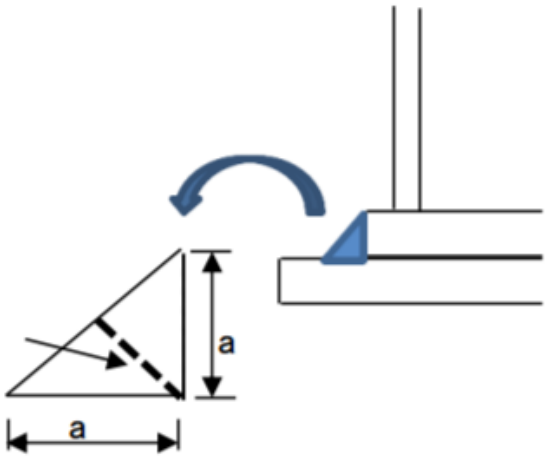


Figure 74: The length of "a" is assumed to be 5 mm, which is same as the thickness of the stainless sheet. In this case, corresponding resistance area against the shearing force is a$\times \cos \pi/4 =$ 3.5mm.

A.3 FEM calculation

In this subsection, the results using the FEM calculation is shown. Figure 75 shows the setup of the FEM calculation.

Tables 16 and 17 show the parameter for the materials and size of the relevant detector components.

Material	Elastic coefficient (N/m^2)	Poisson Ratio	density (kg/m^3)	comments
Steel	2.06×10^{11}	0.3	7850	
Stainless	1.96×10^{11}	0.3	7930	
Gum	3.31×10^{5}	–	–	modeled as the springs

Table 16: Parameters of materials in the FEM .

A.3.1 Static Operation

The static operation case is considered at first. The maximum stress, the maximum

[2]This value is based on the Japanese law

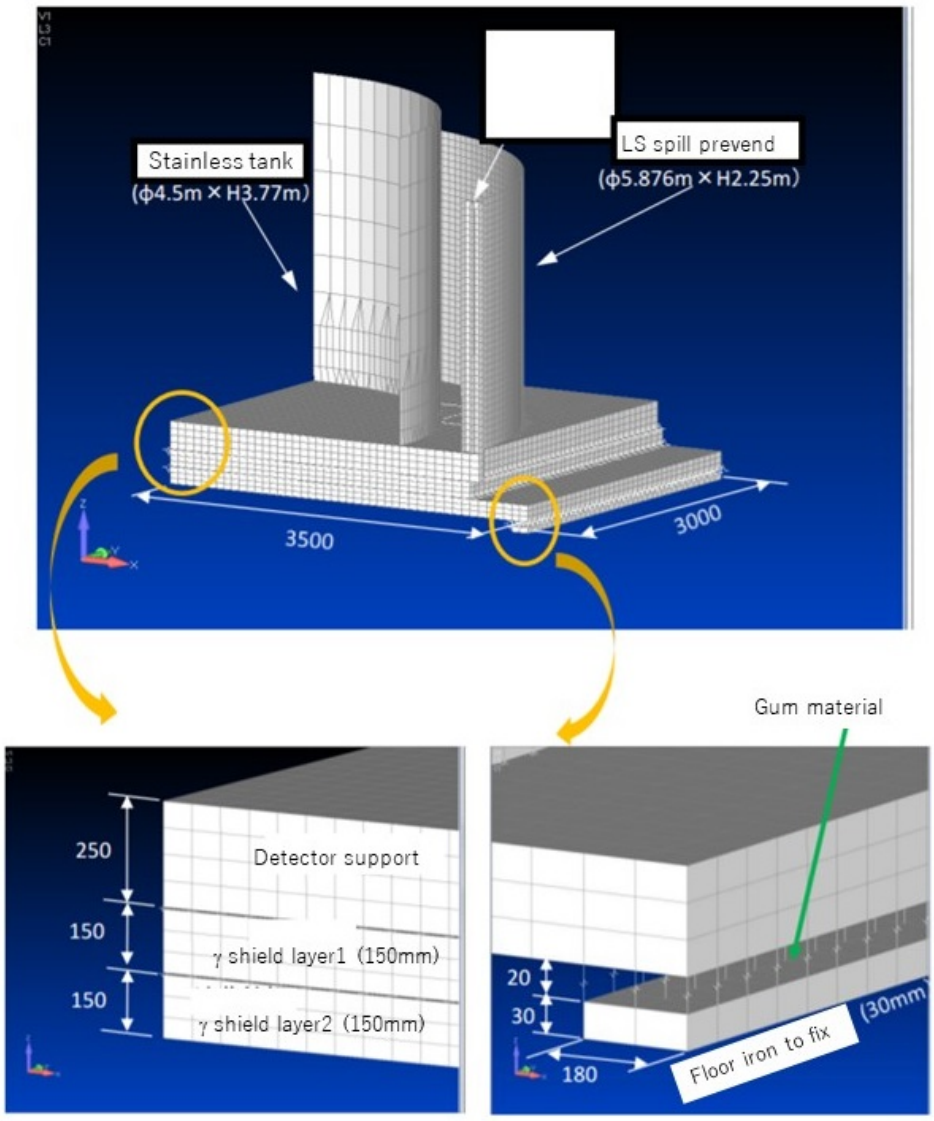


Figure 75: The setup of the FEM calculation. The quarter of the detector is shown for the simplicity hereafter unless it is noticed.

Component	thickness (mm)	length (mm)	width (mm)	comments
γ shield layer 2	150	7000	6000	
γ shield layer 1	150	5876	6000	
iron sheet to fix the detector	30	6000	200	
Gum (on the iron sheet)	20	6000	200	
Support (top sheet)	9.0	5876	5876	
Support (bottom sheet)	9.0	5876	5876	
Support (H type beam)	6.0	5876	250	every 750 mm
Stainless tank	5.0	–	–	4.5m dia. × 3.77 height
LS Spill Prevention	4.5	–	–	5.876m dia. × 2.25 height

Table 17: Size of the detector components in the FEM .

displacement and the maximum tilting are calculated by the FEM analysis. The expected load parameters are shown in Table 18 during the static operation case,

Parameters	Weight load	comments
Vertical Pressure	34293 N/m^2	liquid+top/bottom tank structure
Material self-weight	9.8 m/s^2	inertia force due to mass
Vertical pressure due to liquid	15148 N/m^2	average of height direction

Table 18: Weight Load Parameters

Figure 76 shows the results visually.

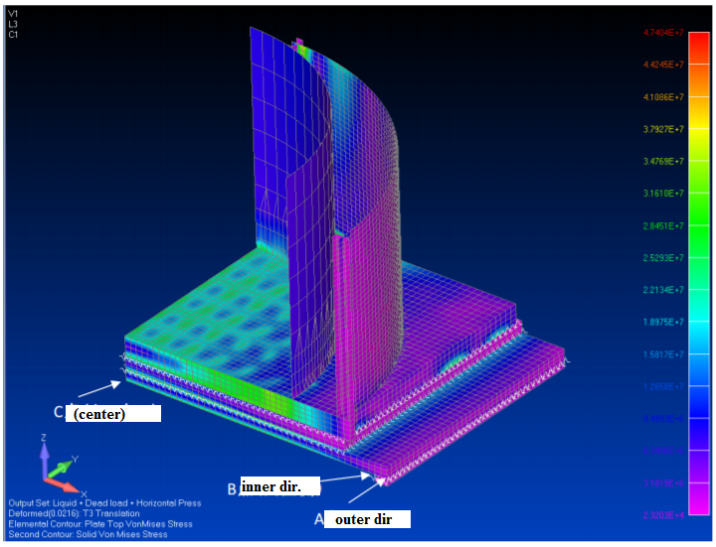


Figure 76: The results for bending and stress calculations.

As expected, the central part of the detector is bent largely. For the quantitative statements, Table 19 shows the comparison between the FEM results and the allowed parameters. Note that allowances are based on the standard values from the Design. ("Kou-kouzou design standard values") All numbers are safe within the standard design, therefore the hand calculation is proved by the FEM analysis as well.

Parameters	Output	Allowance Values
Maximum Stress	73.2 MPa	<158.6 MPa
Maximum Displacement	7.8 mm	–
Maximum Tilting	1/410	< 1/300

Table 19: Comparison between FEM calculation and allowed parameters. Allowances are based on the standard values from the Design. ("Kou-kouzou design standard values')

Figure 77 shows the results of bending and stress for each detector components using

the FEM analysis.

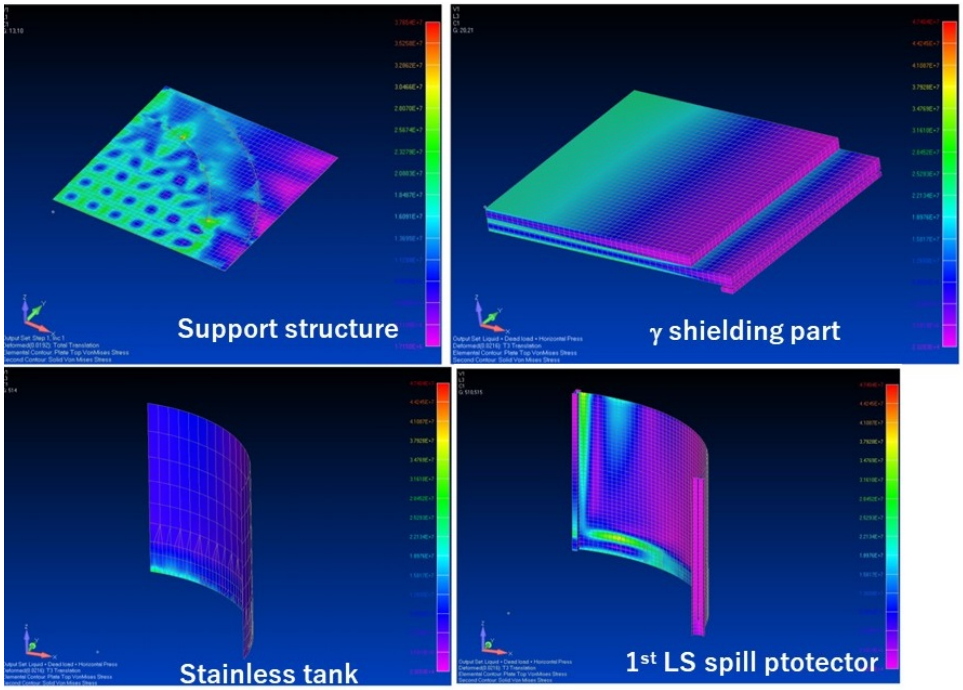


Figure 77: the results of bending and stress for each detector components using the FEM analysis.

Bearing Pressure for Concrete Floor

The concrete floor has the allowed maximum bearing pressure. It is 6000000 N/m^3, which is defined by the standard value of the concrete design in Japan. Thus, we have to check if this detector structure does not break the concrete with the local weights.

To reduce the local weight, we have structure made by iron plates and gums as shown in Fig. 78. The size of the structure is already shown in Table 17.

Using the structure, the FEM calculation shows that the average force to the floor concrete is small enough compared to the allowance by factor of more than 200. **The concrete is not broken using the structure.**

A.3.2 Earthquake case

In this subsection, we calculate the detector's own endemic oscillation mode including whole supports, the γ shields, the "anti oil-leak tank" using FEM analysis. The details are not shown here, but the conclusions from the FEM analysis are as follows:

- The vertical vibration affects to the detector dominantly. Effects from horizontal directional waves are negligibly small.
- The short cycle period of the earthquake wave (>7.85 Hz = cycle period < 0.127

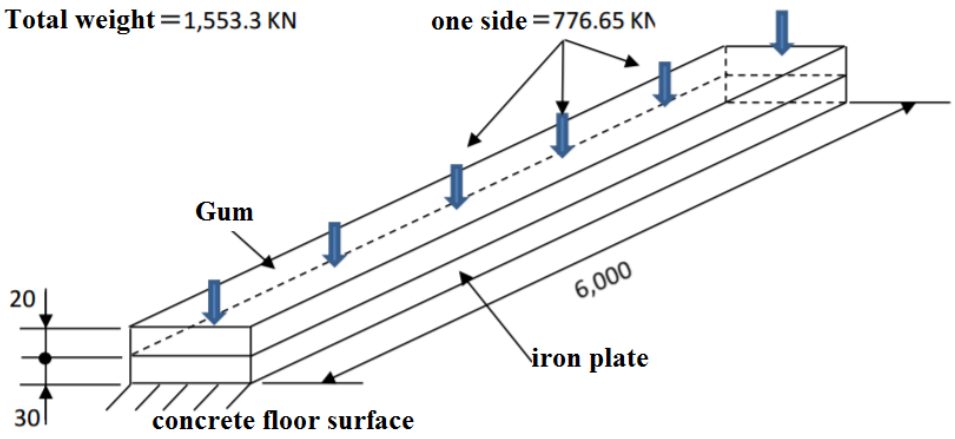


Figure 78: The structure to receive the detector weight made by iron plates and gums to reduce the local weight from the detector.

sec) only affects to the detector. Effects from other frequency regions are also negligibly small.

This is because the detector support, γ shields and iron plates structure has low height weight center, and the wide strcuture for the horizontal directions.

Figure 79 shows the endemic oscillation cycle period of our detector, and the cycle period spectrum of the typical earthquakes (Taft, El Centro, Hachinohe). Compared to the earthquake spectrum peaks, our detector's endemic oscillation cycle period is very low. **We conclude that the usual 0.25G static force to the vertical direction only is good enough to consider the earthquake case from the result.**

Comparison the Results and Allowed Values

Based on the discussion in the previous subsection, we only need to compare static force and the maximum allowance values. For the safety reason, we also compare the horizontal directional case.

Table 20 shows the judgements for the earthquake cases. As expected, **the earthquake does not provide any breaking of the JSNS^2 detector.**

Parameters	Output	Allowance Values
Maximum Stress	91.5 MPa	<237.9 MPa
Maximum Displacement	9.75 mm	–
Maximum Tilting	1/320	< 1/200

Table 20: Comparison between the maximum allowance parameters and the extreme stress during the earthquake, Allowances are based on the standard values from the Design. ("Kou-kouzou design standard Values")

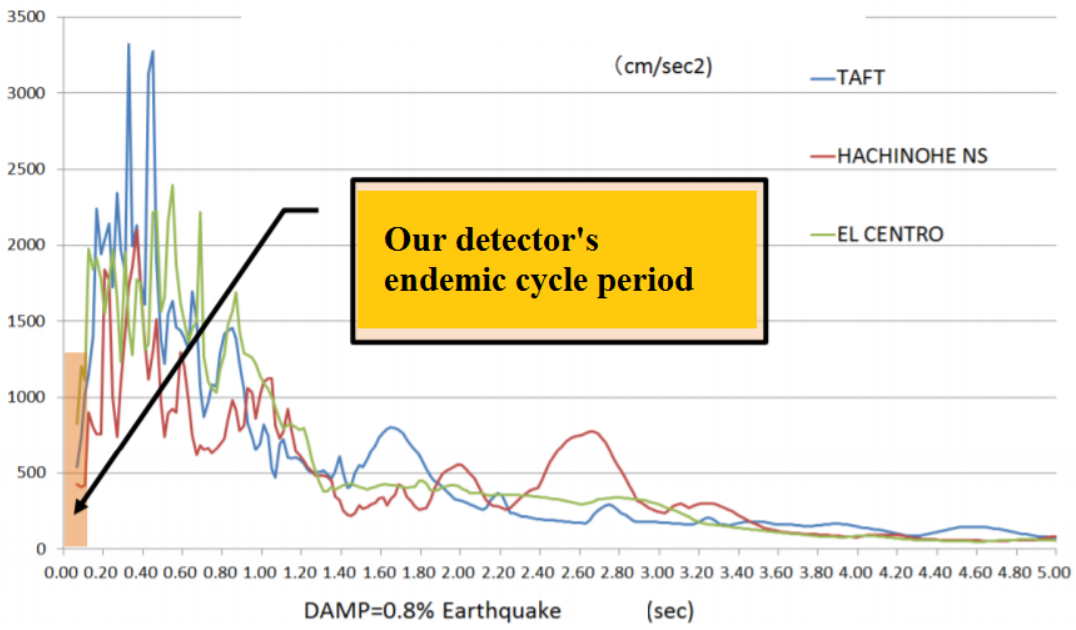


Figure 79: The endemic oscillation cycle period of our detector (orange region), and the cycle period spectrum of the typical earthquakes (Taft, El Centro, Hachinohe). Compared to the earthquake spectrum peaks, our detector's endemic oscillation cycle period is very low.

A.3.3 How to fix the Detector to the Floor

In this subsection, how to fix the detector is described. Figure 80 shows the structure to fix the detector, which consists of iron, gum and pins. Basically, pins stop the sliding the detector during the earthquake.

To calculate the strength of the pins, following assumptions are made:
(1) 0.25G is assumed for the earthquake.
(2) The friction coefficient between iron plates is assumed to be 0. (this include large safety factors because the real coefficient is 0.2∼0.3).
(3) The friction coefficient between iron and gum is more than 0.7, therefore we assume the iron is not moved in this attached areas.

Table 21 shows the strength of the pins to fix the detector (including the detector support, the γ shield layers, gums, the support structure to fix made by iron.) All pins with this design satisfy the requirements.

The bearing pressure of the concrete to fix the pins is also calculated. As shown in Fig. 81, the force is transported from the pins to the concrete hole. The bearing pressure distribution of the concrete which receives the horizontal act force (F_h) is distributed as cosine shape. The maximum bearing pressure (σ) is calculated as;

$$\sigma = F_h/(D/h) = 62.2 kg/cm^2 \tag{10}$$

where, F_h= 4975 kg, D = 80 mm, h = 100 mm.

The tolerance of the concrete for the bearing pressure is 91.8 kg/cm^2, therefore this design is permitted.

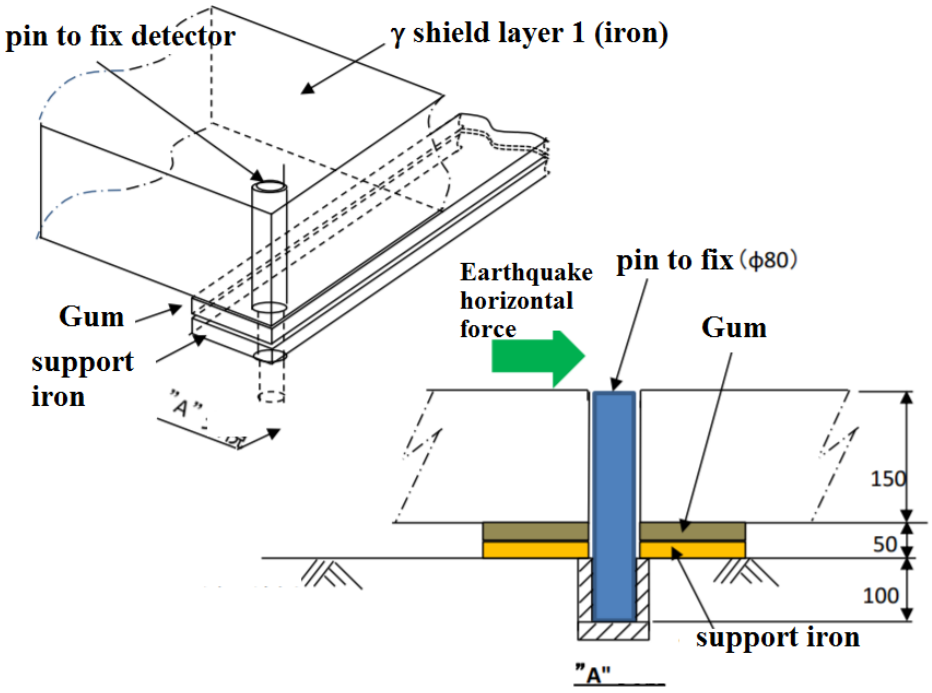


Figure 80: The structure to fix the detector, which consists of iron, gum and pins. Basically, pins stop the sliding the detector during the earthquake.

Parts	Weights (kg)	Horizontal Force (kg)	# of pins	Diameter of pin (mm)	Shearing Force (kg/cm^2)	Tolerance (kg/cm^2)
Detector/γ shield 1	68,243	17,061	4	60	150.8	1086
γ shield 1 / 2	41,514	27,439	4	70	178.2	1086
γ shield 2 / Gum	49,455	39803	8	80	99.0	1086

Table 21: The strength of the pins to fix the detector (including the detector support, the γ shield layers, gums, the support structure to fix made by iron.)

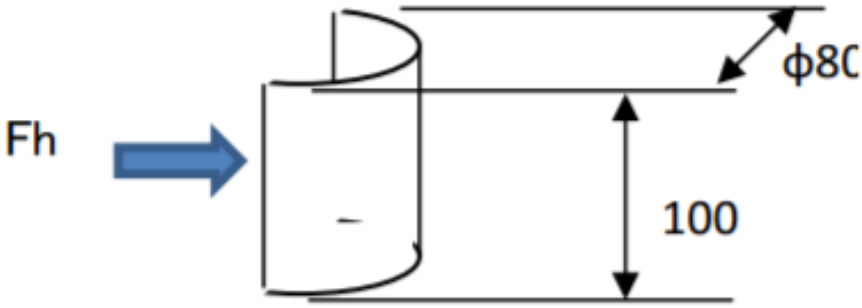


Figure 81: The force from the pins to the hole in the concrete floor.

References

[1] A. Aguilar et al., Phys. Rev. D64, 112007 (2001).

[2] A. A. Aguilar-Arevalo et al. [MiniBooNE Collaboration], Phys.Rev.Lett.110.161801,2013.

[3] C. Giunti and M. Laveder, Phys.Rev.C 83 (2011) 065504

[4] Th. A. Mueller et al., Phys.Rev.C 83 (2011) 054615. P. Huber, Phys.Rev.C 84 (2011) 024617.

[5] J. Kopp et al., arXiv:1303.3011.

[6] M. Antonello et al., arXiv:1307.4699 [hep-ex].

[7] C. Giunti et al., Phys.Rev. D86 (2012) 113014.

[8] F. P. An et al, Phys. Rev. Lett. 113, 141802 (2014)

[9] Y. J. Ko et al, Phys. Rev. Lett 118 (2017) 121802

[10] K. Abe et al, Phys. Rev. D 91, 052019 (2015)

[11] P. Adamson et al, Phys. Rev. Lett. 117, 151803 (2016)

[12] M. G. Aartsen et al, Phys. Rev. Lett. 117, (2016) 071801

[13] S. Gariazzo et al, arXiv:1703.00860 (2016)

[14] M. Harada, *et al*, arXiv:1310.1437 [physics.ins-det]

[15] R/ Acciarri et al, arXiv:1503.01520 (2015)

[16] S. Woosley and H.-T. Janka, Nat. Phys. 1, 147 (2005), and references therein.

[17] K. Otsuki, H. Tagoshi, T. Kajino and S.Wanajo, Astrophys. J. 533, 424 (2000).

[18] S. Wanajo, T. Kajino, G.J. Mathews and K. Otsuki, Astrophys. J. 554, 578 (2001).

[19] T. Kajino, S. Wanajo and G.J. Mathews, Nucl. Phys. A704, 165c (2002).

[20] T. Yoshida et al., Phys. Rev. Lett. 96, 091101 (2006).

[21] S.X. Nakamura, K. Sumiyoshi and T. Sato, Phys. Rev. C80, 035802 (2009).

[22] R. Maschuw (KARMEN Collab.), Prog. Part. Nucl. Phys. 40, 183 (1998).

[23] L.B. Auerbach et al. (LSND Collab.), Phys. Rev. C64, 065501 (2001).

[24] J.N. Abdurashitov et al. (SAGE Collab.), Phys. Rev. C59, 2246 (1999).

[25] W. Hampel et al. (GALLEX Collab.), Phys. Lett. B420, 114 (1998); F. Kaether et al. (GALLEX Collab.), Phys. Lett. B685, 47 (2010).

[26] J.R. Distel et al., Phys. Rev. C68, 054613 (2003).

[27] M. Harada, *et al*, arXiv:1601.01046 [physics.ins-det]

[28] J. Beringer *et al.* [Particle Data Group], Phys. Rev. D **86**, 010001 (2012).

[29] J. Spitz, Phys. Rev. D **85**, 093020 (2012).

[30] J. Spitz, Phys. Rev. D **89**, 073007 (2014).

[31] S. Axani, G. Collin, J.M. Conrad, M.H. Shaevitz, J. Spitz, and T. Wongjirad, Phys. Rev. D **92**, 092010 (2015).

[32] C. Rott, S. In, J. Kumar, and D. Yaylali, Journal of Cosmology and Astroparticle Physics **11**, 039 (2015).

[33] J-PARC Project Newsletter special issue, May 2015.

[34] S. Agostinelli *et al.*, Nucl. Instr. Meth. A **506**, 250 (2003).

[35] N.V. Mokhov, FERMILAB-FN-628 (1995); O.E. Krivosheev and N.V. Mokhov, "MARS Code Status", Fermilab-Conf-00/181 (2000); O.E. Krivosheev and N.V. Mokhov, "Status of MARS Code", Fermilab-Conf-03/053 (2003); N.V. Mokhov, K.K. Gudima, C.C. James *et al.*, "Recent Enhancements to the MARS15 Code", Fermilab-Conf-04/053 (2004).

[36] T. Katori, Neutrino Cross Section Newsletter (12/23/2014); https://pprc.qmul.ac.uk/ katori/nu-xsec.html.

[37] D. G. Michael *et al.* [MINOS Collaboration], Nucl. Instrum. Meth. A **596**, 190 (2008).

[38] D.S. Ayres *et al.* [NOvA Collaboration], FERMILAB-PROPOSAL-0929 (2004).

[39] R. Acciarri *et al.*, [DUNE Collaboration] (2015), Long Baseline Neutrino Facility (LBNF) and Deep Underground Neutrino Experiment (DUNE) Conceptual Design Report, available in 4 volumes at http://www.dunescience.org/.

[40] K. Abe *et al.* [T2K Collaboration], Nucl. Instr. Meth. A **659**, 106 (2011).

[41] J. Cao *et al.*, Phys. Rev. ST Accel. Beams **17**, 090101 (2014).

[42] E. Baussan *et al.*, arXiv:1309.7022 [hep-ex] (2013).

[43] J.E. Campagne, M. Maltoni, M. Mezzetto, and T. Schwetz, J. High Energy Phys. **0704**, 003 (2007).

[44] Private communication with N. Jachowicz.

[45] V. Pandey, N. Jachowicz, T. Van Cuyck, J. Ryckebusch, and M. Martini, Phys. Rev. C **92**, 024606 (2015).

[46] G. Battistoni, S. Muraro, P.R. Sala, F. Cerutti, A. Ferrari, S. Roesler, A. Fasso', J. Ranft, Proceedings of the Hadronic Shower Simulation Workshop 2006, Fermilab 6–8 September 2006, M. Albrow, R. Raja eds., AIP Conference Proceeding 896, 31-49, (2007); A. Ferrari, P.R. Sala, A. Fasso', and J. Ranft, CERN-2005-10 (2005), INFN/TC_05/11, SLAC-R-773.

[47] T.Suzuki et.al., Phys. Rev. C 35 (1986) 2212.

[48] M. Harada, et al., Settlement of Materials and Life Science Experimental Facility at J-PARC, Nucl. Inst. Meth, A600 (2009) 8790.

[49] X. Zhou *et al.*, arXiv:1408.0877v2 [physics.ins-det], (2015)

[50] private communication

[51] Hamamatsu Photonics, Catalog "Large Photocathode area Photomultiplier tubes"

[52] T. Matsubara et al., Nucl.Instrum.Meth. A661 (2012) 16-25

[53] `http://www.hilltech.com/pdf/hl-fm10-cFinemetIntro.pdf`

[54] `https://www.researchgate.net/publication/256925904_Light-weight_Flexible_Magnetic_Shields_For_Large-Aperture_Photomultiplier_Tubes`

[55] `http://www.reiko.co.jp/eng/product_film.html`

[56] UMD2792 - V1730/VX1730 & V1725/VX1725 User Manual rev. 2 - 10 June 2016, CAEN.

[57] J. S. Park *et al.* [RENO Collaboration], Nucl. Instrum. Meth. A **707**, 45 (2013).

[58] J. K. Ahn et al., arXiv:1003.1391 (2010)

[59] R. Alves et al., JINST 10 (2015) P03002.

[60] P. Wahnon, Final year undergraduate project report (2010), University of Sussex.

[61] T. Matsubara, Ph.D thesis (2011), Tokyo Institute of Technology.

[62] Double Chooz Collaboration, JHEP 1410 (2014) 086,
Daya Bay Collaboration, Chin.Phys. C41 (2017) no.1, 013002.

[63] Y. Sakemi *et al*, IAEA-TECDOC-1743, 229 (2014).

[64] M. Harada, *et al*, arXiv:1502.02255 [physics.ins-det]

[65] S. Ajimura, *et al*, PTEP 2015 6, 063C01 (2015)

[66] N. Mauri et al, EPJ Web Conf. 126 (2016) 04031